Advanced methods in Glancing Angle Deposition to control thin film morphology, microstructure and texture

by

Joshua Michael LaForge

A thesis submitted to the Faculty of Graduate Studies and Research
in partial fulfillment of the requirements for the degree of

Doctor of Philosophy

in

Micro-Electro-Mechanical Systems and Nanosystems

Department of Electrical and Computer Engineering

Spring 2014
Edmonton, Alberta

Ashley, whose idea was it anyway?

Abstract

Structuring of material on the nanoscale is enabling new functional materials and improving existing technologies. Glancing angle deposition (GLAD) is a physical vapor deposition technique that enables thin film fabrication with engineered columnar structures on the (10 to 100) nm scales. In this thesis, we have developed new methods for controlling the morphology, microstructure, and texture of as-deposited GLAD films and composite films formed by phase transformation of GLAD nanocolumn arrays during post-deposition annealing. These techniques are demonstrated by engineering the vapour flux motion in both Fe and ZnO nanorod deposition and FeS_2 sulfur-annealing.

Crystalline Fe nanorods with a tetrahedral apex can be grown under rapid continuous azimuthal rotation of the substrate during growth. Discontinuous azimuthal rotation with 3-fold symmetry that matches the nanocolumn's tetrahedral apex symmetry produces nanocolumns with in-plane morphological and crystal orientation. This method, called flux engineering, provides a general approach to induce biaxial crystal texture in faceted GLAD films. Similar effects were found for ZnO nanocolumns.

Reliable production of photovoltaic-grade iron pyrite thin films has been challenging. Sulfur-annealing of bulk films often produces cracking or buckling. We used the flux-engineering processes developed for Fe to control the inter-column spacing of the precursor film. By precisely tuning the inter-

column spacing of the precursor film we can produce iron pyrite films with increased crystallite sizes >100 nm with a uniform, crack-free, and facetted granular microstructure. Large crystallites may reduce carrier recombination at grain boundaries, which is attractive for photovoltaic cells. We assessed the viability of these films for photovoltaic applications with composition, electrical, and optical characterization. Notably, we found a 27 ps lifetime of photocarriers measured with ultrafast optical-pump/THz-probe and tested charge-separation characterization between the pyrite films and a conjugated polymer with absolute photoluminescence quenching measurements. These results provide the foundation for future improvements in pyrite processing for photovoltaic cells.

Acknowledgments

Study at the PhD level is rarely (if ever) performed in complete isolation. There are many individuals and groups that have contributed to the work within this thesis and my scientific, professional and personal development. To all of them I am thankful for that which they have invested in me.

I would like to thank my supervisor Michael Brett for encouraging me to pursue PhD studies and then facilitating that work by continuously investing in our group and the scientific infrastructure at the University of Alberta and the NRC National Institute of Nanotechnology. Michael Taschuk has contributed significantly to my development as a scientist, thinker, and professional through hours of mentorship and multi-year discussions. Similarly, Michael Fleischauer has engaged in many conversations about the scientific process over the years. Jillian Buriak provided wisdom about effective scientific communication and the peer-review process from her years of experience in academic publishing. In addition I would like to thank Frank Hegmann, Jeremy Sit, Jie Chen and Al Meldrum for their support.

For several years I have worked closely with a small team within our group. This team consisted of two other graduate students, Ryan Tucker and Allan Beaudry, and Michael Taschuk. Working with this team has been profoundly rewarding. The experience has shaped my expectations for excellence in team-based scientific projects.

Throughout the years I have had many meaningful conversions with fellow graduate students and post-docs within our lab and elsewhere on campus. These conversions have influenced my development as a young professional. Specifically I would like to thank Ryan Tucker, Abeed Lalany, Jaron van Dijken, Brian Worfolk, Matthew Hawkeye, Tyler Cocker, Joshua Krabbe, Nick Wakefield, Louis Bezuidenhout, Zhifeng Huang, Katie Krause, Andy van Popta, Ken Harris, Joshua Siewert, Michael Thomas, and Jason Sorge.

I have been fortunate to mentor and work with two excellent undergraduate students, Grayson Ingram and Balazs Gyenes. Both of whom have contributed experimental work to this thesis.

Numerous support staff, technical and administrative, contribute on a daily basis to the smooth operation of the University of Alberta's scientific infrastructure. Thank you for your often unsung contributions. In partic-

ular though I would like to thank Shiraz Merali, Kai Cui, Peng Li, Steven Launspach, George Braybrook, De-Ann Rollings, Paul Conception, Jason Dibbs, Martin Kupsta, Dimitre Karpuzov, Anquang He, Shihong Xu and Ben Bathgate for their technical support of my work.

I would like to thank generous funding from both public and private sources. In particular, I have attempted to respect the honor and privilege that accompanies public funding by applying myself dutifully. Public sources include the Natural Sciences and Engineering Research Council of Canada (NSERC), Alberta Innovates Technology Futures (AITF, formerly Alberta Ingenuity and iCORE), the National Research Council (NRC), and the University of Alberta. Micralyne, an Edmonton-based MEMS manufacturer has long sponsored an Industrial Research Chair for Michael Brett that has contributed to the development of the facilities I used throughout my tenure as a PhD student.

Lastly, thank you to all the friends and family that have supported and encouraged me through all these years of study.

Table of Contents

List of Tables

List of Figures

List of Symbols & Abbreviations

α	Deposition angle, angle of flux relative to the substrate normal.
α_o	Optical absorption coefficient.
χ	Spread of XRD peak in azimuthal direction.
$\Delta\Theta$	Angular distribution of vapor flux.
Γ	Deposition flux rate.
Λ	Surface diffusion.
μ	Carrier mobility
$\mu_{\chi m}$	X-ray linear mass attenuation coeffiicient
μ_{PV}	Efficiency of photovoltaic conversion.
ν	Optical frequency.
ω	Incoming x-ray scattering angle
ϕ	Azimuthal angle of the substrate chuck during deposition.
ρ	Electrical resistivity.
ρ_m	Bulk mass density of a material.
ρ_N	Number density of objects in an image. Reported in object number per unit area.
ρ_A	Areal density of objects in an image. This represents the ratio of the total spatial area taken up objects and total image area, after correction with the adjusted counts.

τ_h Average time between adatom hops

τ_m Monology growth time

θ Bragg angle

Θ_T Homologous temperature T_S/T_M

$\vec{Q}$ X-ray scattering vector

A_{image} Image area. The field of view in an SEM for instance.

$A_{objects}$ Object area. A single GLAD post for instance.

D Scherrer crystallite size from XRD data.

d Inter-column spacing.

d_{hkl} Crystal lattice spacing.

E Kinetic energy of a particle in the vapor flux.

E_g Energy of the electrical band-gap.

$F_{x,y}$ Object widht/height.

h Planck's constant. $h = 6.62606957(29) \times 10^{-34}$ J s

K_θ, K Incoming/outgoing x-ray wave-vectors

L_o Optical absorption length.

N Raw object count.

$N_{adjusted}$ Adjusted object count.

n_{maj} Majority carrier density

n_{ref} Mobility parameter for the reference carrier density

p Pearson significance

r Correlation (statiscal)

R_o Optical reflection coefficient.

t Film thickness

T_M Melting temperature

T_o Optical transmission coefficient.

T_S Film growth surface temperature

V_{OC} Open-circuit photovoltage.

w GLAD post diameter.

$W_{x,y}$ Image, typically SEM, width/height dimensions.

AES Auger electron spectroscopy

AFM Atomic Force Microscopy

AFM Atomic force microscopy

EDX Energy Dispersive X-ray Spectroscopy

FIB Focused Ion Beam

FTO Flourine-doped tin oxide

GLAD Glancing angle deposition

ISB Inclined substrate deposition. See OAD.

ITO Indium tin oxide

OAD Oblique angle deposition. Typically used in cases were the deposition angle $\alpha < 70°$.

PL Photoluminescence

PVD Physical vapour deposition

SAED Selected-area electron diffraction

sccm Standard cubic centimeters per minute. Used to measure gas flow rate.

STEM-HAADF Scanning Transmission Electron Microscopy - High Angle Annular Dark Field

TEM Transmission electron microscopy

ToF-SIMS Time-of-Flight Secondary Ion Mass Spectroscopy

XRD X-ray diffraction

Chapter 1

Introduction

The histories of materials science and technological development are intimately linked. Materials development enables technology development, which in turn enables new materials development, setting up a virtuous cycle of scientific and technological progress. Presently, efforts are focused on pushing our understanding and control of materials into the nanoscale. This is the essence of the set of fields broadly characterized as nanotechnology.

There are several modern technological examples that illustrate the success of materials science and materials structuring at the nanometer scale. Perhaps the most common, sophisticated example is the modern integrated circuit. In 2012, Intel® started shipping processors based on the 22 nm Tri-gate technology, otherwise known as FinFETs. An example of a FinFET transistor is shown in Figure 1.1. The three-dimensional structure of this device is due to the novel raised transistor channel architecture which allows the gate to surround the channel and control current flow more effectively than in a traditional planar transistor. This innovation reduces power usage of the transister by limiting leakage current[15]. Fabricating these devices at scale required a decade-long effort in materials processing research, which provides a clue as to the amount of effort such achievements require. The result is that transistor density in integrated circuits continues to scale exponentially, according to Moore's Law, with Intel demonstrating processors with 5 billion transistors.[i].

[i]Intel's ® 62-core Xeon Phi has 5 billion transistors.

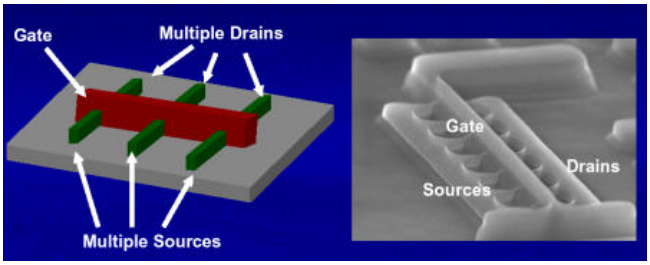

Figure 1.1: Schematic and electron micrograph of a FinFET. Zathlon, "Trigate" June 24, 2006 via Wikipedia, Creative Commons Attribution.

Outside of the microelectronics industry, nanoscale materials are finding applications in virtually every technological application from energy to medicine. Notable examples include, photovoltaic technologies for solar power generation that have developed from wafer-based technologies to conventional thin-films and onto more sophisticated quantum dot or organic architectures in the pursuit of lower-cost and greater conversion efficiencies. Mechanical energy-scavenging technologies that depend on nanowires made of piezoelectric materials have been developed. Graphene, a 2D layer of carbon, is being rapidly developed for electronics. Biosensing, such as bio-tagging with quantum dot fluorescence or nanoplasmonics, is poised to rapidly improve quantification of medicine for individualized treatments.

All of these developments require a robust method for controlling material properties on the nanoscale. Consequently, groups are continuously investigating new methods for nanoscale fabrication and improving existing methods. This thesis has focused on improving one particular fabrication and structuring technique called Glancing Angle Deposition (GLAD) that can be used to create columnar thin film structures. The overall goal of this thesis is to develop advanced methods in GLAD to further develop functional materials for energy applications, such as photovoltaic cells.

1.1 Materials synthesis and processing

Materials science is a strongly interdisciplinary field with contributions and collaborations from biology, chemistry and physics. As such, the methods for

controlling material synthesis, and thereby material properties, are diverse and varied. Materials of interest include organic materials (e.g., plastics, semiconductor polymers, and photoactive small molecules), inorganic material (e.g., semiconductors, ceramics, metals) and composites. In application these materials are assembled on spatial scales that range from $\approx 10^{-}9$ m in the case of quantum dots to $\approx 10^2$ m in the case of buildings and bridges and $\approx 10^4$ m in the case of the interstate highway system. This represents spatial control over the arrangement of materials spanning 13-orders of magnitude! An incredible achievement of technological progress that cannot be over-emphasized.

In this thesis, we are primarily interested in thin films. Such films typically range from ≈ 1 nm to $\approx 1\,\mu$m in thickness, and can be composed of bulk/continuous or porous material. The structure, grains, and material arrangement play a critical role in the material properties. These effects can manifest as changes in the effective medium. For example, periodically altering the film porosity modulates the effective index of refraction to form a photonic crystal[16]. In other cases, fundamental material parameters can be altered from their bulk values. The shift in electronic energy levels due to quantum confinement in quantum dots or quantum wells are a well-cited example of the substantial effect that structure can have on a material's properties[17, 18].

1.1.1 Bulk thin films

Thin films are primarily produced by vacuum deposition techniques, such as physical vapour deposition, chemical vapour deposition[19], atomic layer deposition[20], and pulsed laser deposition [21] due to the highly controlled environment of a vacuum that in turn enables precise composition control [19]. However, chemical synthesis techniques performed in less controlled environments are possible in some applications. These techniques include, but are not limited to, spray-coating[22], spin-casting, sol-gel[23], and electroplating [24]. Post deposition processing may include a sintering step, for example, to recrystallize an inorganic colloidal ink into a thin film[25], or annealing (thermal processing) to affect composition or microstructure.

Each technique has its own advantages that include the control over the material synthesis, fabrication speed, and costs (infrastructure and operation). Selection is made based on the application requirements and costs. Due to the high degree of environmental control available in vacuum deposition, these methods tend to find applications in the microelectronics industry where strict control over composition (i.e., doping, defects, contaminants) is required to ensure proper device performance.

Physical vapour deposition such as evaporation or sputtering affords control over the thin film properties by tuning the deposition conditions during growth. These include temperature, pressure (residual or added gas composition), deposition rate, and shadowing effects. Structure zone diagrams, such as those developed by Thornton [2] are assembled to describe the effect of the deposition conditions on the structure of the film. For example, the structure zone diagram for high-rate sputtering shown in Figure 1.2 describes the effects of several processes on the final film morphology.

Additional processes can be used to further modify the structure of the films during growth. Particle bombardment, from substrate-biased sputtering or ion milling, can have significant effects on the structure and crystallinity of the resulting film[19]. Film texture can also be modified by depositing at modest oblique angles ($\alpha \ll 70°$) and at deposition angles relevant to GLAD ($\alpha \geq 70°$)[26]. These points will be discussed later.

A survey of the energy sources available to modify the film structure during growth was compiled by Harper[3] and reproduced in Figure 1.3. Many secondary effects, such as phase transformation, grain growth, interface energy minimization, and strain energy minimization can have important and dramatic effects on structure[19, 27, 28]. Post-deposition thermal processing can assist in modification of the film structure directly through diffusion and by activating other processes such as grain growth or compound formation. Several of these effects will play an important role in determining the structure of the films discussed in this thesis.

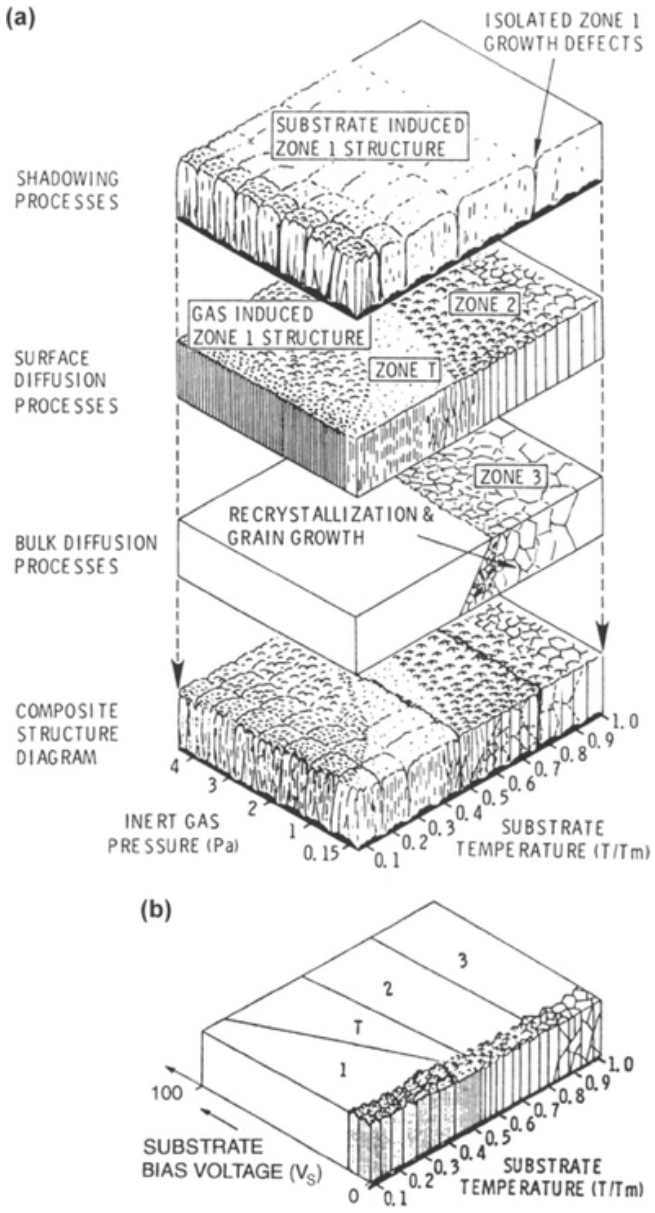

Figure 1.2: (a) Structure zone diagram that demonstrates the superposition of deposition processes that control the structure in high-rate sputtering growth. In (b) the effects of substrate bias voltage during sputtering are shown. Reproduced with permission from [2].

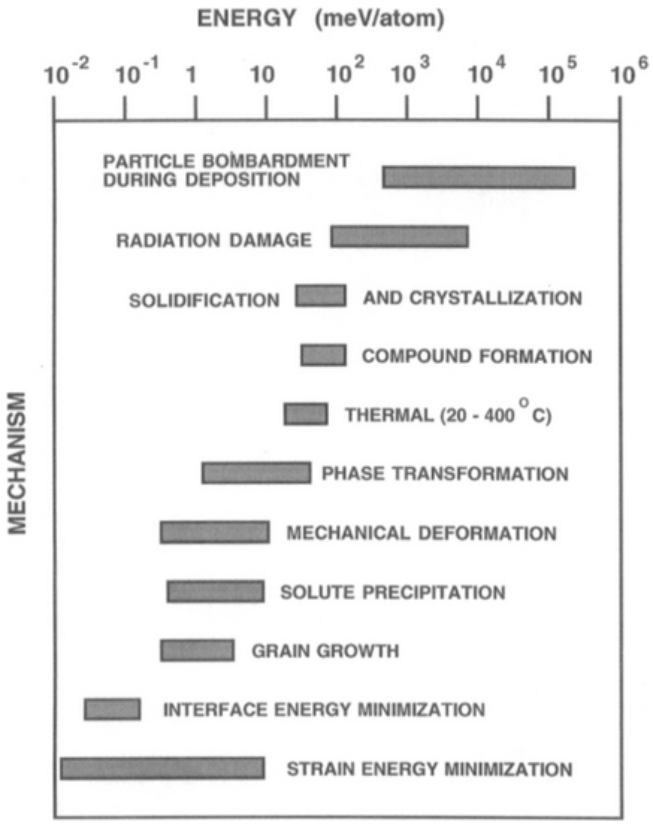

Figure 1.3: Survey of energy sources available for structural modification of the thin films. Reprinted with permission from [3]. Copyright 1997, American Vacuum Society.

1.1.2 Nanostructured thin films

Engineering 3-dimensional columnar, porous, thin films has garnered significant interest in a variety of application areas due to the potential for performance improvements. These applications include optical devices[16, 29, 30], structured electrodes[31], high-interface area sensors[32, 33, 34, 35], magnetic recording media[36], and nanoelectronics[37, 38, 39, 40].

While this thesis focuses on GLAD, a physical vapour deposition method that can precisely engineer thin film material into columnar structures on the (10 to 100) nm scale[41, 4, 42, 43], there are several competing techniques. These include both bottom-up[44] and top-down nanostructuring techniques[45]. Top-down processing includes templating, such as with anodized aluminum oxide[46], and deep reactive ion etching[19], which are often used to produce arrays of one-dimensional nanowires[47, 48]. The smallest of these structures tend to have diameters in the range of (10 to 100) nm because controlling infilling or etching processes on the $\approx$ 10 nm scale is challenging.

Bottom-up processes are dominated by seeded forms of nanowire growth, such as vapour-liquid-solid growth of nanowires[45, 49, 50, 51], carbon nanotube growth[52], or dislocation-driven nanowire growth[53]. These techniques can produce nanowires with diameters $\approx$10 nm wide with high-aspect ratios ($t/w > 100:1$) of highly crystalline materials. Nanowire growth is controlled by many of the same parameters that affect bulk film growth in physical vapour deposition, such as availability of reactants (chemical potential or deposition rate), pressure, residual gas composition, and temperature. The seed material can be used to dope semiconductor nanowires during growth, but in other cases can induce unwanted contaminants into the nanowire[54]. Preventing contamination from the seed material can be difficult and is an active research problem[55]. Due to the high-level of interest in nanowires and their applications, growth capabilities have developed quickly. Recent advances have demonstrated kinking to change the growth direction[56], radial and linear pn junctions[57], and diameter modulation[8].

1.2 Glancing Angle Deposition

Glancing Angle Deposition[58, 59, 60, 4] is a physical vapour deposition technique developed by the Brett group at the University of Alberta. The key innovations of GLAD are: 1) use of dynamic substrate rotation to orient the substrate freely into any orientation during growth and 2) a highly oblique, collimated vapour flux such that the deposition angle is $\alpha > 70°$. Combined, these two enhancements allow for the column morphology to be precisely controlled during film growth by a process of geometric self-shadowing. These features will now be explained in more detail.

Substrate rotation allows for precise positioning of the collimated vapour flux relative to the substrate plane (Figure 1.4). Two stepper motors actuate the rotations around two axes; one around the substrate normal changes the azimuthal position of the flux, ϕ, and another axis in the substrate plane changes the angle of inclination, known as the deposition angle, α. Together these two rotations control the flux direction and change the column growth direction. This capability allows a variety of structures to be produced including vertical posts, helices and square spirals by changing the flux motion algorithms during growth, as seen in Figure 1.5. The structures have allowed GLAD films to be constructed for a variety of device applications such as birefringent optical filters[61, 62], photonic crystals [63], chemical and biological sensors[64, 65, 66, 30, 16] and mechanical pressure sensors[67].

GLAD growth is often viewed as a ballistic growth process, where the column shaping process relies on geometric shadowing to limit the location of material deposition to the column tips. Migration of material from the deposition location to the shadowed surface is therefore undesirable. To limit surface diffusion, and thus migration of material to the shadowed portion of the growth surface, a low homologous temperature is used; the film growth surface temperature (T_S) is a small fraction of the material's melting point (T_M) so that $\Theta_T = T_S/T_M < 0.3$. This allows for shadowing processes in the film to have a greater influence in shaping the morphology of the film, as seen in Figure 1.2. When $\Theta_T \to 1$ GLAD can become ineffective at controlling the surface evolution of the material[4, 68].

A conceptual illustration of the GLAD growth process is shown in Fig-

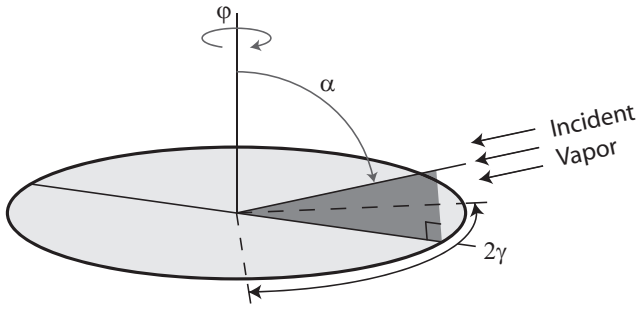

Figure 1.4: Schematic representation of the collimated vapour flux position relative to the substrate plane. Flux position is controlled by the azimuthal angle ϕ and deposition angle (inclination angle α). A modulation angle γ is sometimes used to denote oscillation in the flux azimuthally, relative to the vapour incidence plane defined by the substrate normal and flux vector. Reproduced with permission from [4].

ure 1.6. Growth proceeds from initial nucleation, through roughening where surface topology initiates geometric shadowing, and then onto deposition of columnar structures once shadowing is initiated. Materials that nucleate by a Volmer-Weber growth process[19] will tend to produce well-formed structures, as geometric shadowing can be initiated soon after the nucleation process. However, the Volmer-Weber nucleation model does not apply to all materials and may not be justified at the low homologous temperatures in which GLAD usually operates. Instead, at low homologous temperatures, kinetic roughening can produce sufficient surface topology to initiate geometric shadowing[69]. The study of kinetic roughening is deep and connected to the theory of fractal surface evolution. These concepts are beyond the scope of this thesis, but the interested reader can find several texts on the subject [69, 70].

There are characteristic limitations to traditional columnar GLAD films grown by ballistic deposition and geometric self-shadowing. The stochastic development of nanoscale structure with GLAD has been described as physical self-assembly[71]. However, it is more apt to call GLAD growth a physical self-organization process as it occurs under non-equilibrium conditions[72]. The organization of material is not perfect. For instance, oxide materials often contain fibrous intracolumn structures[4]. These features are a direct

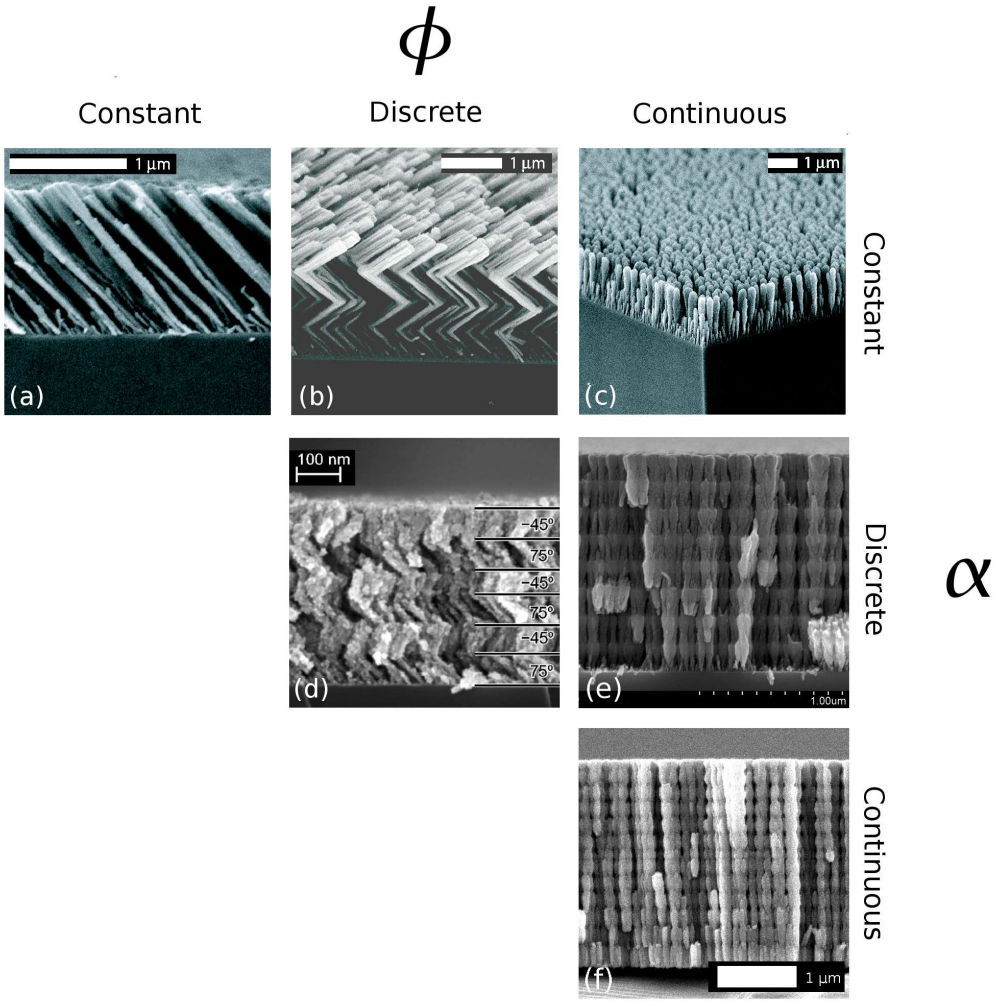

Figure 1.5: The basic GLAD structures: (a) slanted post, (b) chevron, (c) vertical post, (d) slanted post stack, (e) high-low stack and (f) Rugate. These structures are fabricated using constant, discrete and continuous motion in α and ϕ. Reproduced with permission from [4]. (a-c) Reproduced with permission from [5] and (d) Reprinted with permission from [6]. Copyright 2007, American Institute of Physics.

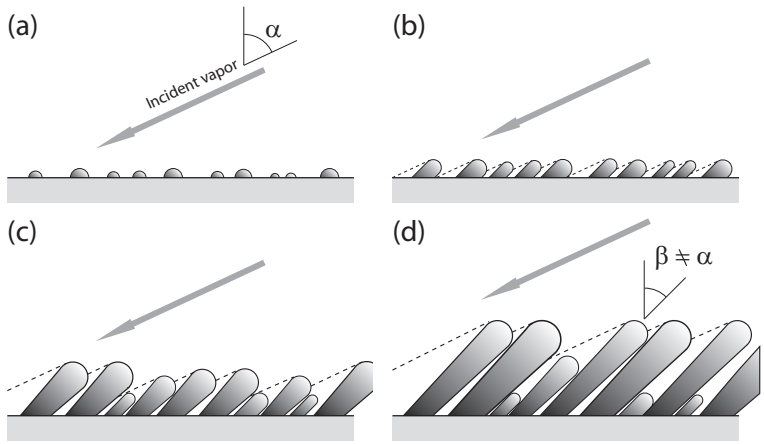

Figure 1.6: Conceptual illustration of the GLAD growth process from a) nucleation, b) onset of geometric shadowing, c-d) development of columns and column extinction. In slanted posts the column tilt angle ϕ is often smaller than α. Reproduced with permission from [4].

result of the stochastic nature of the GLAD growth process. In general, small scale structure (<10 nm) within an individual column cannot be reliably controlled with GLAD. At larger-scales, $\approx$ 100 nm, the inter-column structure can be controlled through defining a seed pattern that initiates geometric shadowing and defines the spatial arrangement of the columns. Shadow instability and column width broadening during growth place limits on the fidelity of this initial pattern as the film grows[73, 74, 75]. In other words, the correlation length of the growth surface in a typical GLAD film is finite and on the order of 100 nm [69, 70, 73, 76]. Considerable effort has been made to increase the correlation length for optical applications of GLAD films, such as in photonic crystals [74, 75]. These requirements motivated the development of the phi-sweep method that modulates the azimuthal position (modulation angle γ in Figure 1.4) of the substrate to suppress shadow instability and maintain good adherence to an initial seed pattern after $t \approx 1000$ nm of growth [77, 74, 75]. A combination of patterned seeds to initiate geometric shadowing and a tuned phi-sweep modulation angle γ that limits deposition between the columns represents the state-of-the-art in column engineering with GLAD. Presently, it is not clear if additional improvements can be made with more complex motion algorithms that further mitigate shadow insta-

bility. Other solutions will have to be explored, such as crystalline growth modes that provide additional constraints on column broadening, improve intracolumn structure, and enable control over other microstructural features. Enabling or enhancing crystalline growth modes in GLAD is a general theme of this thesis.

1.2.1 Crystallinity in GLAD films

Crystalline growth processes can occur in GLAD films. These effects can be used to control morphology, microstructure and texture [26] of the films by designing the process parameters accordingly (e.g., flux configuration, temperature, deposition rate). Early reports on the influence of deposition flux rate and rotation rate on the development of crystalline columns were made about a decade ago [43, 78, 79]. Since that time, specific materials studies have been made on elemental and composite materials as listed in Table 1.1. These additional studies have also reported on the influence of pitch, the amount of the film growth along the substrate normal per substrate rotation, and on the morphology and crystallinity of GLAD films [4, 80, 81, 82, 83, 84]. In this thesis, we will primarily use the deposition rate and the flux motion (in α and ϕ) to control the film's properties.

Table 1.1: List of crystalline materials deposited with GLAD.

Elemental materials		
Cu [85, 67, 82, 86, 87]	Ge [88]	Mg [89]
Ru [90, 83]	Sn [91]	W [92, 93, 94]
Composite materials		
CaF_2 [95]	CrN [96]	MgF_2 [97]
MgO [98, 99]	YSZ [80, 100]	ZnO [101, 81]

More recently, vapour-liquid-solid (VLS) crystalline nanowire growth of indium tin oxide (ITO) and Ge has been adapted to GLAD in a process named VLS-GLAD [102, 103, 104]. In VLS growth a eutectic droplet concentrates vapour and precipitates the vapour as a crystalline material at the droplet/solid interface. In effect, the droplet constrains the shape and broadening of the column/nanowire as it grows. This process was first developed

by Wagner in 1964 for Si and has been applied to many semiconductors and oxides since that time [105, 45, 49, 50, 51].

As mentioned above, large values of Θ_T can often be deleterious to GLAD films due to the larger surface diffusion smoothing out the structure. However, in some materials evaluated temperatures can enable alternative and useful growth modes. Indium tin oxide (ITO) provides a striking example of this case. For $\Theta_T < 0.2$ ITO grows as a typical columnar GLAD film. As temperature is increased to $\Theta_T > 0.3$ In/Sn droplets form and the growth mode changes from ballistic self-shadowing to VLS crystalline nanowire growth. This results in branched nanowire structures called 'nanotrees'[102]. The VLS growth process can be enhanced with the geometric shadowing provided with GLAD. Effects such as shadow-mediated diameter modulation, and biaxial texture through evolutionary selection have already been demonstrated in VLS-GLAD systems[8, 106]. Access to the growth of a wide range of materials compatible with VLS and provides new opportunities to extend the GLAD toolkit.

Controlling crystal texture with evolutionary selection

Crystal growth in GLAD films appears to be connected to texture evolution. Shadow-mediated competition exists between the columns in a GLAD film, and the deposition conditions should ensure that crystalline columns are able to avoid extinction during growth. Abelmann and Lodder [26] note that texture development requires that crystals can grow in a manner that minimizes their surface energy. This is only possible in cases of high surface diffusion, or with vapour incident from all directions. This observation provides a clue as to the role of deposition pitch in encouraging crystal growth in GLAD films.

Although a complete picture of texture evolution [26, 107, 108] has yet to be developed, contributing effects include the crystal geometry [90, 109], flux capture cross-section[100, 110], asymmetric surface diffusion [111], surface energy[100, 112, 92, 109, 113], and shadowing[90]. Development of the in-plane and out-of-plane texture can be controlled by shadow-mediated competition between the nanocolumns, whereby columns with a faster vertical

growth rate are able to out-compete columns that grow more slowly. This process is known as evolutionary selection. In cases where the azimuthal flux symmetry is broken, biaxial texture can be developed, due to a competitive advantage afforded to nuclei oriented for rapid growth. Out-of-plane texture is often defined by the surfaces with low-adatom mobility (interface minimization effect) due to enhanced adatom capture and therefore faster vertical growth[100, 95, 92].

Control of crystal texture by engineering the flux motion is a major theme in Chapter 3. More discussions of crystal texture effects in GLAD films will be provided there.

Thermal processing

Post-deposition annealing steps can often have beneficial effects for enhancing the composition or crystallinity of GLAD films[31, 4]. For example, a two-step annealing process is used in both regular GLAD ITO and VLS-GLAD ITO to increase transmissivity and conductivity of the material[31, 102].

High-temperature annealing can modify the film morphology through many of the same processes identified during growth at high-temperature (Figure 1.3) such as grain growth, recrystallization, diffusion and compound formation[28, 114, 115, 116, 117]. Therefore, care must to taken when developing an annealing process to select temperatures, heating rates, and exposure times that will improve the desired material properties without negatively affecting others. In the case of GLAD films, additional concern must be given to maintaining structural fidelity during the annealing process. As a rule of thumb to prevent significant loss of structural definition annealing should be limited to $\Theta_T \lesssim 0.5$.

Post-deposition sulfur-annealing of Fe GLAD films is discussed further in Chapters 4 and 5. This process was used to develop iron pyrite (FeS_2) thin films where microstructural control is imposed through design of the Fe precursor morphology.

1.3 Motivation and materials selection

As GLAD has matured, an increased focus on device applications has emerged. Several potential areas of technological significance have been explored[4], including optics [61, 62, 63], sensors [64, 65, 66, 30, 16], mechanical devices [67], catalysis [118, 119], microfluidics [120, 121], chemical analysis [122], and energy [31, 4]. Advanced energy materials are of particular interest to our group. These applications require materials structuring techniques that also maintain other characteristics important for device operation, such as semiconductor behavior, chemical activity, and optical transparency. Simultaneous optimization of both morphology and other functional properties presents new challenges for GLAD. Specifically, achieving semiconductor behavior requires crystalline material. This requirement may be achieved through either a crystalline growth mode or by thermal processing post-deposition.

In this thesis, we worked towards meeting these challenges for two materials of significance for energy generation; FeS_2 and ZnO. Iron pyrite, FeS_2, is an earth-abundant semiconductor with widely recognized potential for photovoltaics (Chapter 4 and 5). ZnO nanocolumns can be used as a transparent conductive oxide for photovoltaics and as a piezoelectric mechanical energy scavenger (Chapter 6). Further introduction to these materials will be provided in their respective chapters.

Two major thrusts were undertaken in this thesis. The first thrust involves development of flux engineering techniques for enhanced morphological, microstructural and crystal texture control over as-deposited GLAD materials. These methods were demonstrated with Fe (Chapter 3) and ZnO (Chapter 6). The second thrust centers on development of a fabrication process for FeS_2 with intent towards photovoltaic applications. The Fe films developed in Chapter 3 were used as precursors for the production of FeS_2 films via sulfur-annealing (sulfurization). Control over the Fe inter-column spacing was used to influence the recrystallization process that occurs during sulfurization, and allows us to tune the iron pyrite film microstructure (Chapter 4 and 5).

Others groups have previously explored crystalline GLAD growth in both Fe [123, 124, 125, 126, 127, 128, 129, 130] and ZnO [101]. Previous work

on oblique deposition of Fe has used stationary substrates or continuous azimuthal flux motions to characterize the role of deposition angle, deposition rate, pressure, and temperature in determining the magnetic anisotropies, column tilt angle and crystal texture of Fe nanocolumns. We have extended those studies by providing a wide survey in pitch of Fe nanocolumn growth at highly oblique deposition angles. Additionally, we have shown that discrete flux motions can be used to develop biaxial texture in these Fe nanocolumns. This technique complements other flux motion algorithms used to control crystal texture, which have been previously demonstrated in GLAD materials including:CaF_2 [95], Cu [85, 67, 82, 86, 87], MgO [98, 99], Ru [90, 83], W [92, 93, 94].

The previous work on ZnO [101] provided a proof-of-concept of low-temperature crystalline ZnO growth. We have complemented this work by systematically exploring the effects of flux engineering (i.e., substrate rotation rate and deposition rate) on the morphology and crystallinity of ZnO nanocolumns to test the feasibility of using GLAD to create high-aspect ratio columnar structures or nanowires.

Thus far, reliable production of phase-pure iron pyrite thin films with controlled material properties remains difficult, limiting photovoltaic device development [10, 131]. Recent work has focused on fabrication of iron pyrite thin films using techniques including solvothermal synthesis [132], metal-organic chemical vapor deposition [133, 134], chemical vapor deposition [135, 136], spray pyrolysis [137, 138, 139, 140], nanoparticle synthesis [141, 25], sputtering [142, 143], sol-gel [144], chemical vapor transport [145, 146, 147], and sulfurization of iron and iron oxide precursors films [148, 149, 150, 151, 152, 142, 153, 154, 155, 156].

Sulfurization is attractive for its simplicity and therefore potentially low processing costs. Sulfurization of bulk thin films suffer from potential stress failure of the iron pyrite film, such as buckling or cracking [157, 158, 159, 150]. During phase transformation unconstrained material will expand due to the density difference between iron ($\rho_m = 7.87\ \mathrm{g \cdot cm^{-3}}$) and iron pyrite ($\rho_m = 4.89\ \mathrm{g \cdot cm^{-3}}$). Attempts to alleviate stress failures include the addition of adhesion layers [142] and limited attempts to introduce porosity into Fe precursor by depositing onto heated substrates [150]. By using columnar

Fe-precursors deposited with GLAD, and developed in Chapter 3, we can accommodate the material expansion during sulfurization. We show that stress failure can be eliminated and that the morphology and crystal structure of the iron pyrite films can be tuned to achieve uniform films composed of large grains/crystallites desirable for photovoltaic application. This technique was explored for Fe-precursors deposited with both electron-beam deposition (Chapter 4) and sputter deposition (Chapter 5).

Lastly a note on the chronology of the work. The chapters was completed in the following chronological order: 6, 5, 3 and 4. The ZnO work was pursued with the intent to test the limits of GLAD ZnO nanowire growth for mechanical energy scavenging electric generation. For this particular application, high-aspect ratios of $t/w > 100:1$ are required. It became clear during the work that these specifications were not achievable with the GLAD process, and so we changed focus to FeS_2 development. This explains the discontinuous jump between Chapters 5 and 6.

Chapter 2

Experimental methods

In this chapter, a brief overview of some of the experimental methods used in this thesis will be provided. Although the techniques presented here may be generally familiar to the reader, there are a few specialty techniques, such as x-ray diffraction pole-figures and image analysis, that would benefit from a brief review or introduction.

2.1 GLAD deposition systems

A GLAD deposition system has two major requirements that are uncommon in physical vapour deposition systems. These are

1. Dynamic control over substrate rotation during growth
2. A directional, collimated vapour flux

The geometry of a typical GLAD system is illustrated in Figure 2.1. The substrate is placed above the source material. Two stepper motors control the azimuthal angle (ϕ) and the angle of inclination (α) of the substrate. Often the stepper motors are controlled by software running on a computer connected to the system. More advanced setups incorporate feedback from film thickness monitors to allow the motion of the substrate to be triggered at precise stages during growth [60].

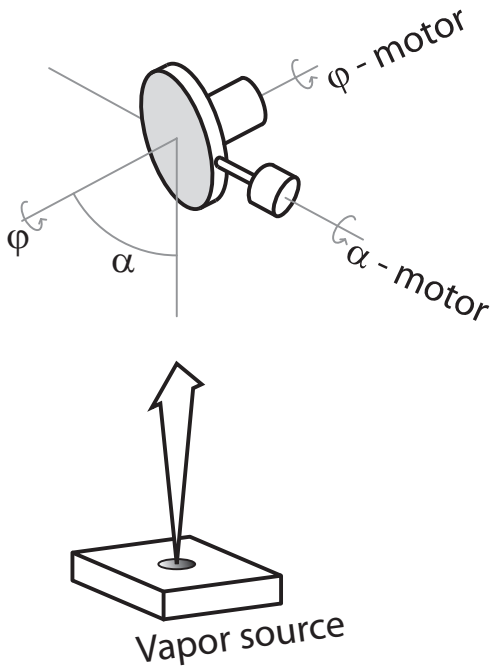

Figure 2.1: Schematic illustration of a GLAD deposition system showing the deposition angle α and azimuthal rotation angle ϕ that allow for arbitrary orientation of the substrate chuck relative to the incoming vapour source. Reprinted with permission from [4].

To meet the second requirement, thermalization of the vapour source must be avoided; that is, the directionality of the flux must be preserved. Generally, the flux is produced from a 'point' source to reduce the angular distribution of flux arriving at the substrate. To preserve directionality of the flux during transit, the mean-free-path (λ) of the flux particles must be larger than the characteristic size of the system (L), which can be defined as the chamber size or the throw distance (distance between the source and the substrate). Expressed mathematically, the flux must have a Knudsen number $K_n = \lambda/L > 1$ [19]. To achieve this deposition often occurs at high-vacuum pressures (<100 mPa) or even lower where the mean-free-path can be in excess of 1 m.

In other physical systems where the particle flux is composed of heavier particles, such as droplets, colloids, or molecules, it may be possible to maintain the directionality of the flux at higher pressures where the reduced mean-free-path may be possible. This is due to the larger momentum of these particles and the smaller effect that collisions with gas during transit have on the direction of motion. A real life example of this effect is rime ice. This phenomena occurs at atmospheric pressures when high-wind speeds direct super-cooled water droplets onto a substrate upon which they condense into a columnar morphology reminiscent of a GLAD structure [160, 161, 162].

Modern GLAD systems, including those within the Brett group, have extended capabilities with additional equipment such as ion guns and substrate temperature control. Additional equipment can be used to modify or monitor the film growth. For example, an ion beam can be used to alter the structure via re-sputtering and/or heating,[163, 164, 165] substrate cooling can be used to improve structuring[166, 167, 168, 4] and elevated substrate temperatures can be used to encourage crystalline growth or enable VLS growth modes [102].

There are several techniques to generate a particle flux in a physical vapour deposition system. The two main methods used in this thesis are electron-beam evaporation and sputtering. However, other methods can be used with GLAD including thermal evaporation, pulsed laser deposition, and spray/nozzle deposition [4].

2.1.1 Electron beam deposition

The vapour flux is produced by heating a crucible full of source material with an 10 mA to 100 mA electron beam. Electrons are generated by thermionic emission, accelerated through a high-voltage field, and then directed to the source with electromagnetic fields. By sweeping the electron beam across the source, the heat distribution can be tailored to accommodate different materials [19, 4]. Upon sufficient heating the source material's vapour pressure will exceed the hydrostatic pressure within the chamber and produce a vapour flux [19].

Of importance to GLAD, an electron-beam system tends to produce a vapour flux that is highly collimated ($\Delta\theta < 2°$) due to the small size of the source material ($\approx$ 10mm) and low deposition pressures ($P < 0.1$ mPa). The flux particles are not energetic with kinetic energy $E \approx$100 meV. This limits substrate heating when the vapour condenses to form a solid film. In turn, a reduced growth surface temperature helps to reduce surface diffusion. Note that radiative heating from the vapour source is still present.

2.1.2 Sputter deposition

A vapour flux in sputter deposition is created by bombarding heavy ions, typically argon, into a solid target material. A momentum transfer process leads to ejection of target atoms that form the flux. The ions are created by lighting a gas plasma in the chamber. Positively charged ions are then accelerated into the target due to a negative potential applied to the target [19].

A considerable advantage of sputtering is that virtually any material, including composite materials, can be sputtered. In addition, the deposited thin films have nearly the same relative composition of elements as in the source material although oxides and nitrides can be problematic [19]. This is a useful feature, as the stoichiometry of composite materials is often critical to their functionality.

Before the advantages of a wide material selection and composition control offered by sputtering can be realized in GLAD several issues must first be addressed. The use of a plasma to generate ions is problematic for GLAD

as it necessitates higher pressures than electron-beam deposition. It is not uncommon for sputter deposition to occur at pressures above 10 Pa. Another issue in sputter deposition is that the target sizes tend to be large, which produces a broader angular distribution within the flux ($\Delta\theta > 10°$). Kinetic energies of $\approx 10eV$ can also exists within the flux generated by sputter deposition. Thus significant substrate heating can occur as the adatoms condense and thermalize on the substrate.

Attempts to improve the suitability of sputtering for GLAD include the use of collimating plates, long-throw distances, magnetron sources, and hollow-cathodes that provide additional electrons by thermionic emission which reduces the pressure required to sustain a sputter plasma [169, 4, 19]. In Chapter 6, most of these techniques were used for ZnO sputter deposition. A collimating plate was avoided as it reduces the flux rate significantly and the flux rates for ZnO were already low enough to require >24 hr deposition times.

2.2 X-ray diffraction

Detailed introductions to x-ray diffraction (XRD) as a technique for thin film characterization can be found elsewhere [170, 171]. A brief overview will be given here to refresh the reader. A familiarity with diffraction, reciprocal space, and crystal structure are assumed.

X-ray diffraction is a technique that utilizes the coherent, elastic scattering of hard x-ray light ($\hbar\omega > 10$ keV or $\lambda < 0.2$ nm) to deduce information about the spatial positions of atoms in a crystal lattice. This is performed by diffracting x-rays off of a sample as illustrated in Figure 2.2. The angle of incidence of the incoming x-ray's is defined by ω, the angle of the diffracted beam by the angle 2θ and $\vec{Q}$ is the scattering vector. The diffraction angle, known as the Bragg angle, is related to the crystal plane spacing (d_{hkl}) by the Bragg law.

$$2d_{\mathrm{hkl}} sin\theta = n\lambda \tag{2.1}$$

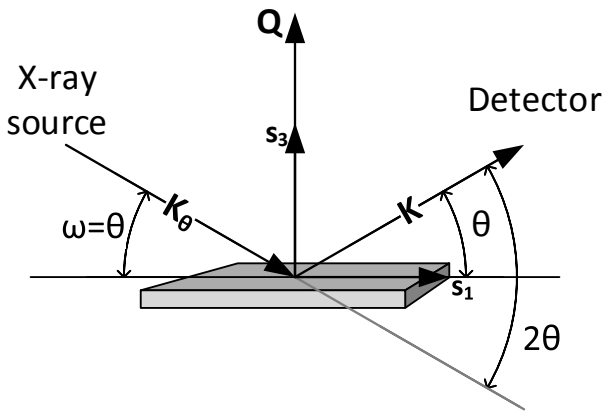

Figure 2.2: Schematic of Bragg reflection. Where the angle of incidence of the incoming x-ray's is defined by ω, the angle of the diffracted beam by the angle 2θ and $\vec{Q}$ is the scattering vector. K_θ and K are the incoming/outgoing x-ray wave-vectors.

Broadly speaking, crystalline materials can be broken up into three categories: polycrystalline with random crystallite orientations, polycrystalline with non-random crystallite orientations (textured), and single-crystal materials. These categories are illustrated in Figure 2.3. Thin films generally fall into the second category. This has important implications for the collection and interpretation of XRD data.

In a typical diffractometer (also called a 'goniometer') the angle of incidence of the incoming x-ray beam and the position of the detector can be varied independently. In this case the angle of incidence is sometimes referred to as ω. The most common use of XRD is the determination of crystal phase(s) of a material with a symmetric $\theta/2\theta$ scan. This is performed by rotating through all $\omega = \theta$ positions and recording the intensity of diffracted light $I(2\theta)$. The peaks in $I(2\theta)$ provide a fingerprint of the material phases within the sample.

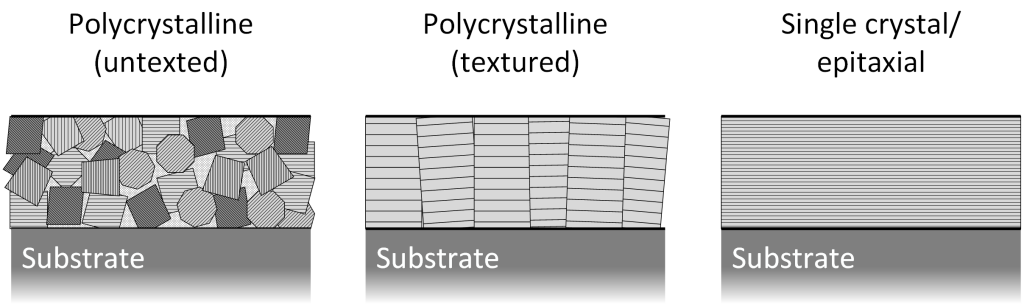

Figure 2.3: Illustration of the crystallite spatial orientations inside crystalline thin films. Films can be polycrystalline with random orientations (untextured), polycrystalline with ordering (textured) and single crystal or epitaxial.

2.2.1 Grazing incidence x-ray diffraction

Symmetric scans can work well for thicker films but for thin films that are <100 nm thick some diffraction peaks may be undetectable due to lack of interaction between the x-rays and the film material. In this case, diffracted intensity can be improved using grazing incidence x-ray diffraction (GIXRD). In GIXRD the incoming x-ray beam is kept at a grazing angle of incidence so that $\omega \approx 1°$ and the path length of the x-ray through the film is increased thereby increasing the intensity of the diffracted light.

Whereas the scattering vector $\vec{Q}$ is always parallel to the substrate normal in a symmetric $\theta/2\theta$ scan it rotates in a GIXRD scan. Thus, $\vec{Q}$ may not be parallel to the reciprocal space vector for a particular set of crystal planes when the Bragg condition is met. Due to the rotation of $\vec{Q}$ GIXRD can introduce diffraction peaks from single-crystal substrates, such as Si wafers, that are not observed in the $\theta/2\theta$ configuration.

An example of this is shown in Figure 2.4a which was taken on Si (100) substrates with $\omega = 2°$. In this case the (004) Si diffraction peak at $2\theta_{Si_{004}} = 69°$ observed in a $\theta/2\theta$ scan is not present, instead the (311) Si peak is seen. The reason for this becomes clear in Figure 2.4, which shows that at the Bragg angle for the (004) Si peak that $\vec{Q}$ is not parallel to the $\langle 004 \rangle$ direction. However, the (311) Si diffraction peak does appear at $2\theta = 56°$ in this configuration, where the Bragg condition and $\vec{Q} \,||\, \langle 311 \rangle$ condition happen to be

met simultaneously.

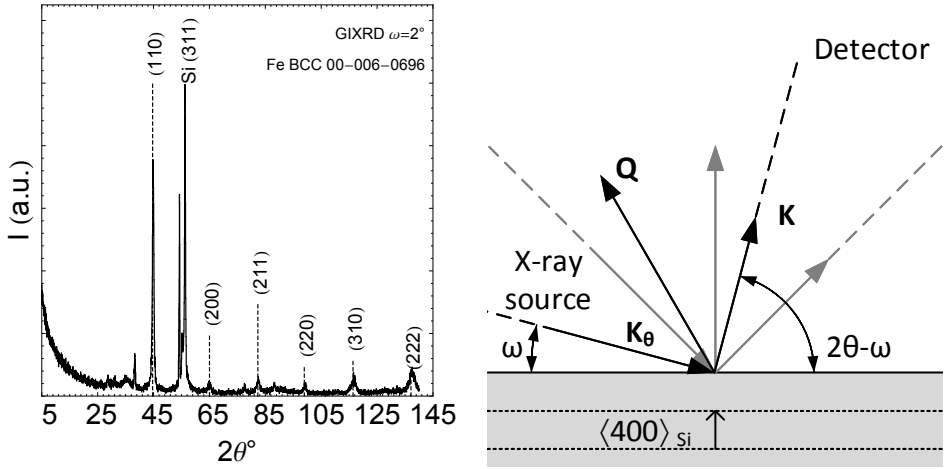

(a) (b)

Figure 2.4: (a) Grazing incidence x-ray diffraction pattern of a 1200 nm Fe film deposited at 1 nm pitch. Expected peaks for BCC iron (ICSD 00-006-0696) are shown for comparison. Reproduced here from Figure 3.5. (b) Geometric configuration of the x-ray beam when attempting to detect the Si (400) peak in the GIXRD configuration with $\omega = 2°$. Dark lines indicate the GIXRD configuration, and gray lines are for a $\theta/2\theta$ symmetric scan.

2.2.2 Texture determination with pole figures

As visualized in Figure 2.3, polycrystalline materials can exhibit preferential ordering of crystallite orientation, called a crystal texture or simply texture. Texture is classified by the number of degrees of constraint placed on crystallites in the sample. Constraint in one degree of freedom is referred to as fiber texture and constraints in two degrees of freedom is called as biaxial texture. Texturing can be viewed as intermediary steps between complete disorder in randomly oriented polycrystalline powder samples to highly ordered epitaxial thin films.

In fiber-textured thin films crystallites, are oriented preferentially along one axis, known as the fiber axis. Typically, the fiber axis corresponds to the substrate normal, either due to evolutionary selection of grain growth and/or

by the constraints imposed by the substrate plane and a grazing incident flux in GLAD [109, 26]. In thin films with biaxial texture, the two axes that define the crystallite constraints typically lie within the substrate plane and along the substrate normal. However, in principal any two independent axes are possible.

Texture manifests itself in a diffraction experiment as a non-isotropic distribution of intensity along a diffraction ring. This can be clearly seen from two-dimensional diffraction frames shown in Figure 2.5.

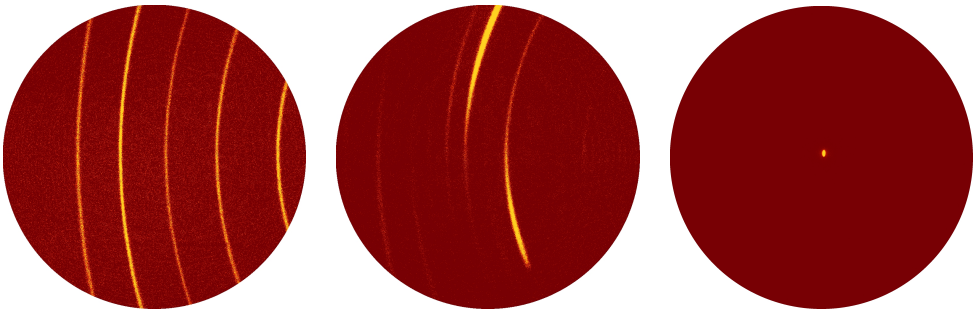

(a) (b) (c)

Figure 2.5: Two dimensional frames taken from the Bruker Discover D8 instrument at NINT. The Bragg angle θ_χ decreases from left to right. The three frames shown correspond to (a) a polycrystalline powder sample with isotropically distributed crystallites that produce uniform diffraction rings, (b) a polycrystalline textured thin film sample that shows intensity variation across the diffraction rings and (c) a single crystal Si wafer where diffracted intensity is localized to a small point.

A pole figure maps the spatial distribution of diffracted x-ray intensity in the hemisphere above the sample plane. In other words, for a given diffraction peak the pole figure provides a spatial map of $\vec{Q}$. These maps are typically drawn on a page using a stereographic projection. By measuring pole figures of at least three separate diffraction peaks the distribution of crystallite orientation in the sample can be determined uniquely [170].

2.3 Image analysis

Electron microscopy is a convenient method to study the microstructure and morphology of GLAD films. As a result, imaging is regularly performed to examine the film structure qualitatively and monitor the reproducibility of the deposition process.

Qualitative changes in the microstructure in response to changes in deposition parameters can be quickly made by assembling image surveys. In addition, simple quantitative measurements, like film thickness or post density, can be taken manually by a human observer. In our experience there can be significant variation in the judgments made by human observers evaluating the same set of images. To help place data acquired from images on a firmer footing, image processing and analysis can be used to systematically analyze electron micrographs. This technique also has the advantage of automating the evaluation process, so scaling from a handful to 100s of images becomes trivial. Ease of access to large image areas enables statistically significant sampling of the films across much larger areas than would be practical to perform manually.

In general, there are three basic steps required to characterize an electron micrograph and produce a usable measure.

1. Object segmentation; potential objects of interest are identified and isolated within the image.

2. Object classification; segmented objects are classified or filtered into groups.

3. Object measurement; measurements on the object shapes or ensemble of classified objects are made.

Items 1 and 3, segmentation and measurement, are tractable with off-the-shelf software packages such as Mathematica (Wolfram Research), MATLAB (Mathworks) and ImageJ (NIH) [172]. Object classification (or image recognition) requires sophisticated algorithmic techniques and remains an active research problem in computer science. Therefore, we made the pragmatic

decision to leave classification to a human observer. This approach avoids extensive algorithmic development and testing, but still benefits from enhanced productivity and objectivity enabled by machine segmentation and measurement.

The work within this thesis has focused on film thickness measurements, object counting, object area summation, object alignment, and some other basic measures. Many of these object measures are implemented in off-the-shelf software packages, such as Mathematica. Thus, the objective is to devise an algorithm for preparing and segmenting the image into separated objects that can be further processed and measured by the software package. An example of a plan-view SEM image of GLAD Fe posts and an array of segmented objects shown in Figure 2.6.

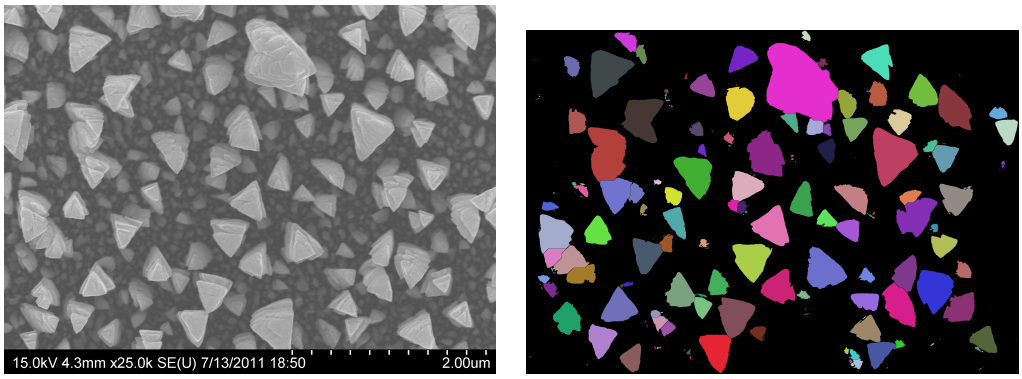

(a) (b)

Figure 2.6: (a) Example of an original plan-view image of an iron nanocolumn film (Chapter 3) that has been segmented (b). Each object is identified by a separate color.

An example from Chapter 3 will now be used to illustrate and introduce some of the concepts and image analysis techniques used within this thesis. Beyond the work presented in this thesis, these techniques have been extended in both internal[84] and external collaborations [173].

There are many texts discussing image processing and analysis available for the interested reader. Two that were particularly useful are "The Image Processing Handbook"[174] and "Hands-on Morphological Image Processing" [175]. The former provides a broad applications based overview of

image processing, and the latter introduces the algebra of mathematical morphology that forms the basis of several useful image processing methods. An extensive introduction to mathematical morphology will not be given here, but relevant concepts will be introduced as required.

2.3.1 Thresholding/binarization for object segmentation

Thresholding or binarization of a greyscale or color image is often used to segment objects. This works best when the pixel intensity histogram is bimodal with one population of pixels representing objects and another the background. Images used for analysis are taken normal to a cleaved film cross-section or normal to the substrate surface. In both cases the film material is typically 'whiter' than the substrate or vacuum. In plan-view images of very-thin films (<100 nm) the large depth of field of the scanning electron microscope can make it difficult to segment only the surviving posts and ignore extinct posts/nuclei at the base of the film. In these cases object classification can be used to select/filter the segmented objects later on.

There are several well-established algorithms that can be used to threshold images based on the pixel intensity histogram [174]. In this work we often used Otsu's clustering algorithm[7], which attempts to minimize the intra-class variance between the background and object pixel populations. In some cases we used other algorithms due to their superior segmentation performance. These included Kittler's minimum error algorithm[176] and Kapur's entropy maximum[177]. These algorithms differ in the metric used to define the threshold, but often produce threshold values that are within $\approx$ 10 intensity levels of each other (for 8-bit images, $2^8 = 256$ intensity levels).

A segmentation example is shown in Figure 2.7. Before performing the binarization step the original image is processed to enhance the edge contrast, remove noise, and increase the dynamic range. Image enhancement can serve two purposes, to assist a human observer in manual analysis or classification by highlighting key features or to prepare images for automated

image processing. The pixel intensity histogram in Figure 2.7 clearly shows a bimodal distribution, and the threshold value determined by Otsu's clustering algorithm[7] is marked between these two populations. Note that the binary mask is imperfect and contains unwanted objects and segmentation errors. These will be dealt with in further processing steps.

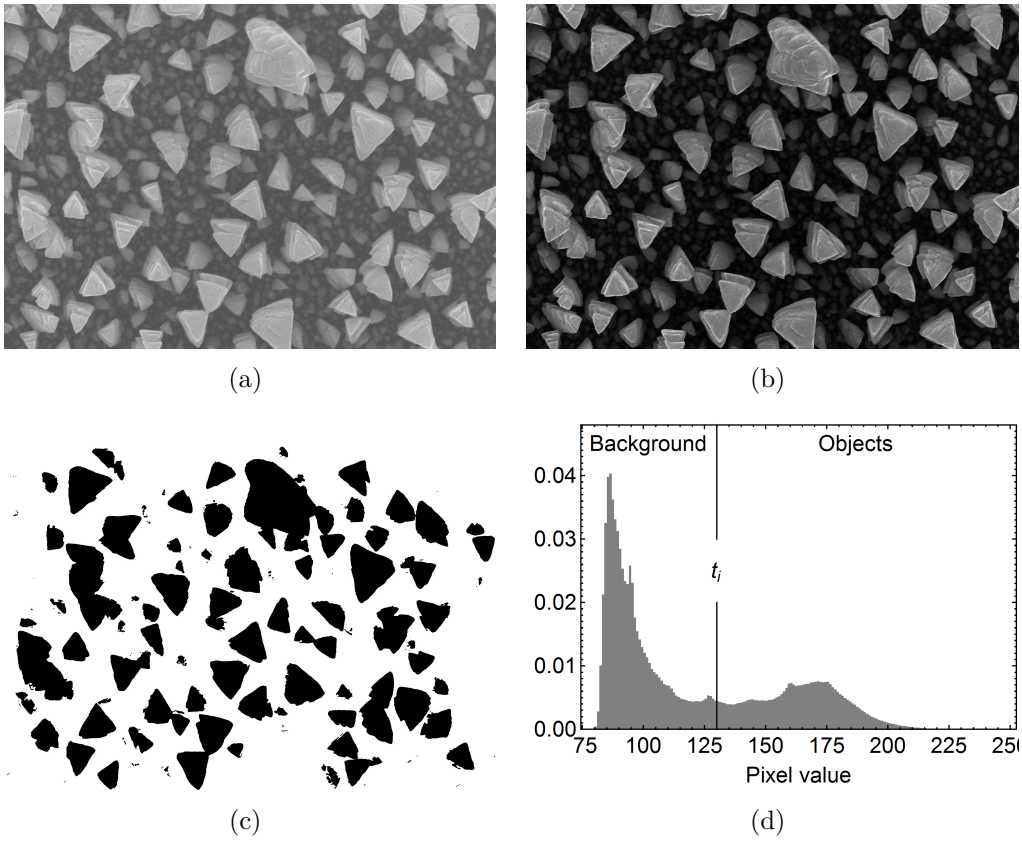

Figure 2.7: (a) SEM image from Figure 2.6a cropped to remove the scale bar. (b) The same SEM image after image and edge enhancement. (c) Thresholded binary image. (d) Pixel intensity histogram for the image in (d) and the threshold value found by applying Otsu's clustering algorithm [7].

2.3.2 Watershed transform for splitting conjoined objects

The watershed transform[178] is often used to separate conjoined objects in a binary image or segment objects from a greyscale image. The binary image in Figure 2.7c has several cases where two segmented objects are conjoined. For example, two conjoined triangular posts objects are shown in Figure 2.8a. This is a common problem when thresholding tightly packed objects. When the conjoined objects have a convex intersection the watershed transform can be used to define boundaries to separate them [174].

A greyscale image can be represented as a surface topology map, with pixel intensity values representing height. Conceptually, the watershed transform produces a boundary by flooding the valleys of this topology. The boundary is defined as the interface between any two basins after sufficient flooding. Successful application of the watershed transform thus requires 1) markers to define the initial flooding points and 2) an image to process.

To prepare a suitable image for the watershed transform a Euclidean distance transform can be used to produce a surface topology map from a binary mask. Each pixel within an object is replaced with a value corresponding to its distance from the boundary; larger values are given to pixels further away from the boundary. Thus, the centers of each object are given the largest values. Now the output of the distance transform can be viewed as a topology map, where pixel values correspond to the valley depth (Figure 2.8b). To define the initial points of flooding for the watershed, ultimate erosion points are often used. The ultimate erosion points are produced by eroding (removing) pixels from each object's boundary, until a object with 1-pixel width remains (i.e., a point or a line segment). In effect, this creates markers that are located within the region of the valleys produced by the distance transform (Figure 2.8c). These two images of 1) valleys produced by the distance transform, and 2) markers corresponding to the ultimate erosion points are inputs for the watershed transform. The watershed transform then produces a boundary mask, which can be overlaid onto the original binary image to separate the conjoined objects as seen in Figure 2.8d.

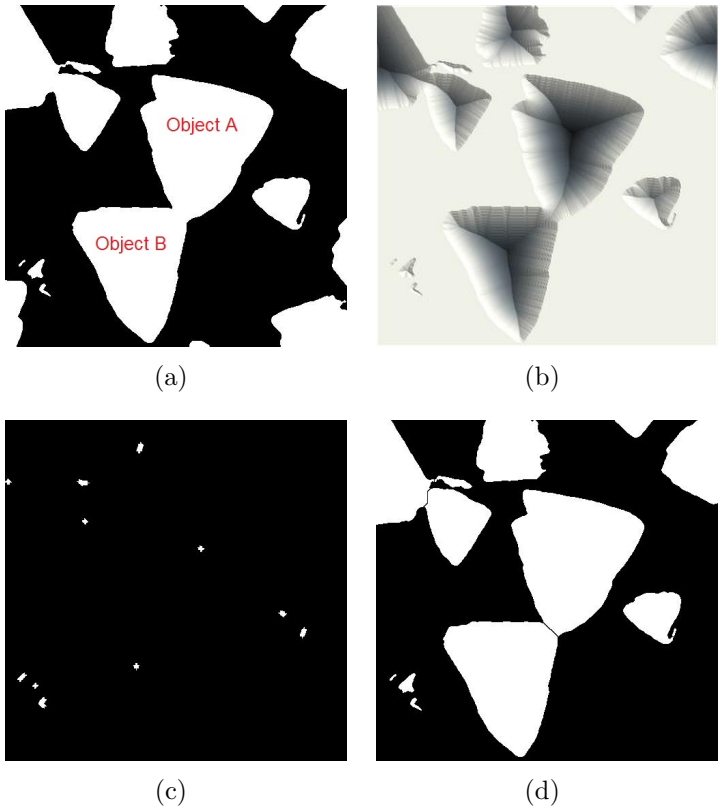

Figure 2.8: Demonstration of the conjoined object separation, such as the two triangular objects (A & B) shown in (a). A distance transform is computed to create a source image with the appropriate topology shown in a relief plot for perspective in (b). The ultimate erosion points are also produced from the original binary mask to create a marker for the initial flooding locations (c). The points in (c) have been dilated with a cross-matrix for presentation. After the watershed transform is used to compute the boundaries, they can be overlaid on the original objects to separate them as in (d).

2.3.3 Extracting human classified objects with geodesic dilation

There may be unwanted objects in the segmented images. Object classification can be used to filter the objects into several groups for measurement. It may be possible to classify objects algorithmically if strong clustering of the object properties is present (e.g., color, circularity, area). Principle component analysis can be used to find grouping across several properties [174]. In cases where strong clustering is difficult to achieve, a human observer can be used to classify the objects instead.

To assist the human observer, it is often easiest to examine the original or enhanced images. In this case, it is useful to allow rapid identification of objects within the greyscale image, and use those choices to select for segmented objects from a binary mask. To achieve this we have allowed a human observer to identify objects within ImageJ[172] by placing single pixel markers in an overlay. This overlay can then be exported and used to select segmented objects in a binary mask by using a geodesic dilation; the markers are dilated (increased in size) under the constraint of the mask shape. The result is that only objects with a marker within their interior are selected (Figure 2.9). Further refinement of the classification can be achieved by evaluating the binary masks and selecting objects with a color fill tool in ImageJ[172] or any other any image editing tool.

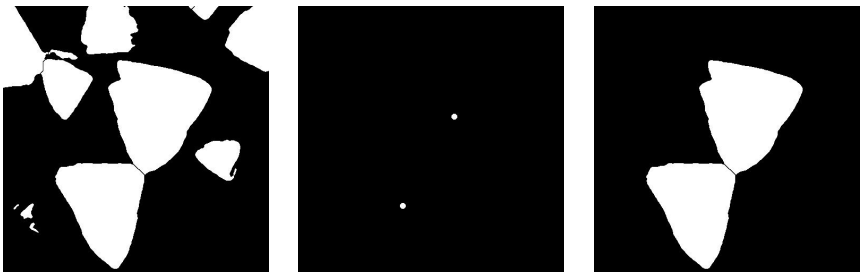

(a) (b) (c)

Figure 2.9: Demonstration of object selection with geodesic dilation. The source image is shown in (a). Markers are defined either by a human observer or by an algorithmic process (b). Application of the geodesic dilation selects only the marked objects (c).

Chapter 3

Flux engineering of iron nanocolumns

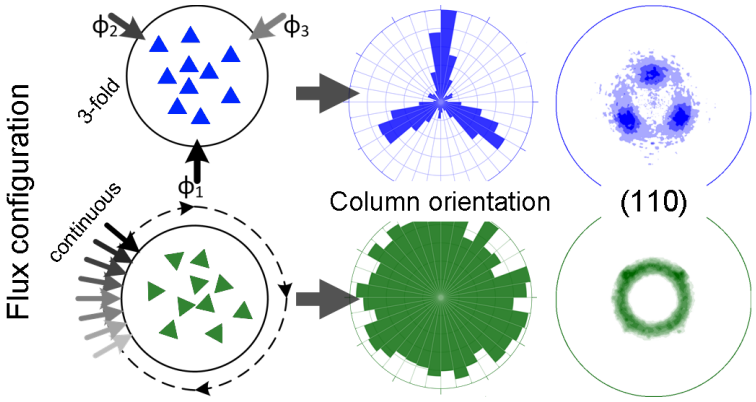

We show that it is possible to induce in-plane crystal texture morphological orientation by engineering the azimuthal distribution of the flux to match the symmetry of faceted iron nanocolumns. Thus we can create biaxially textured nanocolumns with an in-plane alignment that is controlled by the flux configuration. The work in this chapter was published in *ACS Crystal Growth & Design* in 2012 [179].

3.1 Introduction

GLAD is a nanostructured thin film fabrication process that can produce helical, chevron, and columnar nanorod arrays [41, 4, 42, 43]. The distinguishing feature of GLAD, compared to other nanostructuring techniques, is the use of a collimated vapour flux that sculpts the film growth front through substrate motion in a regime of ballistic self-shadowing induced at highly oblique angles ($\alpha > 70°$, defined between flux direction and substrate normal). In the literature, GLAD is often used interchangeably with the terms oblique angle deposition (OAD) [85] or inclined substrate deposition (ISB) [98], although these terms can also be used to describe techniques where the deposition angle is less than 70°. In the first generation of GLAD techniques, substrate motion was limited to continuous rotations around the substrate normal. With this class of motion, control of the columnar structure on the 10 nm to 50 nm scale is possible, which enabled applications that rely on the inter-column structure on the 100 nm scale. Such applications include optical devices [61], chemical and biological sensors [64, 65, 66] and mechanical pressure sensors [67].

To improve control over the intra-column structure, the second generation of GLAD techniques (Figure 3.1) has incorporated more complex substrate motions during film growth. Typically, this involves modulation of either the azimuth or angle of inclination during film growth. Techniques such as phi-sweep [77], substrate swing [180], spin-pause [181], and alpha-modulation [29] have been developed. Second generation GLAD nanostructures can be used in applications which were too demanding for the first generation, including square-spiral photonic crystals [63] and precisely engineered birefringent thin films [62].

The first two generations of GLAD technology have primarily focused on flux engineering to sculpt nanostructured morphology under conditions of limited surface diffusion. Third-generation GLAD techniques combine growth kinetics and flux engineering to design nanostructures with desirable morphological and crystalline properties. Work towards the third generation began with reports of crystalline GLAD films [43, 78, 79], followed by material specific studies (CrN [96], Ge [88], Mg [89], MgF_2 [97], Sn [91], YSZ [80, 100],

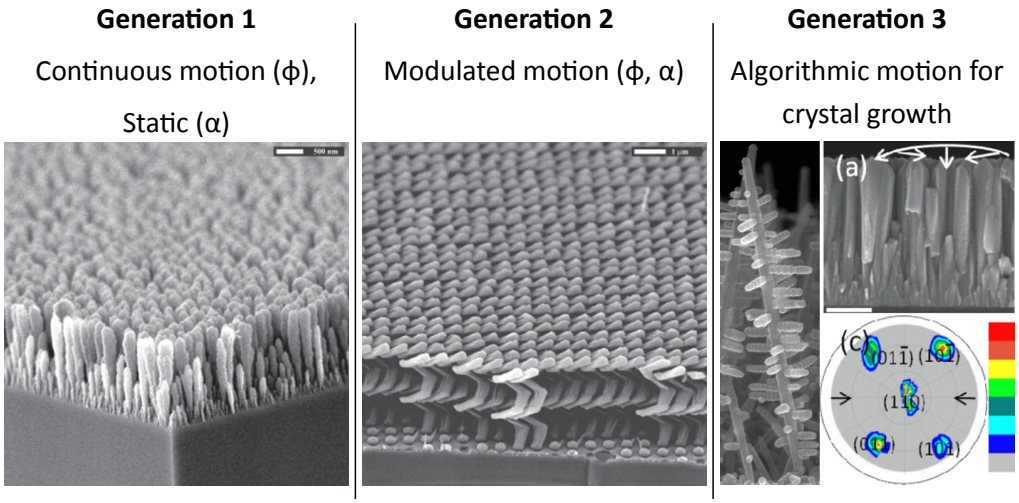

Figure 3.1: Examples of the three generations of GLAD technology. Parts reprinted with permission from [8]. Copyright 2012, American Institute of Physics. Parts reprinted with permission from [9].

ZnO [101, 81]). Several groups reported on the influence of pitch, the amount of the film growth along the substrate normal per substrate rotation, and on the morphology and crystallinity of GLAD films [4, 80, 81, 82, 83]. In parallel, the use of GLAD to influence crystal texture through evolutionary selection was under investigation in a variety of material systems including CaF_2 [95], Cu [85, 67, 82, 86, 87], MgO [98, 99], Ru [90, 83], W[92, 93, 94]. More recently, flux shadowing in GLAD has improved morphological control of vapor-liquid-solid (VLS) grown nanostructures [102, 103, 104]. Electric, magnetic, and optical properties are influenced by the morphology and crystallinity of nanostructured films. Therefore, advanced control over the crystallinity and morphology should improve a variety of device applications. Benefits of third-generation GLAD films have already been demonstrated with enhanced field-emission from faceted structures[182] and biaxial textured buffer layers used to grow crystalline semiconductor films on amorphous substrates [99, 183, 184]. As the third generation develops, GLAD may become a useful platform technology for several applications such as solar power, fuel cells and batteries.

In this chapter, we use Fe GLAD nanocolumns to demonstrate the level

of morphological and crystal texture control possible by engineering the azimuthal motion of the collimated vapor flux without changing the other deposition parameters. Previous work on oblique deposition of Fe has used stationary substrates or first-generation motions to characterize the role of deposition angle, deposition rate, pressure, and temperature in determining the magnetic anisotropies, column tilt angle and crystal texture of Fe nanocolumns [123, 124, 125, 126, 127, 128, 129, 130]. Pitch is known to affect development of crystallinity and has an obvious affect on morphology where vertical posts form at small pitches ($\approx$1nm) and helices at large-pitches (≈ 100 nm). We have characterized the effect of pitch on this system over 4-orders of magnitude to determine the regime of crystalline growth. Under continuous substrate rotation and a pitch <5 nm, crystalline Fe nanocolumns that have a faceted, tetrahedral apex are formed. Relative to the substrate surface, the columns have an out-of-plane crystal orientation, but no in-plane orientation (fiber texture). The 3-fold azimuthal symmetry of the columns provides an opportunity to induce in-plane orientation by changing the evolutionary selection dynamics during film growth. We accomplish this by designing the flux to also have an azimuthal 3-fold symmetry. The resulting films retain the out-of-plane crystal orientation but now also possess in-plane orientation of their morphology and crystal texture, and thus have biaxial texture. Furthermore the alignment of in-plane orientation is determined solely by the flux configuration (Figure 3.2); this is not an epitaxial effect but rather produced by directing the self-organized growth through engineering the positions of the incoming flux. Engineering algorithmic flux motions has the potential for extending the quality and control of GLAD microstructures in both ballistic and guided (e.g., vapor-liquid-solid) growth.

3.2 Experimental Details

The deposition system used in this work was a custom, high-vacuum, electron beam deposition system (Kurt J. Lesker AXXIS). Elemental iron (cylindrical pieces 3 mm to 6 mm in length, 99.95% purity, Kurt J. Lesker) was deposited on the native oxide of Si (100) substrates (test grade, single-sided polished, $\rho < 100\,\Omega \cdot$ cm, University Wafer) positioned 42 cm away from the source.

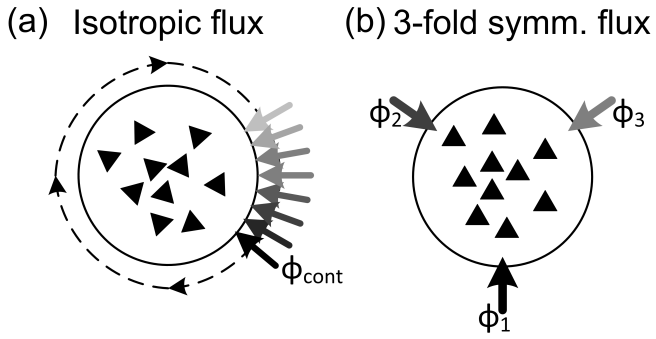

Figure 3.2: Schematic of the two flux patterns used. Continuous substrate rotation in (a) led to isotropically orientated columns with fiber texture. Moving the substrate through a 3-fold symmetric pattern in (b) produces preferential orientation in the triangular columns and a biaxial texture.

Before deposition, substrates were cleaned by sonication in de-ionized water, then rinsed with acetone and isopropanol, and finally dried with a jet of clean dry air. Deposition commenced after the chamber pressure was below 0.3 mPa and was kept near that value during film growth. An electron beam with spot size of 1.5 cm in diameter created a localized melt in the crucible. A quartz crystal thickness monitor (Maxtex SC-105) reported the nominal flux rate, which was maintained at $(0W.1 \pm 0.01)\,\mathrm{nm \cdot s^{-1}}$ by adjusting the beam current. Substrate motion control was achieved with two stepper motors that controlled the vapour flux incidence angle (α), and azimuth (ϕ). All films reported here were deposited at $\alpha = 88°$, measured relative to the substrate normal. Deposited film thicknesses were between 20 nm and 1200 nm; deposition pitches were between 0.1 nm and 500 nm. We also define a flux azimuthal symmetry parameter (FASP), which corresponds to the number of stopping points around one complete rotation of the substrate. A traditional vertical column would have an FASP = 0 (see Figure 1a), representing a continuous rotation around the substrate normal. A serial bi-deposition film[61] or substrate-swing[93, 94] would have a FASP = 2, and we use a deposition with a FASP of three (see Figure 3.2b) here to achieve a 3-fold symmetric flux distribution. Films deposited at a FASP = 3 were limited by the rotation speed of the chuck to a 2 nm pitch. Details of the substrate motion control used for the FASP = 3 films, including an example

motion file, are presented in Appendix A.

Number density, areal density, and orientation of the faceted, triangular columns (Figure 3.4a, b) were determined from image analysis of plan view scanning electron microscope (SEM) images taken with a Hitachi S4800. Each image analyzed corresponds to a different section of the film by translating the field of view to avoid double counting. Number density (columns per unit area) and areal density (column area per unit area) were determined using a combination of human observers and machine processing routines. Human observers marked triangular, faceted columns with the multi-point tool in ImageJ [172]. Two observers processed a significant subset of the images and the counts from each observer were highly correlated. Changes in observer should not affect the reported trends. After applying an edge-enhancing filter and median filter for noise reduction to the original image, a thresholding routine implemented in Mathematica 8.0.4 (Wolfram Research) segmented the images to produce a binary mask of object candidates. Details of this process were discussed in Section 2.3. We discarded objects intersecting the field-of-view boundary. Conjoined objects are a common problem seen when thresholding images containing densely packed convex features. To separate conjoined objects we applied a boundary computed from a marker-based watershed transform of the Euclidean distance transform (input) and the ultimate-erosion points (marker) of the binary image [174]. Finally, a geodesic dilation of the binary mask and marker produced in ImageJ selected objects identified as faceted columns. These concepts were introduced in Section 2.3 and Mathematica code samples for processing the images is provided in Appendix B.

When computing the number density, we compensated for the difference in likelihood between a large object and a small object intersecting the boundary and being discarded from further counting by using a standard adjusted count[174] for each object. The adjusted count is defined as

$$N_{adjusted} = \sum_{objects} \frac{W_x W_y}{(W_x - F_x)(W_y - F_y)} \tag{3.1}$$

where $W_{x,y}$ are the width and height of image and $F_{x,y}$ are the width and height of the object. Thus, a larger object is weighted more heavily as it is

more likely to have intersected the image boundary and been discarded from further analysis. To calculate the number density (ρ_N) and areal density (ρ_A) for each sample we used the following equations

$$\rho_N = \sum_{images} \frac{N_{adjusted}}{A_{image}} \tag{3.2}$$

$$\rho_A = \sum_{images} \frac{N_{adjusted}}{N} \frac{\sum_{objects} A_{object}}{A_{image}} \tag{3.3}$$

The sums occur over all the SEM images taken for that sample, where A_{image} is the entire image area (field-of-view) and A_{object} is an object area for one column. We measured the triangular column orientation from the angles of line-segments placed to outline the cross-section of each column in ImageJ. In cases where the triangular cross section was distorted due to intra-column shadowing, seen in FASP = 3 films, a line-segment was placed to connect the vertices, as shown in Figure 3.3. Orientation histograms were produced by compiling orientation data from all the images taken of a film.

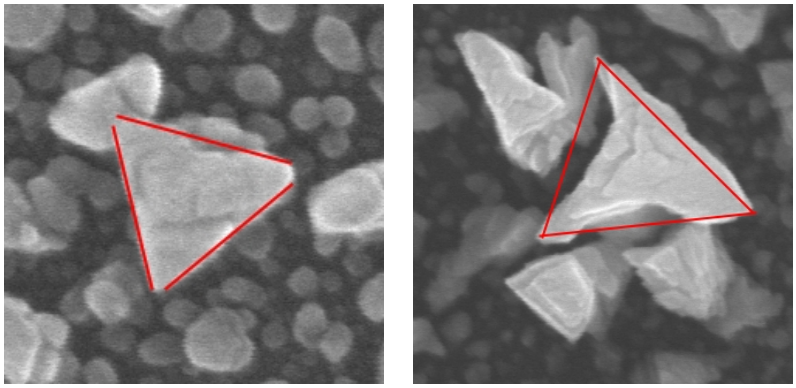

(a) (b)

Figure 3.3: Line segment traces (red lines) for well-formed (a) and malformed (b) trianglur Fe posts. Notice the identations on the sides of the post in (b) that are likely caused by the shadowing of the adjacement objects.

X-ray diffraction (XRD) profiles were taken with a Rigaku Ultima IV using a Cu Kα source in grazing-incidence ($\omega = 2°$) configuration and a monochromator to remove Fe fluorescence. A Bruker D8 Discover using a

Cu Kα source, 0.5 mm collimator, Bruker HiStar area detector at a distance of 15 cm measured the pole-figures. Transmission electron microscopy (TEM) was used to image select Fe nanocolumns, and to further analyze their crystal structure with selected area electron diffraction (SAED) on a JEOL 2200 FS and Hitachi H9500.

3.3 Results

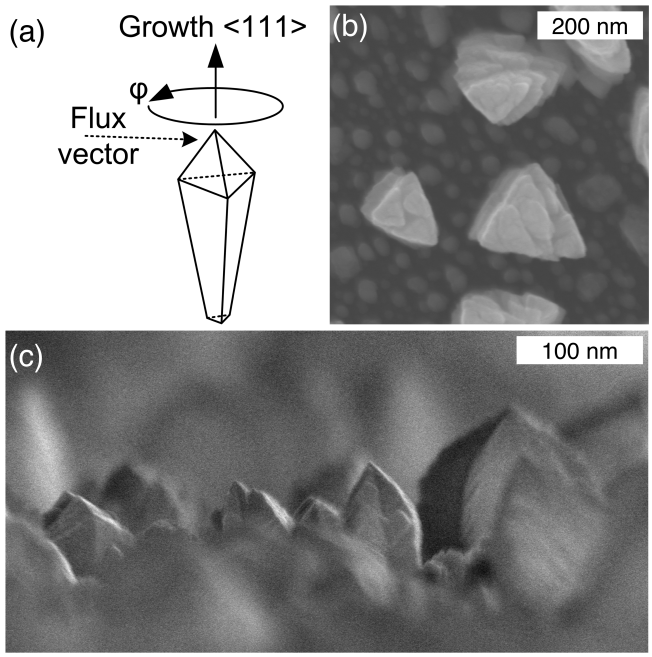

Figure 3.4: Schematic of a nanocolumn and the incoming flux (a). Two representative SEM images of the nanocolumns taken above the substrate plane (b) and at an oblique angle of 88° (c) demonstrate the tetrahedral, faceted apex of the nanocolumns and their triangular cross sections.

We used GLAD to implement engineered motion of the inclination and azimuthal angles of the Fe flux to control nanocolumn shape, crystallinity and texture. Iron nanocolumns deposited at a deposition angle $\alpha = 88°$ and 1 nm pitch (continuous rotation) as shown in the growth schematic Figure 3.2a exhibit faceted morphology with a triangular cross-section as seen in the SEM images shown in Figure 3.4. The faceted shape and triangular cross

section are indicative of a cubic crystal structure where the $\langle 111 \rangle$ direction is aligned parallel to the growth direction as seen in Figure 3.4a. X-ray diffraction confirmed the crystalline nature of the nanocolumn films. A sample diffraction pattern from a 1200 nm thick film in Figure 3.5 matches well with the BCC iron structure (ICSD 00-006-0696). The diffraction profile was taken in a grazing-incidence configuration ($\omega = 2°$) to measure peaks absent in the $\theta/2\theta$ symmetric configuration. A peak at $2\theta = 56°$ is attributed to Si (311) which is expected in the grazing-incidence configuration used with Si (100) wafers. The remaining peaks at 2θ values of 35°, 38°, 54°, 77° and 88° cannot be accurately identified, but are likely due to iron oxide phases (Fe_2O_3 and Fe_3O_4) since the films were exposed to the ambient environment before diffraction measurements were made allowing for oxidation of exposed surfaces within the film. High-resoluation TEM imagery of the nanocolumns reveal a $\sim$5 nm surface layer as seen in Figure 3.6, which is consistent with surface oxidation. Diffraction patterns for films ranging in thickness from 50 nm to 1200 nm all showed peaks consistent with an iron BCC structure.

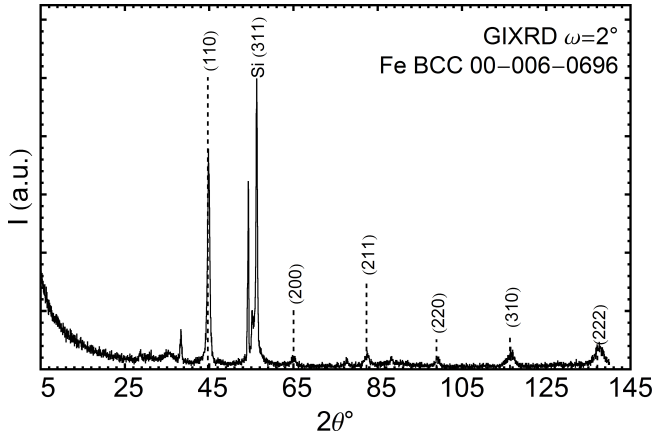

Figure 3.5: X-ray diffraction pattern of a 1200 nm Fe film deposited at 1 nm pitch taken at a grazing incidence. Expected peaks for BCC iron (ICSD 00-006-0696) are shown for comparison.

The faceted, tetrahedral apex of the crystalline nanocolumns suggests that the nanocolumns are textured with the growth-axis parallel to the $\langle 111 \rangle$ direction, as that crystal geometry can produce tetrahedral apices. An XRD pole-figure of the (110) diffraction peak shown in Figure 3.7f confirms that the

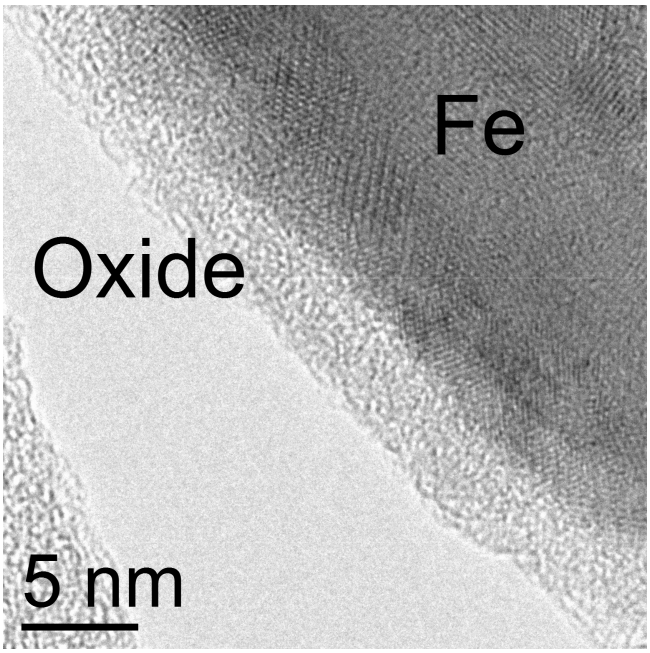

Figure 3.6: High-resolution TEM image of a Fe nanocolumn (deposited at a 1 nm pitch) that shows the oxide layer present on the surface.

nanocolumns are fiber-textured with the ⟨111⟩ parallel to the substrate normal. These results motivated an attempt to induce preferential orientation of the triangular cross sections and biaxial texture in the film via evolutionary selection of grains in the nucleation layer. We used a flux engineered to have a three-fold azimuthal symmetry (FASP = 3) to grow several films to a thickness of 500 nm with a pitch of 2 nm and compared them to films with a FASP = 0 with a pitch of 1 nm. Limited rotation speed of the motors in the deposition system prevented us from achieving an overall pitch of 1 nm in the FASP = 3 films. In each case, we measured the orientation of the triangular nanocolumn cross-sections and took XRD pole-figures shown in Figure 3.7. A flux with FASP = 3 produces triangular nanocolumns preferentially oriented across the film so that the normal of each edge is parallel to a flux vector as shown in Figure 3.7a. Visible in this figure is a small population of nanocolumns oriented in the inverse direction. Pole-figures for the (110), (200), and (211) seen in Figure 3.7b-d have 3-fold azimuthal symmetry. The positions of the peaks are in agreement with the expected positions (overlaid)

for an out-of-plane ⟨111⟩ texture. Azimuthal positions seen in pole-figures agree with the expected positions of the (110), (200), and (211) peaks for biaxial texture as illustrated in the schematic of Figure 3.7g. Together this data confirms that FASP = 3 flux is able to produce biaxial textured Fe nanocolumns denoted as $[111](\bar{1}10)$ in the common notation [26], where the square brackets indicates the out-of-plane direction and the parenthesis the crystal face parallel to the flux incidence plane. When a flux with FASP = 0 is used, azimuthal orientation of the nanocolumns (Figure 3.7e) and the in-plane texture are lost so that the nanocolumns only exhibit a fiber-texture (Figure 3.7f).

The lowest energy faces of the BCC structure in iron are the {110} planes followed by the {100} planes [185], so it is reasonable to expect the facets of the nanocolumn apex to be composed from one of these families. Measurements of the angle subtended by the nanocolumn apex from several SEM images produce values ranging between 75° to 105°, and no values as low as 60° were observed. The expected value for a {100} habit is 90°, whereas the {110} habit is 60°; our experimental results are consistent with the {100} interpretation. Previous experiments have also observed a {100} crystal habit [125, 129]. However, variations in the viewing angle will distort the measured angle, and a definitive measurement of the crystal habit will require further study.

As stated in the introduction, a complete picture of texture evolution[26, 107, 108] has yet to be developed. Contributing effects include the crystal geometry [90, 109], flux capture cross-section [100, 110], asymmetric surface diffusion [111], surface energy [100, 112, 92, 109, 113], and shadowing play a role [90]. Development of the in-plane texture is likely due to shadow-mediated competition between the nanocolumns, whereby columns with a faster vertical growth rate are able to out-compete columns that grow more slowly. Mechanisms for the out-of-plane texture appear more complex. Abelmann and Lodder[26] argue that a uniform distribution of adatoms is required for successful crystal growth. We propose that at low pitch, the combination of surface diffusion, presumed to be constant across our films, and rotation are able to distribute adatoms on the nanocolumn growth surface uniformly, enabling crystalline growth. The low energy surfaces (high-mobility) are the

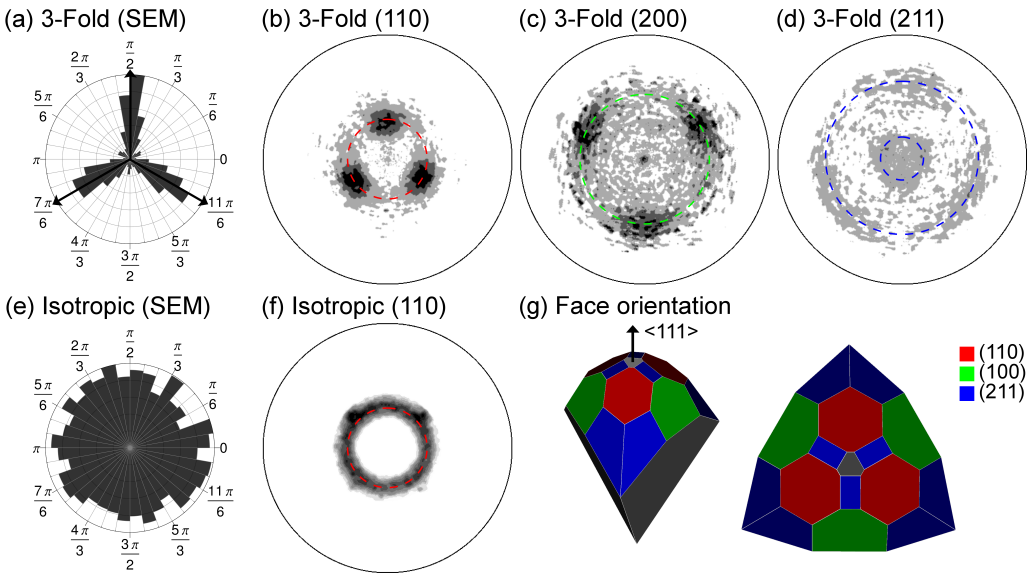

Figure 3.7: Sector plots show the azimuthal distribution of nanocolumn edge normals measured from plane view SEM images for a film deposited with 3-fold symmetric flux (FASP = 3) (a) and another film under continuous rotation (FASP = 0) (e). The radial distance of the sector plots corresponds linearly to the count of each 10° bin, with the largest bin count of 139 for (a) and 89 for (e) occurring at the circumference. Flux directions are overlaid on (a) for FASP = 3 and the pole figures in (b,c,d) for the same FASP=3 film have been oriented to have the identical flux orientations on the page. A pole-figure (f) for the FASP = 0 film shown in (e) demonstrates the loss of in-plane crystal orientation. A schematic of the crystal morphology of the BCC structure is shown in (g) from a perspective view and with the ⟨111⟩ direction normal to the page. Colors of red, green, blue indicate the crystal faces in the schematic. A label and colored line corresponding to the face in (g) has been added to each pole-figure (b,c,d,f) to indicate the expected peak position for ⟨111⟩ out-of-plane texture.

{100}, and {110} planes and the highest energy surface (low-mobility) is the {111} family of planes [185]. Therefore the observed out-of-plane orientation along the ⟨111⟩ direction is consistent with previous work, where surfaces with low-adatom mobility will define the fastest vertical growth direction due to enhanced adatom capture[100, 95, 92]. The facets of the pyramidal apex appear to be comprised of the {100} faces, which is a configuration that minimizes surface energy. With flux in the FASP = 3 configuration a $[111](\bar{1}10)$ orientation develops, which indicates that columns with the fastest vertical growth are oriented with their {100} faces directed towards the flux. One potential explanation is that crystallites with this azimuthal orientation receive a nearly uniform distribution of adatoms on their growth surface. Therefore these columns can continue to undergo textured growth and outcompete disoriented columns. However, a full understanding of the growth of these films and the development of biaxial texture will require further study and simulation.

Next we investigated FASP = 0 films to determine the effect pitch has on the film morphology, nanocolumn crystallinity, and the inter-column competitive dynamics due to shadowing. As mentioned above, the observed correlation between crystallinity and low pitch observed in GLAD films can be interpreted as the threshold where the combination of flux rotation around the growth front and surface diffusion are sufficient to distribute adatoms uniformly across the growth surface. The exact value of the pitch threshold will depend on the material, deposition temperature (surface diffusion), and other system parameters. A comparison between nanostructures deposited at pitch values of 1 nm and 500 nm shows the expected change from columnar morphology at 1 nm pitch to the helical morphology at 500 nm as seen in the TEM images in Figure 3.8. The lattice spacing displayed inset to Figure 3.8a matches the value for BCC iron expected from XRD. Selected area electron diffraction patterns inset on Figure 3.8 reveal high crystallinity at a pitch of 1 nm and a reduced crystalline character and amorphous structure at a pitch of 500 nm. Thus, the pitch threshold where crystalline growth is possible should exist between these two values.

Faceted nanocolumn number density provides a measure of the efficacy of the flux configuration to enable crystalline growth. This is possible be-

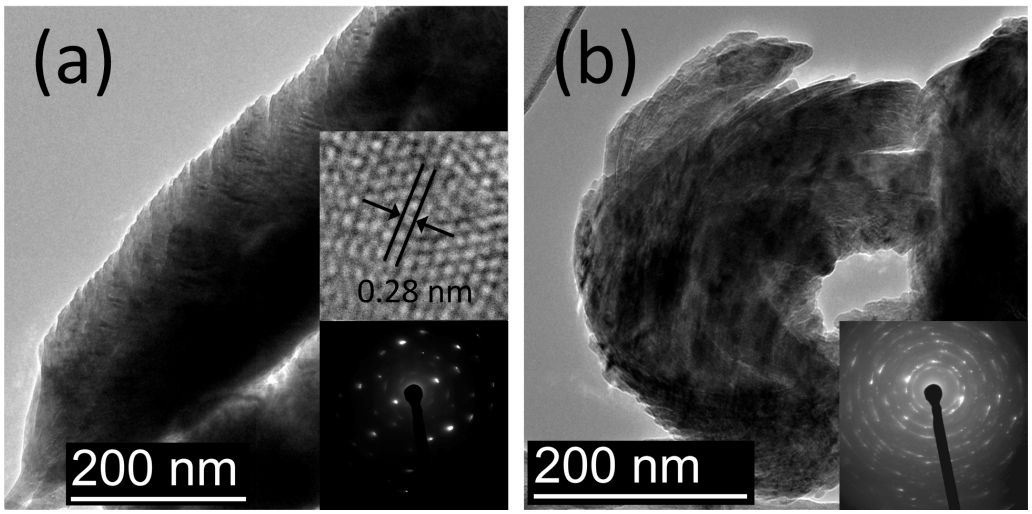

Figure 3.8: Bright-field TEM images of a nanocolumn deposited at a 1 nm pitch (a) and a helix deposited at a 500 nm pitch (b). Selected area electron diffraction images taken from each structure are shown inset on (a) and (b). Also a high-resolution lattice image is shown inset to (a).

cause faceted nanocolums, oriented along the $\langle 111 \rangle$ direction, are expected to grow more quickly than cylindrical nanocolumns. Thus the growth front becomes dominated by faceted nanocolumns, as observed in SEM images across a range of thicknesses. Number density data for films across four orders of magnitude in pitch, deposited at a nominal thickness of 50 nm are shown in Figure 3.9. We observe high faceted column density ($\approx 50\ \mu\text{m}^{-2}$) at low pitch, and low density ($\approx 3\ \mu\text{m}^{-2}$) at high pitch, with a transition occurring at around a pitch of 5 nm. The onset of faceted columns below 5 nm pitch suggests that under this threshold, the combination of flux rotation, which distributes the adatoms azimuthally and modulates their parallel momentum, in conjunction with surface diffusion is sufficient to uniformly distribute adatoms and thereby enable textured nanocolumn growth. In effect, at low pitch the collimated flux can simulate an azimuthally isotropic vapour source. Similar transitions of Fe nanocolumn crystal and morphological properties have been observed for a variety of deposition parameters that affect surface diffusion, such as temperature, pressure and deposition rate [124, 125, 26]. Above 50 nm pitch, these effects are unable to distribute the adatoms uniformly around columns, leading to a growth surface that

follows the slow rotation of the flux, and helical structures are developed.

Films grown at 10 nm pitch, slightly above the threshold determined in Figure 3.9, also exhibit a morphology dominated by triangular nanocolumns, although with rounded corners, in the thick-film limit reached at 500 nm of growth (Figure 3.10). Therefore, performing the same measurement shown in Figure 3.9 with thicker films will obscure the transition in pitch. This effect is clearly seen in Figure 3.11 where the triangular column density is plotted with film thickness for a series of films deposited at 1 nm and 10 nm pitch. Above 50 nm thickness, the column density difference between the series decreases until the series merge above 250 nm of total film growth. Inter-column shadowing produced at high deposition angles limits the surface area of the active growth front and drives the convergence between the two series in Figure 3.11 at large thicknesses. This convergence also occurs for the areal density of the series (not shown) as expected. Below 50 nm of thickness, shadow competition between the initial nuclei leads to evolutionary selection of crystallites with their fast growth direction, $\langle 111 \rangle$, oriented parallel to the substrate normal. Thus, oriented columns come to dominate the growing film. As the population grows and the cross-sectional area of each nanocolumn increases the shadowing limit begins to drive competition within the faceted nanocolumn population after 50 nm of film growth. Shadowing continues to provide a selection pressure so that only the fastest growing (textured) nanocolumns survive as the film continues to grow, which assists in the evolution of the crystal texture and morphological orientation presented in Figure 3.7 for 500 nm thick films.

3.4 Conclusion

Texture evolution studies in obliquely deposited Fe films have shown that deposition rate and pressure affect the development of fiber texture or biaxial texture [124, 125, 26]. Biaxial texture in other materials has also been demonstrated, and substrate motion can affect alignment of the biaxial texture so that the out-of-plane orientation is normal to the substrate or tilted into the substrate plane [93, 94]. We have shown that either fiber texture or

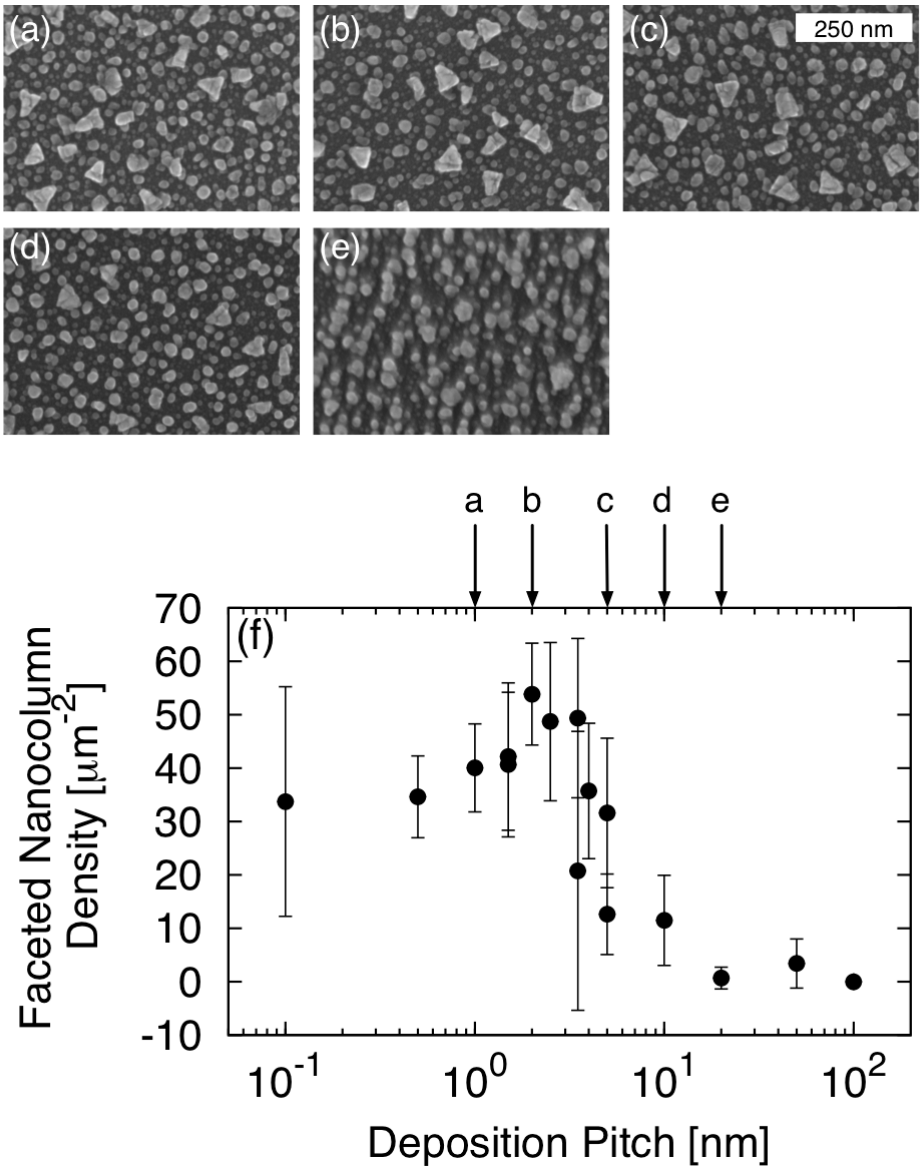

Figure 3.9: Density of faceted nanocolumns in 50 nm thick films as a function of deposition pitch. A pitch threshold occurs around 5 nm. At lower values the nanocolumns exhibit a triangular cross section, and at higher values faceting is lost and columns with a circular cross section become increasingly prevalent. Sample plane-view SEM images (a-e) at the pitch values indicated with arrows demonstrate the loss in triangular nanocolumns.

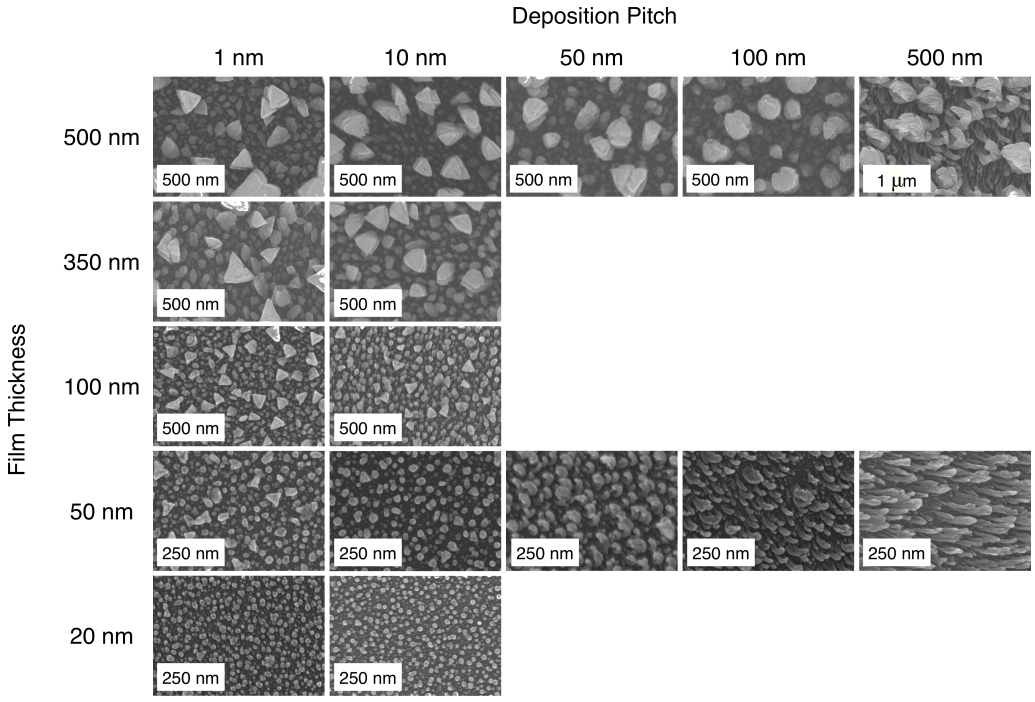

Figure 3.10: Plane view SEM images of Fe films deposited at different values of pitch (cplumns) and total film thickness (rows) are shown. The morphology moves from facetted at low pitch, to circular and finally to helices at large pitch. Note that facetted, triangular morphology develops at 10 nm pitch as the film grows.

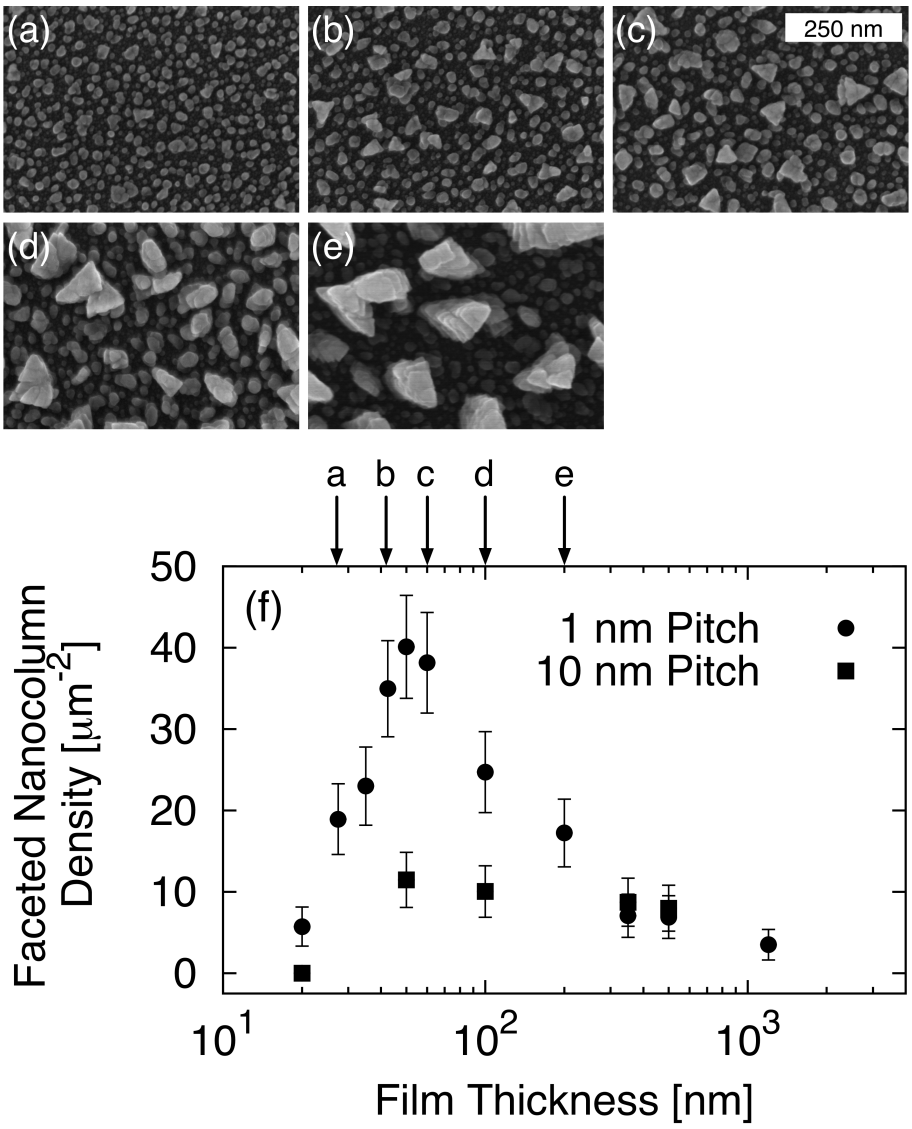

Figure 3.11: Faceted, triangular column density for 1 nm and 10 nm pitch films as a function of film thickness. Evolutionary selection drives the population increase in the fast-growing faceted nanocolumns up to 50 nm of film thickness. As growth continues, competition between the faceted nanocolumns begins and the population decreases. Eventually shadowing limits the density of columns and the two series merge. Plane-view SEM images (a-e) show the growth of the film for the 1 nm pitch series.

biaxial texture, both with ⟨111⟩ out-of-plane orientation normal to the substrate, can be developed by changing the flux azimuthal distribution. Continuous substrate rotation (azimuthally isotropic) produces a fiber texture. Matching the azimuthal symmetry of the flux to that of the nanocolumn morphology, produces in-plane orientation via evolutionary selection and results in a biaxial texture. Furthermore, an in-plane morphological orientation accompanies in-plane crystal orientation and the flux controls the alignment of both. Thus, the direction of in-plane orientation on the substrate is controlled by the flux configuration. Although we used nanocolumns with a 3-fold azimuthal symmetry, in principle orientation of 4-fold and 6-fold symmetric morphologies should be possible with this technique. Engineering the flux distribution to influence growth kinetics represents a third generation of GLAD techniques that can provide new opportunities for GLAD where control of crystal texture, faceting, and grain size enhance device performance in applications like piezoelectric energy scavenging devices and structured electrodes for solar and energy storage.

In the following chapters, we will use these nanocolumn arrays as precursors for iron pyrite formation. The control over the nanocolumn density developed here, through the deposition angle, will be shown to play a critical role in influencing the microstructure of the iron pyrite films.

Chapter 4

Control of iron pyrite thin film microstructure by sulfurization of columnar iron precursors

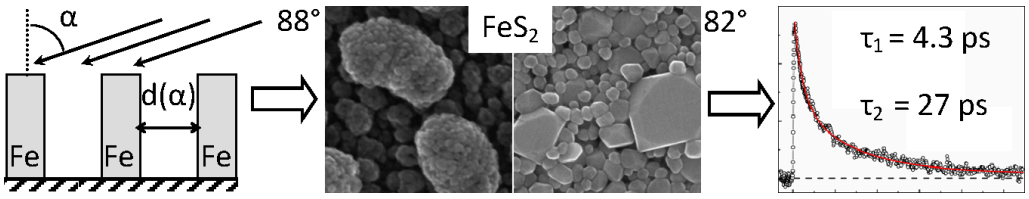

We now use the techniques established in the previous chapter to produce large-grained, uniform, crack-free iron pyrite thin films. These films are produced by sulfur-annealing the iron films in a process termed 'sulfurization'. Void-fraction of the precursor films controls iron pyrite microstructure (e.g., crystallite size, morphology) and can eliminate cracking or buckling. Composition, electronic properties and photocarrier dynamics relevant to photovoltaics are presented. This chapter was published in *Solar Energy Materials and Solar Cells* [186].

4.1 Introduction

Iron pyrite is an indirect band gap (0.95 eV) semiconductor material with high optical absorption ($\alpha_o > 10^5\,\mathrm{cm}^{-1}$ for $h\nu > 1.3\,\mathrm{eV}$), which results in an absorption length ($L_o = 1/\alpha_o$) that is 10^3 to 10^4 times smaller than crystalline silicon [10, 187]. The large optical absorption reduces the amount of material required for photovoltaic devices. Combined with the low material extraction costs and processing costs, in part determined by high material abundance, development of iron pyrite photovoltaic cells may contribute to global power production at the terawatt scale [188].

Despite iron pyrite's favorable photovoltaic properties and several decades of experimental and theoretical effort, development of iron pyrite remains incomplete [10, 135, 187, 146, 143]. Some progress towards photovoltaic devices has been made with reports of thin film Schottky cells with Au, Pt, and Nb contacts [189, 187], photoelectrochemical cells [190, 146, 133, 191, 192, 193, 194, 154] and nanocrystal pyrite inorganic-organic hybrid devices[195]. However, power conversion efficiencies remain low with $\mu_{PV} < 0.2\%$ for hybrid cells [195] and $\mu_{PV} < 6\%$ for photoelectrochemical cells [190]. A low open-circuit photovoltage ($V_{OC} < 200\mathrm{mV}$) in single-crystalline material is one of the main challenges towards improving efficiencies [190, 189, 196, 187]. Several mechanisms for the low V_{OC} have been proposed and explored in the literature, including bulk non-stoichiometry via vacancies or impurities [197, 190, 198, 199, 200, 189, 187, 201, 202, 203], Fermi level pinning from surface states [198, 204, 199, 205, 187], and phase impurities (such as marcasite or amorphous iron sulfide) [197, 196, 206, 202, 188, 143], but a consensus for the cause of low V_{OC} has not been reached. Improving device performance will require more complete understanding and control over growth mechanisms, microstructure, surface chemistry, doping and electronic properties, and passivation[10, 187].

Thus far, reliable production of phase-pure iron pyrite thin films with controlled material properties remains difficult, limiting photovoltaic device development [10, 131]. Recent work has focused on fabrication of iron pyrite thin films using techniques including solvothermal synthesis [132], metal-organic chemical vapor deposition [133, 134], chemical vapor deposition [135,

136], spray pyrolysis [137, 138, 139, 140], nanoparticle synthesis [141, 25], sputtering [142, 143], sol-gel [144], chemical vapor transport [145, 146, 147], and sulfurization of iron and iron oxide precursors films [148, 149, 150, 151, 152, 142, 153, 154, 155, 156].

Sulfurization is attractive for its simplicity and therefore potentially low processing costs. Typically, bulk Fe precursor films are used, where the microstructure, optical and electrical properties of the iron pyrite are primarily controlled through the sulfurization conditions (e.g., temperature, pressure, duration)[157, 207, 208, 209, 153, 210, 211]. Although some studies have explored the effect of the precursor's structure, such as Fe film thickness and grain size [150, 212], the full potential of this technique remains uncultivated.

Conversion of Fe to FeS_2 occurs through an intermediate phase of FeS [157]. Insufficient diffusion through the intermediate FeS layer can lead to incomplete conversion in thicker films. However, this issue is mitigated for photovoltaic applications where only thin layers 100 nm are required. An issue that does persist at these thicknesses is potential stress failure of the iron pyrite film, such as buckling or cracking [157, 158, 159, 150]. During phase transformation unconstrained material will expand due to the density difference between iron ($\rho_m = 7.87\ \mathrm{g \cdot cm^{-3}}$) and iron pyrite ($\rho_m = 4.89\ \mathrm{g \cdot cm^{-3}}$). Attempts to alleviate stress failures include the addition of adhesion layers[142] and limited attempts to introduce porosity into Fe precursor by depositing onto heated substrates [150].

In this chapter we mature the idea that precursor structure can be used to influence the iron pyrite microstructure. In the previous chapter, we used flux engineering to develop precursors with a columnar morphology and tunable spacing. This allows sulfur vapor to penetrate the depth of the film to assist sulfurization [157], and proper spacing of the columns eliminates stress-failures by incorporating voids into the film. The angle of incidence of the flux, known as the deposition angle (α), controls the column spacing (void fraction) of the precursor films. A schematic of the deposition and sulfurization process is shown in Figure 4.1. Here, we show that stress failure can be eliminated with precursors deposited at $\alpha > 80°$. Morphology and crystal structure of the iron pyrite films can be tuned to achieve uniform films composed of large grains/crystallites desirable for photovoltaic application.

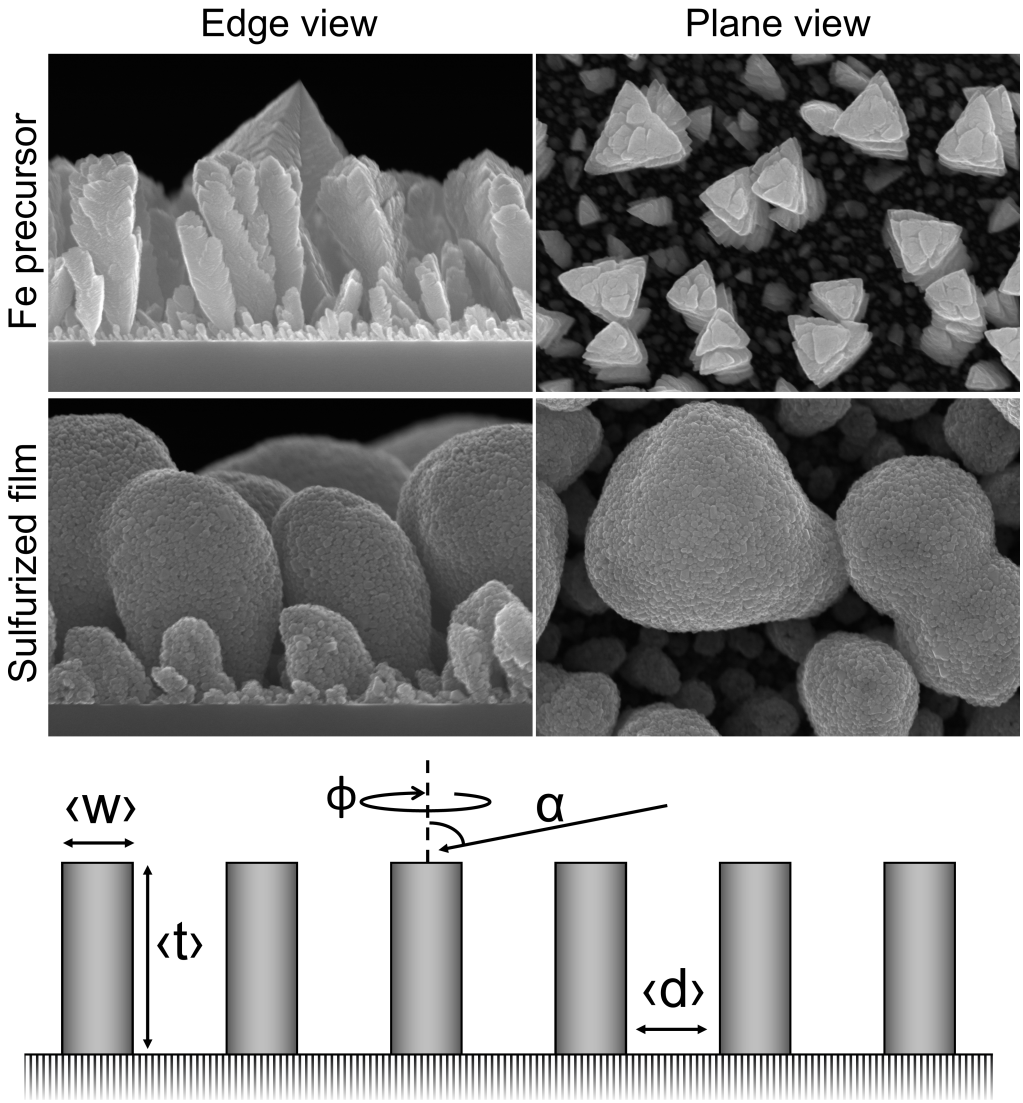

Figure 4.1: Electron micrographs of a Fe precursor deposited at $\alpha = 88°$ and $t_{Fe} = 936$nm (1000 nm nominal) and the resulting sulfurized film. A schematic of the deposition geometry is provided to illustrate the deposition angle (α) and rotation angle (ϕ). Changing the deposition angle (α) affects the inter-column spacing (d), so that $\langle d \rangle$ tends to increase with α and thereby increase the void fraction of the film. Column parameters are bracketed in the schematic, to indicate that these parameters are statistical averages over the film.

We consistently used a sulfurization recipe taken from an examination of the literature [157, 207, 208, 209, 213, 210, 211] and have not attempted to demonstrate improvements on sulfurized iron pyrite through the sulfurization chemistry. Instead, we establish that precursor structure, primarily void fraction, presents an additional mechanism to control iron pyrite microstructure that can potential supplement changes in the sulfurization recipe. Finally, we have characterized the optical and electrical properties, including optical-pump/THz-probe measurements of carrier recombination times, of the films with the largest grains (produced at $\alpha = 82°$) to gauge their suitability for device applications and contrast them with other sulfurized iron pyrite thin films.

4.2 Experimental details

4.2.1 Iron precursor film deposition

The iron precursor films were deposited using a similar recipe established in Chapter 3. Briefly, the iron precursor films were deposited with a custom, high-vacuum, electron-beam evaporation system (Kurt J. Lesker AXXIS) onto unheated Si substrates (100, p-type, test-grade, $\rho < 100\,\Omega \cdot \mathrm{cm}$, University Wafer) and fused quartz after reaching a chamber pressure of $p < 0.1$ mPa, which was maintained during deposition. Substrates were cleaned by ultra-sonication in de-ionized water, followed by rinses in acetone and isopropanol. The substrate chuck was placed 42 cm from the crucible. Elemental iron (cylindrical pieces 3 mm to 6 mm in length, 99.95% purity, Kurt J. Lesker) source material was held in a graphite crucible. An electron beam with sweep pattern size of 1.5 cm in diameter melted the source material. Nominal flux rate was monitored with a quartz crystal thickness monitor (Maxtex SC-105) and maintained at $(0.1 \pm 0.01)\,\mathrm{nm \cdot s^{-1}}$ by adjusting the beam current periodically throughout the deposition. The vapour flux incidence angle (α) was held at a constant value for each deposition, but the azimuth (ϕ) was continuously increased (constant rotation). Deposition pitch was held constant at a value of 1 nm for each deposition to achieve the well-formed tetrahedral columns discussed previously in Chapter 3.

4.2.2 Iron film sulfurization

After deposition, the iron films were sulfurized [i] to produce iron pyrite (FeS_2) in sealed quartz ampoules at 450 ℃ (Figure 4.2). The quartz ampoules (inner diameter 25 mm) were prepared by cleaning in de-ionized water under sonication, followed by rinses in acetone, isopropanol and ultra-pure water. Ampoules are then placed in a glass oven held at 110 ℃ and left overnight. Sulfur powder was placed in the ampoules (Alfa Aesar, 99.9995 %, CAS No. 7704-34-9) with Fe precursor films. The amount of sulfur powder was adjusted to the ampoule volume, so that a partial pressure of $S_{8(g)}$ would reach 80 kPa at 450 ℃. Typically, 200 mg to 250 mg of powder were added to meet this requirement. Afterwards the ampoules were pumped down with a glass diffusion pump for >1 hour before sealing under vacuum. Sealed ampoules were placed in a tube furnace (Lindburg Blue M, one zone) at room temperature and ramped to 450 ℃ in 45 minutes, and then held at 450 ℃ for 10 hours before passively cooling back down to room temperature.

Figure 4.2: Photograph of a fused quartz ampoule with a Si substrate and iron pyrite thin film after sulfurization.

4.2.3 Characterization

Morphological characterization of both iron precursors and sulfurized films was performed with SEM (Hitachi S4800). Select sulfurized samples were

[i] The American spelling of "sulfurization "is used here to be consistent with the majority of the scientific literature.

also examined with TEM (JEOL 2200 FS and Hitachi H9500) and EDX (Hitachi S5500) under STEM-HAADF (atomic number contrast). TEM and EDX samples were prepared by focused ion beam (FIB) to create 30 nm thick lamellas and by mechanically removing film material from their substrate and placing the powder on TEM grids.

A ToF-SIMS IV instrument (ION-TOF GmbH) produced composition depth profiles via time-of-flight secondary ion mass spectroscopy (ToF-SIMS) with a 200 μm $\times$ 200 μm sputter etch area and a centred 40 μm $\times$ 40 μm analysis area. X-ray diffraction profiles were acquired with a Bruker D8 Discover, with a Cu Kα, 0.5 mm collimator, and HiStar area detector positioned at a distance of 15 cm. Iron fluorescence is produced by the Cu Kα radiation and was compensated for by increasing the acquisition time per frame.

Crystallite size was calculated by fitting the (200) peak at $2\theta = 33°$ with a pseudo-Voigt profile [170]. The instrumental function was estimated by fitting the (110) peak at $2\theta = 30.4°$ of the NIST SRM 660b (lanthanum hexaboride, LaB_6) to a pseudo-Voigt profile. Diffraction data for LaB_6 was taken on several days, and collected under the same conditions as the film diffraction data. The Cauchy contribution of the integral breadth, which is due to crystallite size-broadening, was calculated for both the films and LaB_6 powder reference [214]. The instrumental resolution was estimated by averaging the integral breadth from six fits and taking the mean for the integral width limit. The crystallite size instrumental limit was taken to be the crystallite size calculated for an integral breadth that is three standard deviations from the mean LaB_6 integral breadth. After subtracting the instrumental contribution to the (200) integral breadth, the crystallite size was calculated with the Scherrer equation assuming monodisperse, cubic crystallites. Further explanation and summary of size-broadening analysis from diffraction line profiles is summarized elsewhere [170].

Reflection and transmission spectra of the films on fused quartz substrates were acquired with a variable angle spectroscopic ellipsometer (V-VASE, J.A. Woollam Col. Inc). Absorption spectra were calculated using a simple single-reflection model described by Equation 4.1.

$$\alpha_o = -\frac{1}{t} ln \frac{T_o}{1 - R_o} \tag{4.1}$$

where t is the film thickness, and T_o and R_o are the reflection and transmission values. Room temperature Hall measurements were taken with HL5500PC Hall Effect Measurement System (Accent) with pressed indium contacts.

By collaborating with Dr. Hegmann's group in the Department of Physics we were able to obtain measure the ultrafast photoconductivity by optical-pump/THz-probe measurements at room temperature. The experimental technique is illustrated schematically in the inset for Figure 4.15 and a schematic of the optical setup is provided in Appendix C. The sample is excited with an ultrafast optical pump pulse (800 nm, 100 fs) which generates charge carriers in the film. The resulting transient photoconductivity is then probed by monitoring the negative differential transmission, $-\Delta T_o/T_o$, of the main peak of the THz pulse with respect to pump-probe time delay. In the limit of small transmission modulation, $-\Delta T_o/T_o$ is proportional to the time-dependent photoinduced conductivity of the sample. Optical-pump/THz-probe measurements allow probing of transient photoexcited carrier dynamics and photoconductivity over picoseconds time scales in a contact-free fashion, and have been successfully applied for exploring ultrafast carrier dynamics and the nature of conduction in a variety of materials[215], including nanogranular[216] and nanocrystalline[217] materials.

4.3 Results

4.3.1 Microstructural survey with α

Porous iron GLAD films were deposited with a range of void fractions by adjusting the deposition angle (α) from 30° to 88° on Si and fused quartz substrates. A schematic in Figure 4.1 clarifies the relationship between α and Fe film morphology. Post deposition the films were sulfurized in a sealed quartz ampoule with 80 kPa of sulfur at 450 ℃ for 10 hours. An example of a Fe film before and after sulfurization is shown in Figure 4.1. In this case (α = 88°), the columnar structure of the Fe film is clearly seen and

this structure is reflected after sulfurization. Inter-column spacing of the precursors decreases with α. At the lowest values studied ($\alpha = 30°$) the films are bulk-like, but have a surface microstructure consistent with a high-density of grain boundaries as shown in Figure 4.3. Voids and grain boundaries assist sulfurization by increasing sulfur vapor transport into the film [157]. We have examined films across a range of deposition angles (enumerated in Table 4.1) to examine microstructural changes and determine the conditions that produce films most suitable for photovoltaics (e.g., uniform and large-grained).

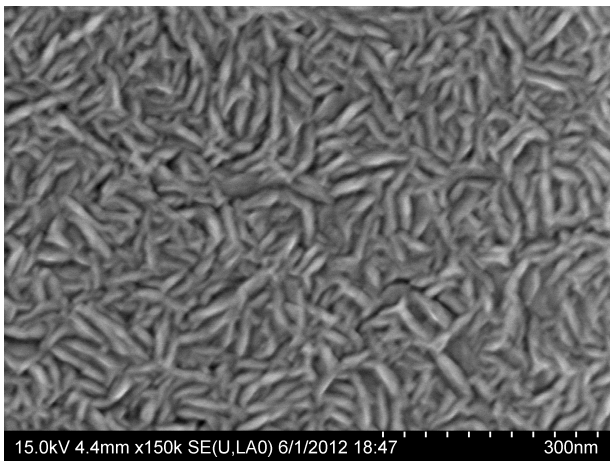

Figure 4.3: Plan-view SEM image of a Fe precursor film ($\alpha = 30°$, 200 nm nominal).

Our iron pyrite films consist of equiaxed grains, where the grain size and their spatial distribution depend on the void fraction of the Fe precursor, controlled by α, as shown in Figure 4.4. Three regions are observed across the range of α studied: cracked and/or buckled planar films $\alpha < 81°$, uniform planar films $81° \leq \alpha \leq 83°$, nanostructured films $\alpha \geq 84°$. Films sulfurized at $\alpha < 81°$ produce small grains similar to those seen in Figure 4.4a. At the opposite end, $\alpha \geq 84°$, the films are composed of small grains grouped into larger surface structures Figure 4.4c,d). Surface grooves appear at $\alpha = 84°$, but it is not clear if the grooves extend to the base in the film from the cleaved-cross section images in Figure 4.4c. As α increases further, the film consists of nanopillars ≈ 100 nm in diameter, which themselves appear to be comprised

Table 4.1: Sample legend for the sulfurized iron pyrite films produced from columnar Fe GLAD precursors. The sulfurized film thickness (t_{FeS_2}), Fe precursor deposition angle (α_{Fe}), Fe precursor thickness (t_{Fe}).

α_{Fe} (°)	Nominal t_{Fe} (nm)	Measured t_{Fe} (nm)	σt_{Fe} (nm)	t_{FeS_2} (nm)	σt_{FeS_2} (nm)
30	200	187	9	312	18
50	200	179	9	502	36
70	200	167	9	442	23
80	200	194	10	333	17
81	200	217	14	330	17
82	200	192	11	359	21
83	200	206	11	311	16
84	200	220	11	335	18
86	200	174	9	284	15
88	200	132	7	222	12
82	100	88	4	182	13
82	200	197	11	329	17
82	300	296	15	502	30
82	500	492	25	786	43
88	1000	936	72	1371	82

of smaller grains $\approx$ 10 nm in size (Figure 4.4d). In between these two regions, at $81° \leq \alpha \leq 84°$, bulk-like, poly-crystalline films with large faceted grains $\approx$ 100 nm in size are produced (Figure 4.4b). This microstructure appears well-suited for electronic devices, due the large crystallites that may facilitate long-carrier lifetimes if the iron pyrite can be made defect-free. Plan-view SEM images indicate that voids are present in the film at $\alpha = 82°$ and direct confirmation of these voids was made by imaging a film lamella with a transmission electron microscope (Figure 4.5) We have not attempted to remove the voids through changes in sulfurization conditions of precursor morphology. A voided microstructure may be a necessary trade-off to achieve larger grain growth.

Fitting of the (200) x-ray diffraction peak with a pseudo-Voigt profile was used to calculate crystallite size as a comparison to the grain size observed in the electron micrographs [170]. In general, these two measures do not correspond to the same physical entity. Their difference has been previously highlighted by Ares et al.[159] where they showed that grains imaged with atomic force microscopy (AFM) were consistently larger than the crystallite size measured with XRD. Our crystallite size measurements are shown in Figure 4.6. The crystallite size begins at 70 ± 16 nm ($\alpha = 30°$) and trends towards smaller values as α increases and finally reaches a value of 30 ± 9 nm at $\alpha = 88°$. However, in the range between $81° \leq \alpha \leq 84°$, the crystallite size increases suddenly, diverges from the overall trend and increases to values >100 nm. Note that the lower bound error bars for a few points with crystallites above 100 nm extend to negative values and thus have been omitted from the semi-log plot. These large crystallites approach the instrumental limit of the x-ray diffractometer that is defined by the minimum integral breadth measurable, and thus cannot be quantified precisely. To illustrate this point, the measured integral widths are also shown in Figure 4.6b and the data demonstrate the sudden decrease to the instrumental limit for films in the range $81° \leq \alpha \leq 84°$. Confirmation of this effect was made by repeated sample fabrication and repeated measurements near $\alpha = 82°$. The Scherrer formula calculates the ratio of the 4th and 3rd moments of the crystallite size distribution ($D = \langle D^4 \rangle / \langle D^3 \rangle$); it is not a measure of the average crystallite size or first-moment of the crystallite distribution [170]. Overall,

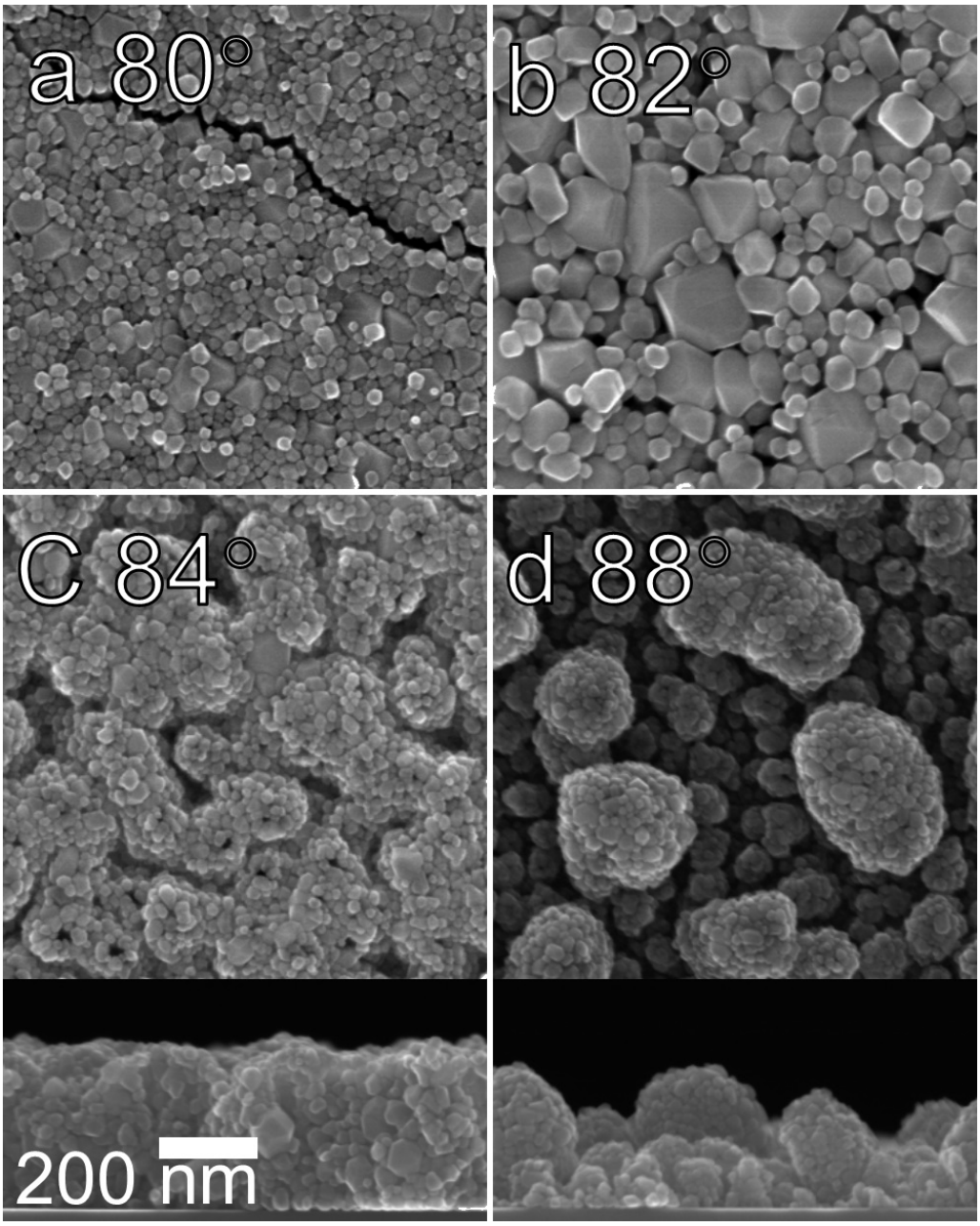

Figure 4.4: Morphology of sulfurized films from Fe precursor films deposited at a) 80°, b) 82°, c) 84°, and d) 88°. Imaging of cleaved-cross sections for samples c) and d) are shown at the bottom and demonstrate the transition to a porous structure at large deposition angles.

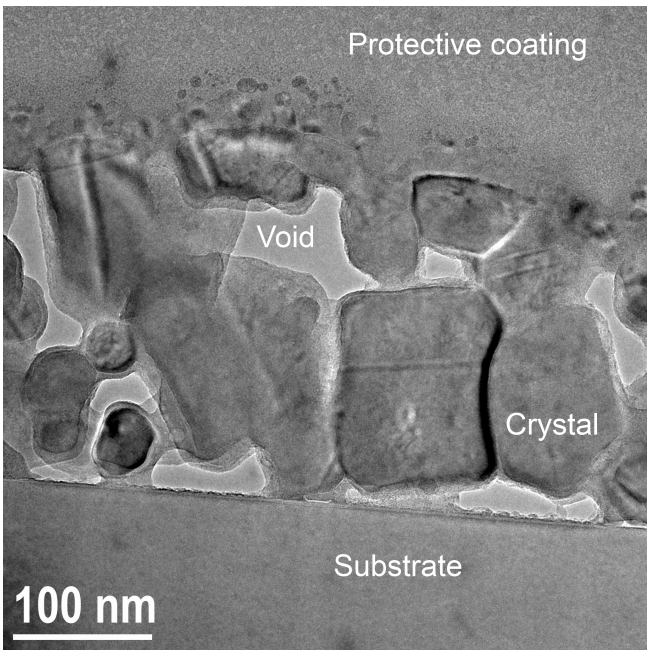

Figure 4.5: TEM survey image of the lamella taken from the sulfurized film (precursor, $\alpha = 82°$, 200 nm). Large crystallites mixed with voids can clearly be seen.

changes in the crystallite size observed by electron microscopy (Figure 4.4, Figure 4.5) agree with the trends seen in x-ray diffraction data (Figure 4.6) and provide a complimentary picture of the effect void-fraction has on iron pyrite microstructure.

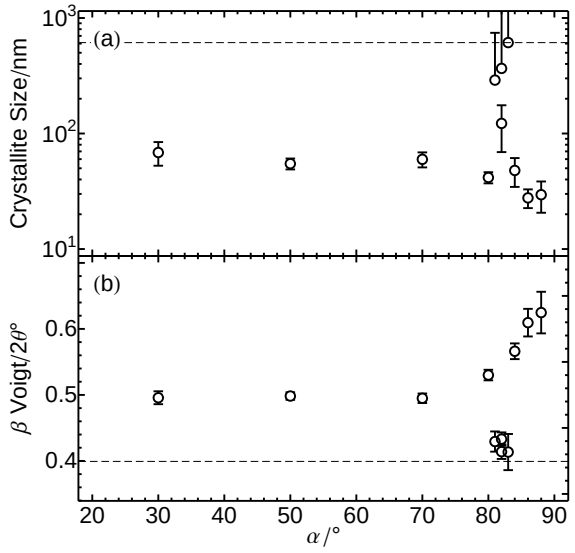

Figure 4.6: Crystallite size a) calculated from the (200) diffraction peak decreases with deposition angle (α), except for the region around $\alpha = 82°$, where the crystallite sizes approach the instrumental limit (dashed lines). Negative error bars for three measurements in a) are omitted on the log-scale, but extend below the x-axis. The integral breadths of the peaks are shown in b) for comparison, where the decrease to the instrumental limit is more apparent.

While grains >100 nm have been observed in other sulfurization work, crystallite sizes measured by XRD have remained at $\approx$ 100 nm even under conditions of hotter sulfurization temperature, or longer processing times [218, 219, 159]. Control over precursor void fraction provides another mechanism, in addition to the sulfurization chemistry to optimize the microstructure of iron pyrite for devices. Further improvements in crystal growth may be expected by combining void-fraction with improved sulfurization conditions (e.g., hotter temperatures). Control over crystal growth and crystallite size

is an important parameter in photovoltaic materials. For example, grain boundaries can affect electronic properties such as photocarrier lifetimes and mobility. Thus, void fraction engineering may be an important technique for producing photovoltaic-grade iron pyrite films.

4.3.2 Stress-related failure changes with α

In conjunction with the changes in morphology and microstructure, stress failures were observed for iron pyrite sulfurized from films deposited below $\alpha \leq 80°$. Buckling occurs at $\alpha = 30°$ and was initiated during cleaving for $\alpha = 50°$ (Figure 4.7). Residual stress also contributes to poor adhesion to the Si substrates, with both the 30° and 50° films delaminating partially during a Scotch tape test. In comparison, films $\geq 70°$ are robust enough to stay completely adhered. However, cracking similar to that in Figure 4.4a, is present at $\alpha = 70°$ and 80°. The compressive and tensile stresses that lead to cracking, buckling and poor adhesion can be attributed to the volume expansion during phase transformation and substrate-film thermal expansion mismatch. The linear thermal expansion coefficients at 300 K for both substrates, Si and fused quartz ($2.6\times10^{-6}\mathrm{K}^{-1}$ and $0.59\times10^{-6}\mathrm{K}^{-1}$)[220], are smaller than that of iron pyrite ($4.5 \times 10^{-6}\ \mathrm{K}^{-1}$)[147]. This mismatch is expected to contribute to tensile stress, and hence cracking, as the sulfurized material cools from the reaction temperature (450 ℃) to room temperature. During sulfurization, the precursor Fe films undergo a volume expansion of approximately 3.5 times due to the density difference between iron ($\rho_{m_{Fe}} = 7.87\ \mathrm{g \cdot cm^{-3}}$) and iron pyrite ($\rho_{m_{FeS_2}} = 4.89\ \mathrm{g \cdot cm^{-3}}$), which contributes to compressive stress. When laterally constrained by the substrate (i.e., no buckling) films are only free to expand along the substrate normal.

We can reduce the lateral constraint on volume expansion by increasing the void fraction of the precursor films through α as shown in Figure 4.8. The low value of normal expansion at $\alpha = 30°$ is attributed to the spontaneous buckling that occurs there, which removes the lateral constraint of the substrate/film interface. For $\alpha = 50°$ and 70° where spontaneous buckling is absent, lateral constraint by the substrate forces the thickness expansion to increase to values between 2.5 to 3.0. When $\alpha > 80°$ the increased void

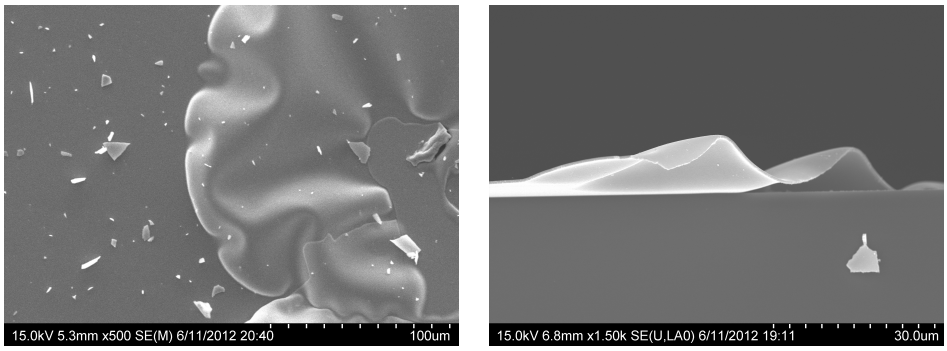

(a) (b)

Figure 4.7: Examples of buckling seen in (a) $\alpha = 30°$ and (b) $\alpha = 50°$ films after sulfurization.

fraction allows for lateral expansion and the normal expansion decreases to the unconstrained value of $3.5^{1/3} \approx 1.51$ as expected.

Reduced stress during recrystallization can lead to larger crystallite sizes [221], which may offer an explanation for the sudden increase in crystallite size seen in Figure 4.4 and Figure 4.6. In this region, the void fraction reduces stresses which result in the recrystallization process producing larger grains/crystallites. The smaller crystallites seen as isolated structures form at $\alpha > 84°$ suggests that long-range diffusion processes are important for producing large-crystallites. However, the precise role that voids play in the dynamic recrystallization process during sulfurization will require additional studies.

Above $\alpha = 80°$, sufficient void-fraction exists in 200 nm (nominal t_{Fe}) precursor films to prevent stress-related failures that would be detrimental to their application in devices. At $\alpha = 88°$, the columnar structure of the sulfurized films in Figure 4.4d (nominal $t_{Fe} = 200$ nm) is maintained in sulfurization of Fe precursors with a nominal thickness of 1000 nm (Figure 4.1). However, a thickness survey of $\alpha = 82°$ films in Figure 4.9, shows that the large-grained films begin to crack at a precursor thickness of 300 nm. This suggests that void fraction must be tuned in accordance with the precursor thickness to avoid cracking after sulfurization. Columnar GLAD films, like the Fe precursors, exhibit column broadening during growth [92, 84, 222].

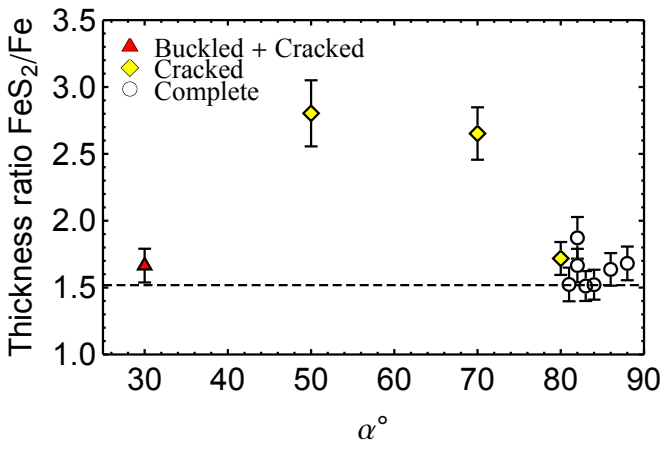

Figure 4.8: Thickness ratio between the sulfurized and precursor Fe film plotted against the deposition angle (α). Points are marked by the cracking behaviour observed in the films. At large deposition angles the void fraction of the precursor increases and the films approach the value for unconstrained expansion marked by the dashed horizontal line.

Reducing column broadening in the precursors, for example by increasing rotation rates during deposition, may also help suppress crack formation in thicker iron pyrite films.

4.3.3 Detailed characterization at $\alpha = 82°$

Iron pyrite films sulfurized from 200 nm thick precursors deposited at $\alpha = 82°$ are crack-free, uniform with large grains/crystallites. These films are sufficiently thick for strong absorption of sunlight, and the large crystallites may help improve carrier transport and lifetime. As these characteristics are appealing for photovoltaics we have further examined films prepared at these conditions to determine their phase purity, composition, and optoelectronic properties.

Composition and crystal phase

X-ray diffraction patterns demonstrate that the sulfurized films have a single crystal phase. A typical pattern for an iron pyrite film (precursor, $\alpha = 82°$,

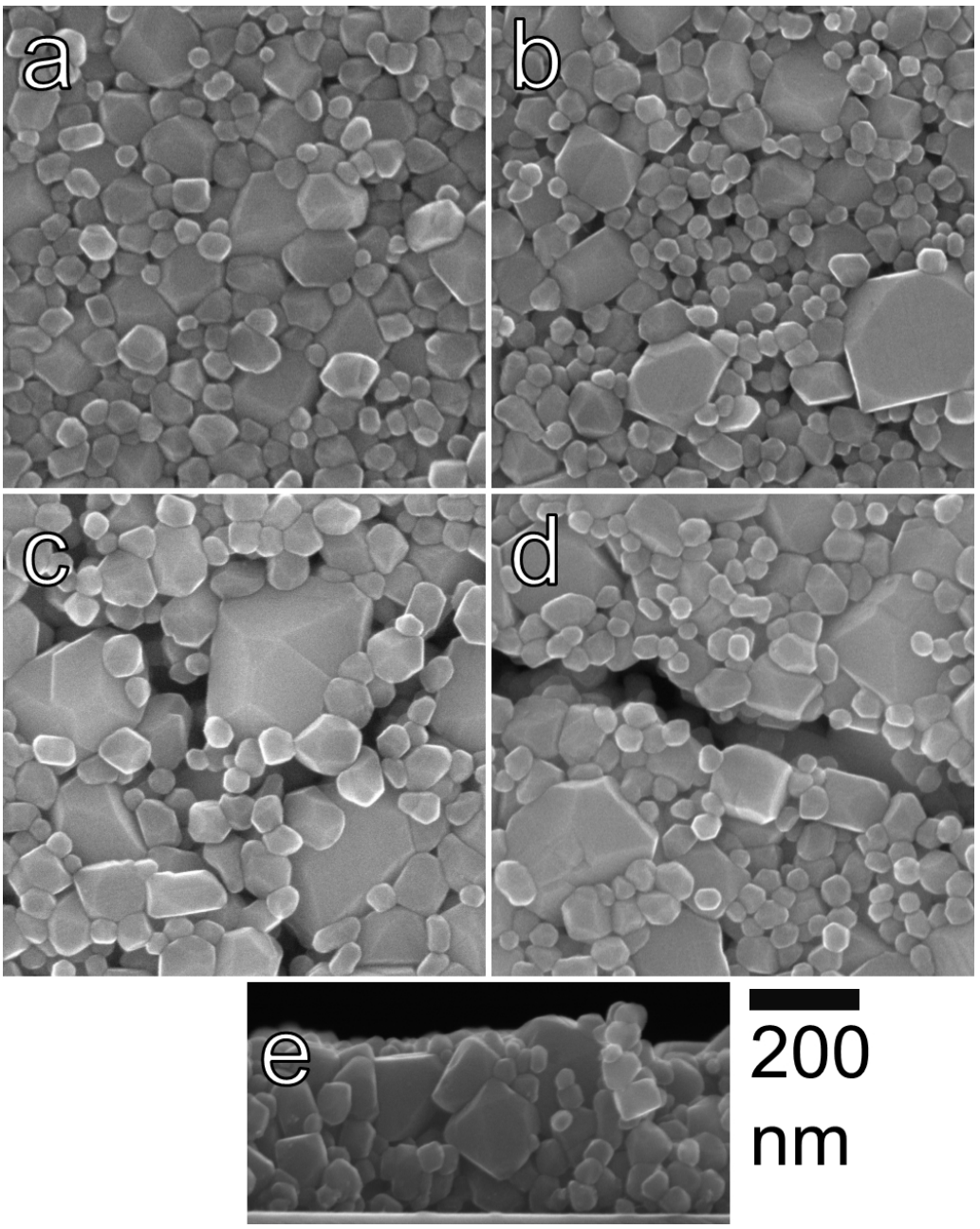

Figure 4.9: Plan-view images of sulfurized films from $\alpha = 82°$ precursors at nominal thicknesses of 100 nm a), 200 nm b), 300 nm c) and 500 nm d). A cross-section image of the film at 200 nm is included in e).

$t_{Fe} = 200$ nm) is shown in Figure 4.10a. There is no indication of a marcasite phase, a common impurity, in the diffraction profile, or in the diffraction profiles for the other films studied. Diffraction patterns for all the samples are presented in Figure 4.11.

We used transmission electron microscopy and electron diffraction on mechanically removed film material and lamellas (≈ 30 nm thick) to characterize the crystallinity and internal film structure. A high-resolution image of a crystallite is shown in Figure 4.10f. Measurements of the lattice spacing from this image and others produce a value of 0.54 ± 0.03 nm in agreement with the expected value of 0.5428 nm. Electron diffraction patterns, such as that shown in Figure 4.10h, further confirm the crystallinity of the material. Several of the crystallites show the development of right-angled surfaces that suggest {100} surfaces on the crystallite faces, but the faceting is often imperfect as seen in the Figure 4.10g. Changes in the sulfurization conditions may help improve consistency in crystallite shape.

Large crystallites, exceeding 100 nm in diameter can be seen in Figure 4.10g, corroborating the evidence for large crystallites in the previous SEM (Figure 4.4) and XRD diffraction data (Figure 4.11).

Composition was investigated with depth profiles taken with ToF-SIMS (Figure 4.10b) and energy dispersive x-ray spectroscopy (Figure 4.10c-e). Both techniques reveal the presence of oxygen within the film. Crystalline phases with an oxygen component were not observed in the XRD line profiles, thus the oxygen may be present on the surface[223] and/or as a substitutional defect [201, 202]. Presently it is unclear if the presence of substitutional oxygen is detrimental to the performance of iron pyrite in photovoltaic applications [201, 202]. Other samples at $\alpha = 30°, 50°, 70°, 80°,$ and $88°$ also show similar oxygen components (see Figure 4.12). In collaboration with Brian Worfolk of Dr. Jillian Buriak's group in Chemistry, we have begun to explore surface oxidation of similar iron pyrite films ($\alpha = 88°$) with ultra-violet and x-ray photoelectron spectroscopy (not shown). Initial results suggest that after exposure to atmosphere, oxidation of the surface progresses over the span of days to weeks. Thus, it is likely that at least some of the observed oxygen is due to surface oxidation. Oxygen contamination, potentially located at the surface and/or grain boundaries, has been observed by other

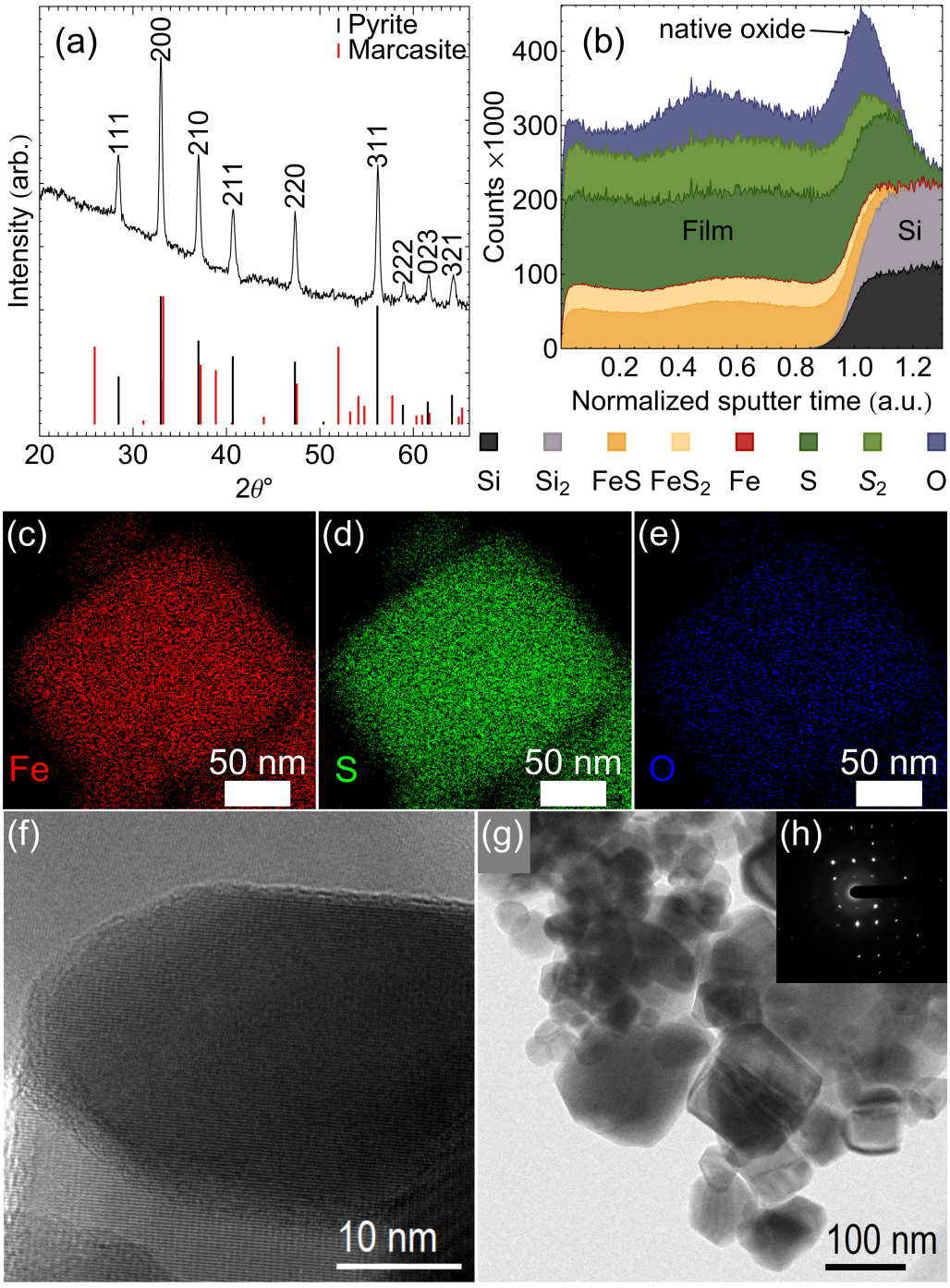

Figure 4.10: Characterization of a sulfurized film from an $\alpha = 82°$ and 200 nm nominal thickness Fe precursor. a) XRD diffraction profile for the sample along with powder diffraction profiles for the pyrite (ICDD 01-071-0053), and marcasite (ICDD 01-075-6904) phases shown for comparison. b) A composition depth profile of the film acquired with ToF-SIMS shows the continuous presence of oxygen throughout the film depth. Spatial composition maps for c) Fe, d) S, and e) O taken by EDX also indicate the presence of oxygen. TEM images of a film scraped off of the substrate to form a powder are shown in f) and g) along with an electron diffraction pattern shown in h).

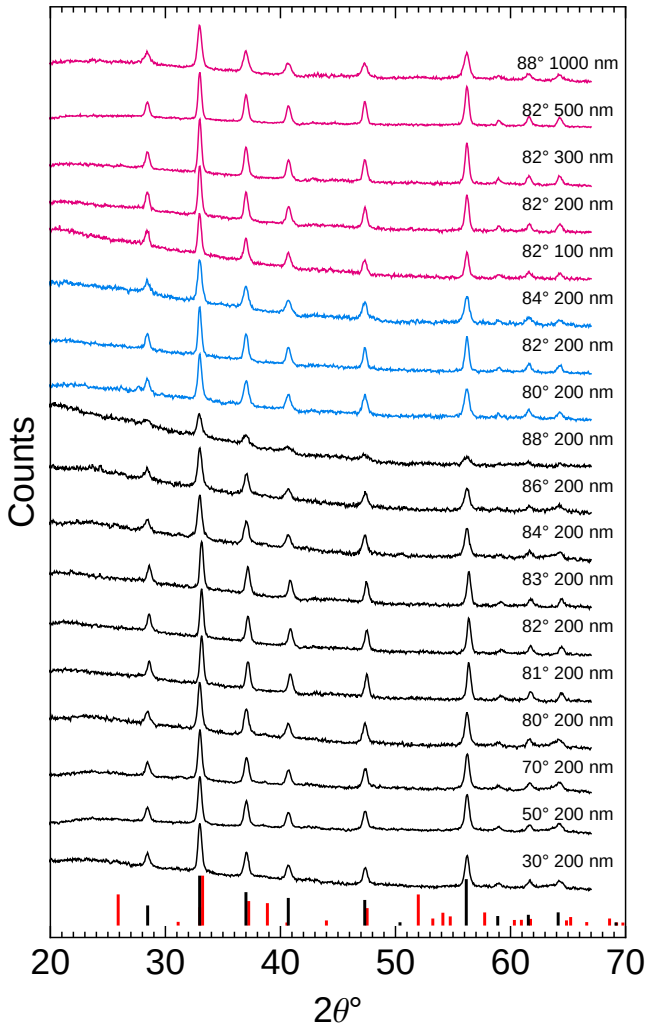

Figure 4.11: X-ray diffraction profiles for all samples studied. The samples are broken up into three groups by color. The black profiles are from sulfurized precursor films at a variety of deposition angles, but with a constant nominal thickness of 200 nm. The blue profiles are from repeated measurements. Magenta profiles are from a sulfurized precursors of varying thickness. Data for the 82°, 200 nm point from the black and magenta series was taken from different films. The powder diffraction patterns for pyrite (Black, ICDD 01-071-0053) and marcasite (Red,ICDD 01-075-6904) are shown at the bottom of the plot for comparison.

groups[135, 157] emphasizing the need for surface passivation [187]. Addressing these deficiencies experimentally, if possible, will likely require improvement in the sulfurization process and careful treatment of the samples to avoid oxidation before characterization.

4.3.4 Optical and electronic properties

Optical absorption was measured for iron pyrite sulfurized from $\alpha = 82°$ precursor with nominal Fe thicknesses of 100 nm, 200 nm, 300 nm, and 500 nm. Absorption spectra and a Tauc plot for these films are shown in Figure 4.13 where the data has been linearized according to Equation 4.2 [224, 225, 135].

$$(\alpha_o h\nu)^n = B(h\nu - E_o) \tag{4.2}$$

where $n = 1/2$ and $E_o \sim E_g$. Using this method, the band-gap of the film at $\alpha = 82°$ estimated to be 0.98 ± 0.04 eV, with values for the other films between 0.94 eV to 0.98 eV, in agreement with the accepted value of 0.95 eV [10]. Reasonable values for the band-gap in the literature can deviate from the accepted value by $0.1 - 0.2$ eV depending on the quality of the material and the experimental methods used [225, 10, 135]. Future work, may investigate the behavior of the sub-band absorption as the system temperature is reduced as a sceondary confirmation of a lack of amorphous regions within the film.

A room temperature four-point probe was used to measure resistivity, with measured values between 2.2 $\Omega \cdot$cm and 7.6 $\Omega \cdot$cm for the films between 200 nm and 500 nm thick. We measured the Hall mobility and majority carrier concentration for sulfurized films at $\alpha = 82°$ and nominal Fe thickness of 200 nm, 300 nm, and 500 nm. The measured carrier mobility was on the order of 0.1 $\mathrm{cm}^2 \cdot \mathrm{V}^{-1} \cdot \mathrm{s}^{-1}$ with majority carrier concentrations between $10^{18}\,\mathrm{cm}^{-3}$ to $10^{19}\,\mathrm{cm}^{-3}$.

Both Altermatt et al.[10] and Ferrer et al.[11] have compiled data of the mobility and carrier concentration of pyrite from the literature. An

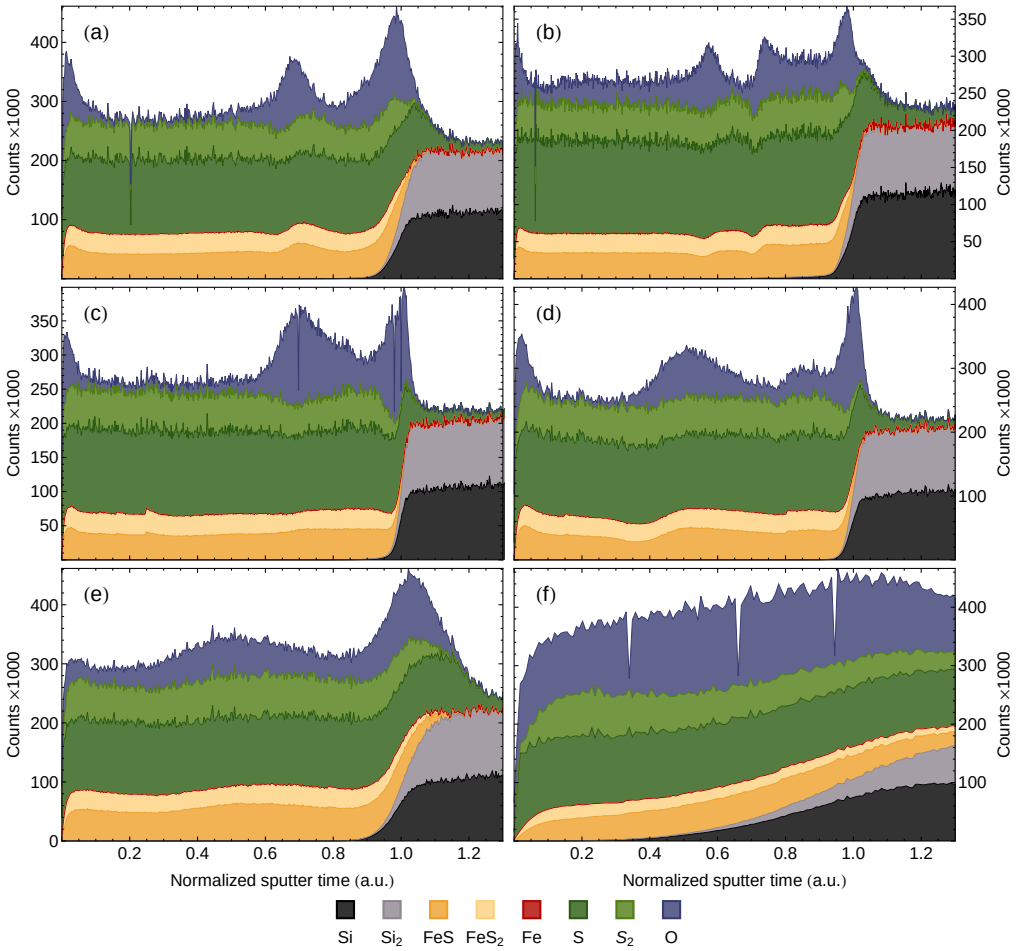

Figure 4.12: Time-of-flight secondary ion mass spectrometer (ToF-SIMS) composite depth profiles taken from sulfurized films of precursors with a nominal thickness of 200 nm and deposition angle (α) of a) 30°, b) 50°, c) 70°, d) 80°, e) 82° and f) 88°. The sputter time has been normalized to the film thickness (1.0), defined by the half-max point in the Si curve. Oxygen is present for all samples, and a peak in the oxygen signal occurs immediately before the substrate, which corresponds to the Si native oxide. At high porosity f) sputtering of the film and substrate appears to occur simultaneously, which causes the gradual change in composition.

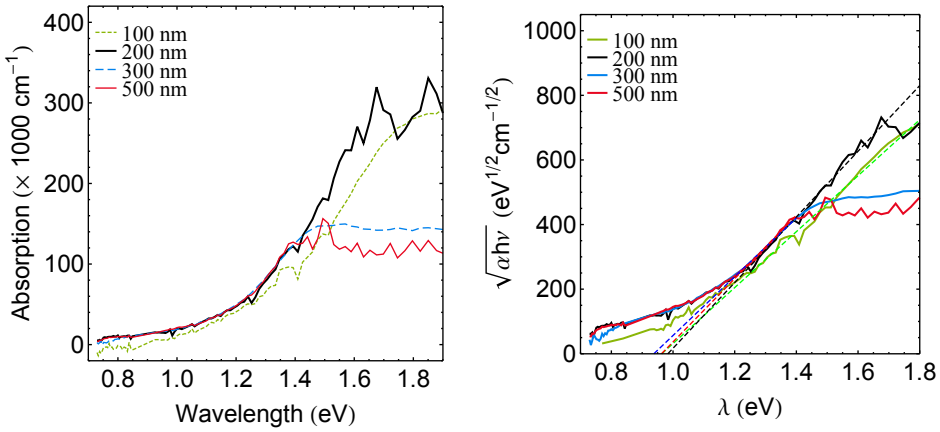

(a) (b)

Figure 4.13: (a) Absorption spectra and (b) Tauc plots of sulfurized samples from $\alpha = 82°$ precursors at all thicknesses studied. Noise at the higher photon energies is due to the transmission approaching the instrumental limit.

empirical relationship between the majority carrier mobility and majority carrier concentration has been used describe the trend in the data.

$$\mu = \mu_{min} + \frac{\mu_{max} - \mu_{min}}{1 + (n_{maj}/n_{ref})^{\beta}} \tag{4.3}$$

Parameter values used here and in the previous work were $\mu_{min} = 0.02\text{cm}^2 \cdot \text{V}^{-1} \cdot \text{s}^{-1}$, $\mu_{max} = 300\,\text{cm}^2 \cdot \text{V}^{-1} \cdot \text{s}^{-1}$, $n_{ref} = 6 \times 10^{17}\text{cm}^{-3}$ and $\beta = 1.3$, which were originally proposed by Dasbach[226] to describe how the room temperature carrier mobility is limited by phonon scattering and lattice defects. We have digitized the data in Figure 1 from Altermatt et al.[10] and included our own data from films sulfurized from precursors deposited at $\alpha = 82°$ and a nominal thickness of 200 nm, 300 nm and 500 nm on fused quartz substrates. The combined data set and model is presented in Figure 4.14. These values overlap well with the literature values summarized in reports by Altermatt et al.[10] and Ferrer et al.[11]. Important to this work, this suggests that the voids present in these films are not of sufficient density to disrupt continuous in-plane electrical pathways. We have not reported majority carrier type due to the known difficulties in reliably determining majority carrier type in iron

pyrite thin films with Hall measurements[11].

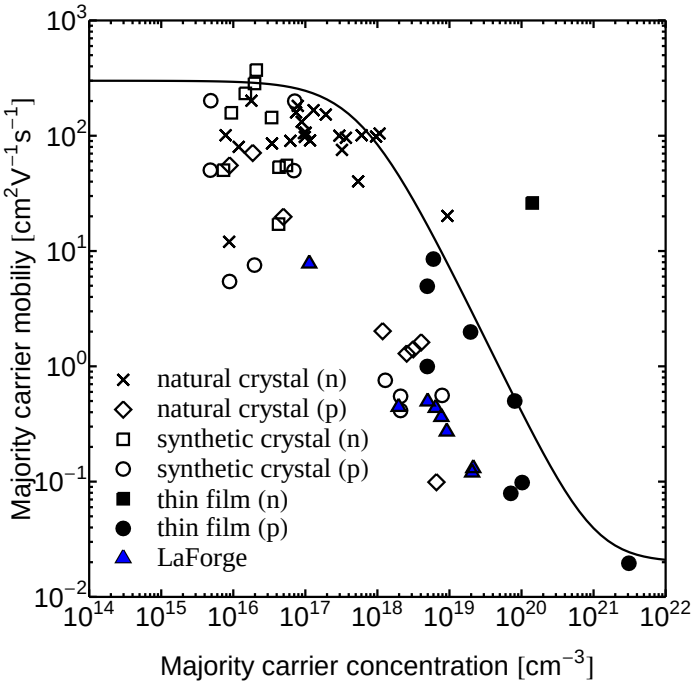

Figure 4.14: Majority carrier mobility versus majority carrier concentration for data taken from Altermatt et al.[10] and from sulfurized films measured in this work. The data includes some repeated measurements of the same film. The line is a empirical curve using parameters found in the literature [11, 10].

At present, the cause of the consistent electrical properties observed in iron pyrite films remains unresolved. Metallic sulfur-deficient phases[143], oxygen doping or point defects[135, 201, 227], and surface effects[135, 228] have all been proposed. Our work does not support the metallic sulfur-deficient phases as the cause. Unlike Yu et al.[143], we do not observe large amorphous regions that could indicate a sulfur-deficient phase. Spatial composition maps (Figure 4.10) also do not indicate sulfur deficient regions within the crystallite volume.

As the primary interest in iron pyrite is as an absorber material in photovoltaic cells, we have quantified the ultrafast photoconductivity of the mate-

rial with a room temperature optical-pump/THz-probe measurement shown in Figure 4.15. This work was pursued in collaboration with Dr. Hegmann's group in the physics department. We find that FeS_2 exhibits photoconductivity characteristic of semiconducting materials: the initial fast rise, followed by a fast decay over tens of picoseconds. The time evolution of photoconductivity can be fit by a bi-exponential decay with fast (4 ps) and slow (27 ps) components, indicative of at least two different carrier relaxation mechanisms such as carrier trapping at bulk defect and grain boundary trap states. These lifetimes are significantly shorter than previous studies, which have reported lifetimes (10 to 100) ns for pyrite films prepared by spray pyrolysis and sulfurization of iron oxides [154]. As lifetimes of at least 100 ns are required for good photovoltaic performance [10], further improvements in carrier lifetimes are required before application of these films to devices. Substitutional oxygen defects may act as Shockley-Read-Hall recombination centers, and therefore limit carrier lifetimes in these films [201, 227]. Reducing oxygen incorporation is an obvious area of improvement, and should be possible with changes to the sulfurization chemistry.

4.4 Conclusion

We have demonstrated that engineering the void fraction of Fe precursor films can be used to control the microstructure of iron pyrite thin films produced by annealing in a sulfur atmosphere. Precursor films have a columnar morphology, which assists the sulfurization processes by enhancing the diffusion into the film's bulk[157]. With sufficient void fraction ($\alpha > 80°$), stress-related failures (i.e., buckling or cracking) in the iron pyrite films can be eliminated. Furthermore, within a narrow range of void fraction seen around $\alpha = 82°$, the crystallite size of the iron pyrite peaked and was 4 to 5 times larger than for $\alpha \neq 82°$. Control over crystallite growth is important, as crystallite size influences carrier dynamics that are important for photovoltaic applications. For instance, large crystallites reduce grain boundaries and may assist in improving photocarrier lifetimes. Here, we have achieved some of the largest crystallites for sulfurized Fe films in the literature [208, 218, 159, 151]. Typical crystallite values for sulfurization at 450 ℃ are $D \approx 40$ nm, with values

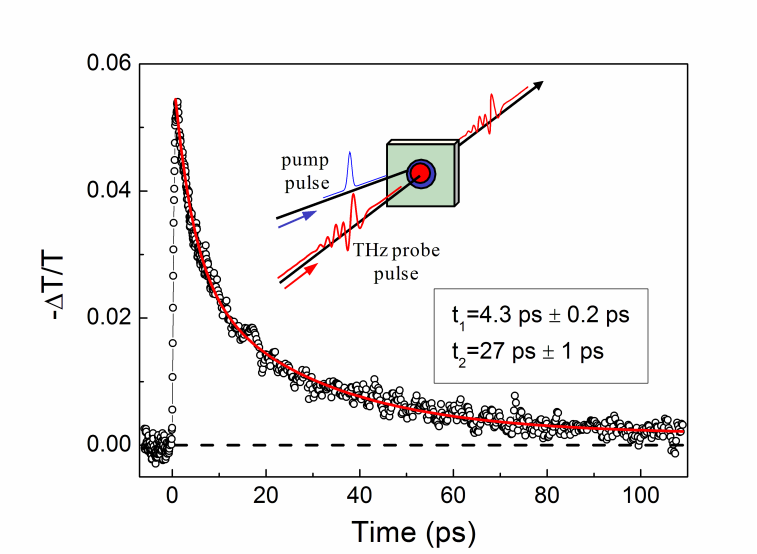

Figure 4.15: Transient photoconductivity from optical-pump/THz-probe measurements of a 200 nm (nominal) 82° sulfurized film on fused quartz after photoexcitation with 800 nm pulses at a pump fluence of 290 μJ cm^{-2}. The experimental data is represented by symbols (open circles), and the solid line is a fit to a biexponential decay. Fit parameters are given in the legend. Inset – schematic diagram of the optical-pump/THz-probe experiment.

< 90 nm at 500 ℃ [159]. Crystallite sizes > 100 nm can be produced by other methods [25, 229]. Thus, engineering the void fraction makes metallic-Fe sulfurization competitive with other fabrication techniques in this area. Our iron pyrite films have a single crystal phase and possess optical and electrical properties consistent with other thin films prepared elsewhere [10, 135, 11]. Despite the large crystallite sizes, carrier lifetime in these films is too short to produce high-performance photovoltaic devices. Careful tuning of the sulfur annealing conditions to reduce bulk defects, and a better understanding of interactions at the surface and grain boundaries, should help improve carrier dynamics.

Void fraction engineering provides a means to tune microstructure (i.e., crystallite size and morphology) that is independent of sulfur annealing conditions. Thus, the technique presented here compliments, and may enhance, existing and future sulfurization methods in the pursuit of high-quality, low-cost, iron pyrite thin films for photovoltaics. The next chapter will use similar sulfurized iron pyrite films and evaluate their feasibility as an inorganic absorber in a hybrid organic-inorganic photovoltaic device.

Chapter 5

Exploring pyrite hybrid inorganic-organic photovoltaic applications

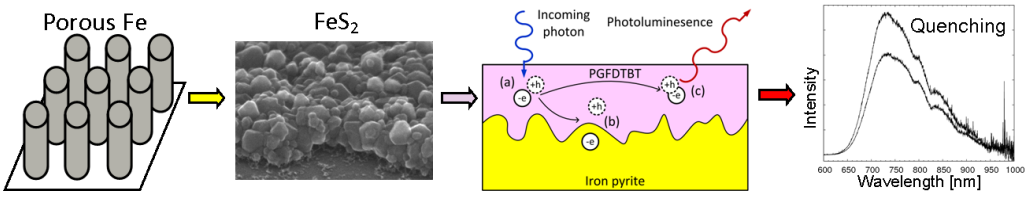

The previous chapter established that columnar Fe precursors can be used to tune the microstructure of iron pyrite produced by sulfurization. Here, we fabricated similar iron pyrite films and tested their feasibility in a hybrid inorganic-organic photovoltaic system with photoluminescence quenching measurements. Such measurements provide an indication of charge transfer between the conjugated polymer and pyrite material. We undertook the work in this chapter before that in Chapter 4, which helped define the scope of and design of that subsequent study.[i]

[i]The results of this chapter were presented at the MRS Spring 2012[230] conference and Next Generation Solar[231] meetings.

5.1 Introduction

A more complete introduction to iron pyrite was given in the preceding Chapter 4. Briefly, iron pyrite is an earth abundant semiconductor material with properties that make it desirable for photovoltaic energy conversion. Due to iron pyrite's strong optical absorption ($\alpha_o > 10^5$ cm^{-1} for $h\nu > 1.3$ eV) it could potentially serve as a thin absorber layer[143, 141, 232] or optical absorber material in inorganic or hybrid devices[233, 195].

This chapter will investigate the feasibility of our iron pyrite films for use in hybrid photovoltaic devices by performing photoluminescence (PL) quenching measurements[195] with a conjugated polymer. The PL quenching measurements compare the PL of the conjugated polymer separately and in contact with the pyrite thin films. A reduction in the PL, known as quenching, provides an upper-bound for charge-separation at the polymer/pyrite interface. Such experiments provide a check on the quality of the iron pyrite material without dealing with the complexities of an entire device architecture and multiple processing steps. Note that we attempted to produce some Schottky devices (i.e., all inorganic with Au contacts) in parallel with this work but were unable to maintain the integrity of the transparent conductor, ITO (indium tin oxide) or FTO (fluorine-doped tin oxide), through the high-temperature sulfurization steps. Schottky cell architectures are reported in the literature[187], but required several material layers and processing undeveloped within our group. As our goal was a test of the material properties of the iron pyrite for photovoltaics, the hybrid approach was chosen for pragmatic reasons; the processes required were well known to our chemistry collaborators, and therefore presented a more viable route forward.

We collaborated with Dr. Brian Worfolk, then of Dr. Buriak's group in the Department of Chemistry to guide our choices of polymers, and prepare and process the polymers for this work. Together, we worked with Dr. Michael Taschuk from our own group to make the photoluminescent quenching measurements. The measurements were performed in Dr. Al Meldrum's laboratory in the physics department.

We have chosen to use an organic polymer as the photoluminescence source and electron donor to match the equipment capabilities of Dr. Mel-

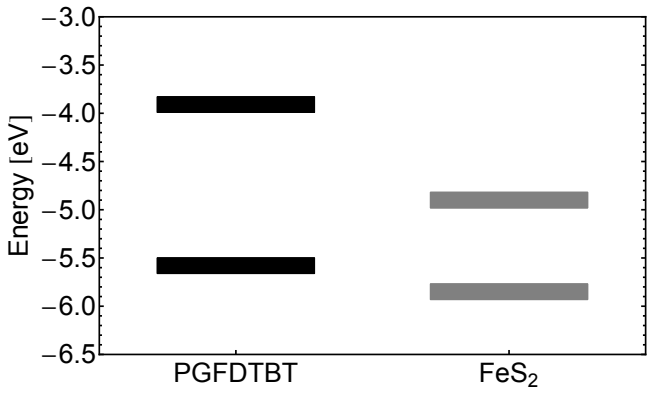

Figure 5.1: Band diagram comparing the HOMO and LUMO levels of PGFDTBT with the conduction and valence bands of FeS_2. Values were taken presented here are taken from the literature [12, 13]. Our collaborators in The Department of Chemistry also attempted for confirm the electrochemical band-structure of our iron pyrite with cyclic-voltametry measurements.

drum's lab. There are several candidate polymers with appropriate band alignment with iron pyrite that will serve this purpose. With the assistance of Dr. Brian Worfolk, a conjugated polymer abbreviated as PGFDTBT[ii] (HOMO = 5.58 eV, LUMO = 3.91 eV)[13] was chosen as the donor since its energy levels form a type-II heterojunction (staggered gap, Figure 5.1) with iron pyrite (valence band maximum = 5.85 eV, conduction band minimum = 4.9 eV expected) and it exhibits photoluminescence [12]. This polymer has been successfully integrated into all-organic bulk heterojunction type architectures for photovoltaics[13] and thus is a promising candidate for pairing with iron pyrite.

5.2 Experimental details

5.2.1 Iron film deposition

At the time of this study, we were still exploring the use of sputtered-GLAD to induce structuring. Except for the change to sputtering from electron-

[ii]Full name of PGFDTBT is Poly[2,7-(9,9-di-n-octylgermafluorene)-alt-5,5-(40,70-di-2-thienyl-20,10,30-benzothiadiazole)]

beam evaporation, the deposition process was similar to that in Section 4.2.1.

Iron thin films were sputtered onto Si substrates ($\langle 100 \rangle$, p-type) in a high vacuum system pumped to a pressure of 0.1 mPa to 1 mPa before deposition. Metallic iron targets (Kurt J Lesker, 50.8 mm diameter, 1.6 mm thick, 99.9 % pure) were sputtered in voltage regulation mode (Advanced Energy Pinnacle+, 550 V, 5 kHz repetition rate, 0.4 μs reverse time). Film thickness was adjusted by changing the amount of energy delivered to the sputter target (50 kJ, 100 kJ, 200 kJ, and 500 kJ) and porosity was adjusted by manually changing the deposition angle ($\alpha = 0°, 70°, 80°, 85°$) at a throw distance of 150 mm (target to substrate chuck center). Deposition pressure was reduced to less than 66 mPa with a tantalum hollow cathode operated in current regulation mode at 1 A.[169, 81] Ar working gas was flowed into the deposition chamber through the tantalum hollow cathode at a flow rate of 16.0 sccm. Briefly, the hollow cathode assists in reducing the working pressure by creating a secondary plasma at the gas inlet and by creating excess electrons through thermionic emission. Additional technical details of the sputter system are provided in Appendix E.

5.2.2 Iron film sulfurization

After deposition the Fe films were sulfurized in a tube furnace (Lindburg Blue M, single-zone) similar to the method used by Dahman.[149] Samples were placed in a 25.4 cm diameter fused quartz tube with 5 g of sulphur (Alfa Aesar, 99.9995 %, CAS No. 7704-34-9) placed in a quartz crucible. Ar flow gas (7 sccm) carried vaporized sulfur across the sample surface. The tube was heated to 400 ℃ from room temperature at a rate of $10\,℃ \cdot \mathrm{min}^{-1}$ and held there for 6 hours.

5.2.3 Characterization

We characterized the sulfurized sample morphology with SEM (Hitachi S4800), the surface topology with tapping mode atomic force microscopy (AFM: Digital Instruments Multimode AFM), the crystal phase by XRD, and the composition with ToF-SIMS and Auger electron spectroscopy (AES).

X-ray diffraction patterns were taken with a Bruker D8 Discover operated in a symmetric scanning mode. The goniometer was equipped with a Cu Kα radiation source, 0.5 mm collimator and a scintillator detector positioned 15 cm from the sample.

The AES and ToF-SIMS characterizations were performed at the Alberta Center for Surface Engineering and Science. Composition depth profiles were measured in the ToF-SIMS IV instrument (ION-TOF GmbH). A Cs^+ ion beam (1 kV, 75 nA) rastered over approximately a 200 μm $\times$ 200μm area was used for sputter etching and the secondary ion signal was generated by a Bi^+ beam (25 keV, 0.7 pA) within a 40 μm $\times$ 40 μm area at the centre of the etched crater.

The AES measurements were carried out using a JAMP-9500F Auger microprobe (JEOL). The instrument is equipped with a Schottky field emitter that produces an electron probe diameter of about 3 nm to 8 nm at the sample. The accelerating voltage for both SEM and AES was 20 kV and the probe current for AES was 7 nA. The working distance was about 24 mm. The sample was rotated 30° away from the primary electron beam to face the electron energy analyzer in Auger measurement and a M5 lens with 0.6% energy resolution was used for Auger spectroscopy.

The Auger peaks of Si KLL (1614 eV), Fe LMM (712 eV), and S LVV (146 eV) were selected for the line profile. The intensity of each pixel in the Auger image was calculated by $(P-B)/B$, where P and B are the peak and background intensity respectively. This intensity definition helps to reduce the edge effect of islands and dots. An auto probe tracking technique was used to compensate for possible drifting of the image during the analysis as a result of power instabilities.

5.2.4 Polymer preparation and spin coating

The PGFDTBT polymer was prepared for spin coating similarly to Allard et al.[13] and dissolved in o-dichlorobenzene at a concentration of 25 mg mL^{-1} and mixed at 75 ℃ for at least 48 hours. All substrates were pre-heated to 80 ℃ before spin coating. The polymer solution was heated to 90 ℃ and

100 μL of polymer solution was spun onto the iron pyrite samples at a spin speed of 600 rpm for 60 s followed by 2000 rpm for 5 s. Samples were air dried for 2 hr in darkness before photoluminescence measurements.

5.2.5 Absolute photoluminescence quenching measurements

Absolute photoluminescence (PL) quenching measurements allow us to estimate the number of photons absorbed by the conjugated polymer that are re-emitted in the PL spectra. A decrease in the number of re-emitted photons indicates that a fraction of the corresponding excitons where unable to recombine radiatively. We report these effects with a PL quenching value that indicates the ratio of re-emitted photons N_γ in the test sample to those produced by the polymer reference $N_{\gamma O}$. Thus, a smaller quenching value indicates less radiative recombination and a larger upper-bound for charge-seperation at the interface.

$$\text{Quenching} = N_\gamma / N_{\gamma O} \tag{5.1}$$

Photoluminescence was excited with an unfocused HeCd laser (442 nm, Omnichrome Series 56). Power on the target was monitored using a single surface reflection from a quartz wedge and a reference power meter (Newport 1815-C). The reference was calibrated using an optical power meter as a traceable standard (Gentec-EO, PH100-Si). Combining variability in the laser output (0.5 %) and the absolute calibration accuracy, the laser power on the target was (16.0$\pm$0.4) mW. The full-width half-maximum illumination spot size was (1.51 $\pm$ 0.05) mm measured using the knife edge technique.[234] The beam was nearly Gaussian with a peak irradiance on the target of (620 $\pm$ 35 mW $\cdot$ cm^{-2}).

The PL was measured using an optical fibre-coupled compact CCD spectrometer. An optical schematic for these measurements is provided in Figure 5.2. The first fibre (Ocean Optics, NA 0.4, High-OH, 600 μm core, 1 m long) was positioned approximately 14 cm from the illumination spot at an angle of 8° from the laser axis. The collection fiber was coupled to another

fibre (Ocean Optics, NA 0.4, High-OH, 600 μm core, 0.5 m) through a long-pass filter with a 475 nm cutoff that removed scattered laser light before the spectrum was measured by the spectrometer (Ocean Optics USB2000). The combined radiometric response of the compact CCD, both fibres, and the band pass filter was calibrated using a 150 W Xe lamp (Oriel 6256 bulb in an Oriel Photomax 60100 housing) filtered through a 0.25 m monochromator (Oriel MS 260i). Output light from the monochromator was monitored using both surface reflections from a quartz window ($\sim 8\%$) and the optical power meter as a traceable standard (Gentec-EO, PH100-Si). A calibrated diffuse reflector (Labsphere SRS-99-010) was used to scatter light from the lamp-monochromator combination to the first fibre's aperture.

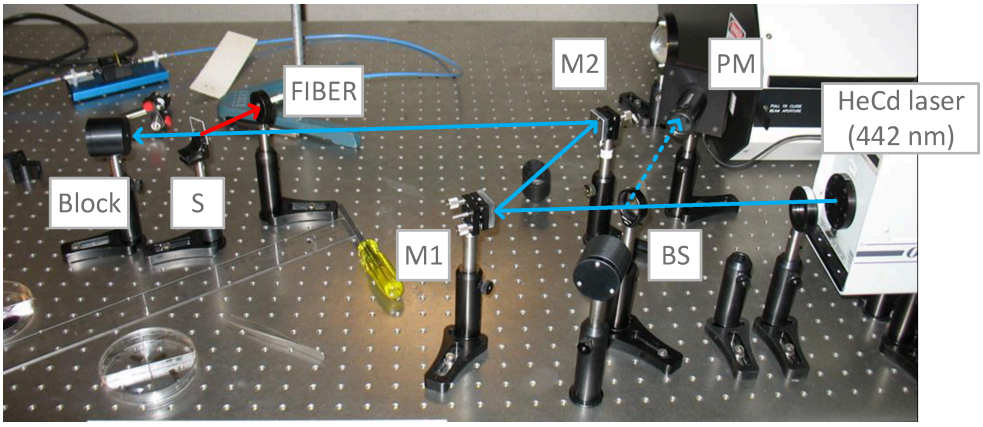

Figure 5.2: Schematic of the setup for the photoluminescence measurements. M = mirror, BS = beam splitter, S = sample, PM = power monitor.

The PL measurements were performed in random triplicate across all samples including a Si/PGFDTBT control sample to normalize any systematic error. We observed a bi-exponential decrease ($\tau_1 = 2$ min, $\tau_2 = 32$ min) in PL efficiency under the illumination conditions described above. To ensure capture of the peak photoluminescence signal, spectra were obtained in free-running mode starting with the laser light blocked. Once the spectrometer was acquiring signals the sample was exposed to the laser for ≈ 5 s before the block was replaced. Each photoluminescence measurement was performed on a fresh spot to avoid signal degradation from cumulative illumination.

After PL measurements, PGFDTBT thickness was measured using a white light interferometer (Zygo Optical Profilometer) and SEM (Hitachi S4800). For the Zygo measurements, a razor was used to scrape the spin-coated PGFDTBT and iron pyrite layer off the silicon wafers. Step profile measurements were taken for at least four positions across each sample. For the SEM measurements, samples were cleaved and examined in cross section. Reflection and transmission measurements were performed with a spectroscopic ellipsometer (V-VASE with Autoretarder, J. A. Woollam Co., Inc.) and a spectrophotometer (Perkin-Elmer NIR-UV).

Optical model for photoluminescence

The iron pyrite substrate acts as a strong optical absorber. For the polymer/pyrite/Si samples studied here, any light that enters the iron pyrite may be assumed as absorbed. Based on optical transmission measurements, the absorption coefficient of our iron pyrite at 442 nm is around $1.8 \times 10^5\,\mathrm{cm}^{-1}$. Our thinnest iron pyrite film is about 30 nm, and our thickest film is just under 300 nm.

The following calculations will demonstrate the nearly perfect absorption of the FeS_2 in the polymer/pyrite/Si system. Following the thin film optical model in Figure 5.3a laser light is incident on the sample from the left (1), and a fraction of the incident light penetrates into the iron pyrite layer (2). Some of the light within the iron pyrite layer is transmitted to the substrate, and lost to the system (3a); the remainder is reflected, and returns through the iron pyrite layer (3b). The remaining unabsorbed light escapes the iron pyrite layer (4).

Thus we can estimate the fraction of light returning to the polymer after making a single pass through the iron pyrite layer as,

$$R = 10^{-2\alpha_{o_{FeS_2}} t_{FeS_2}} (1 - R_{poly:FeS_2})^2 R_{FeS_2:Si} \tag{5.2}$$

where $\alpha_{o_{FeS_2}}$ is iron pyrite's absorption coefficient[iii], and t_{FeS_2} is the iron pyrite's thickness. For the results presented in this thesis, we find

[iii] Here we use powers of 10 instead of e.

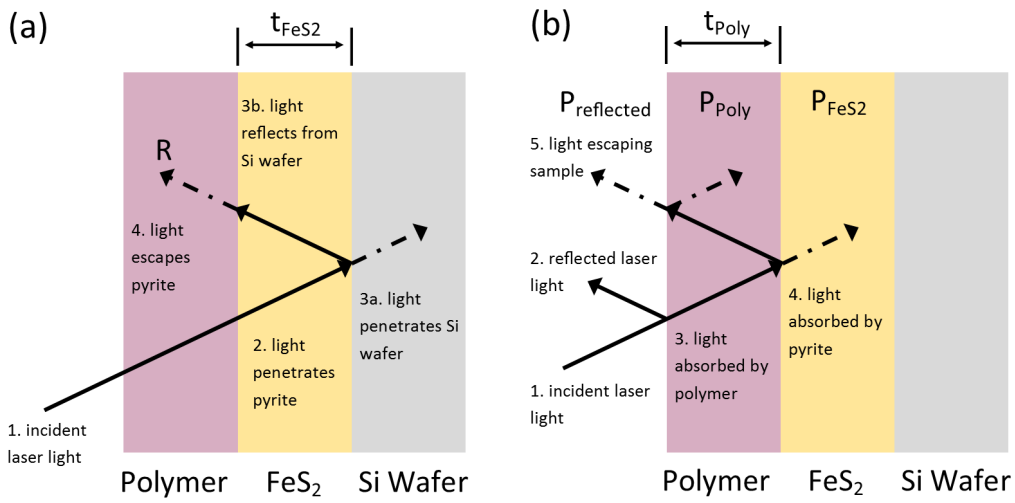

Figure 5.3: (a) Schematic of thin film optical model, demonstrating that iron pyrite acts as a nearly perfect absorber for the excitation laser used here. (b) Schematic for derivation of optical model. We use a two pass model to approximate the optical behavior of the Poly:FeS_2:Si wafer multilayer stack.

$$0.076 < R_{poly:FeS_2} < 0.137 \tag{5.3}$$

and

$$0.017 < R_{FeS_2:Si} < 0.053 \tag{5.4}$$

The range in these parameters reflect our uncertainty in the indices of iron pyrite and the conjugated polymer. These extremes will occur at opposite times – when the losses are high at the poly:FeS_2 interface, they will be lower at the FeS_2:Si interface. In the worst case, using our 30 nm iron pyrite film, we expect R values of approximately

$$R = 10^{-2(1.8\times10^5\ \mathrm{cm}^{-1})(30\times10^{-7}\mathrm{cm})}(1-0.076)^2(0.053) = 3.8\times10^{-3} \tag{5.5}$$

About one part per thousand of light coupled to the 30 nm pyrite film will re-enter the polymer PGFDTBT layer. As the thickness increases to 100

nm, the expected reflectance drops to the part per million level. In all cases, the returning light is negligible. The iron pyrite layer can be treated as an infinite sink. This feature simplifies subsequent analysis, as we can ignore any returning beams from the iron pyrite layer and the Si substrate layer.

A schematic of our poly:FeS_2 system is shown in Figure 5.3b. Following this scheme, and applying the infinite sink approximation, it can be shown with a simple thin film reflection model that the power transmitted through the polymer film and absorbed by the iron pyrite layer is

$$P_{FeS_2} = P_{incident}((1 - R_{Air:poly})10^{-\alpha_{o_{poly}} t_{poly}}(1 - R_{poly:FeS_2})) \tag{5.6}$$

where $P_{incident}$ is incident laser power, $R_{Air:poly}$ is the Fresnel reflection from the air:polymer interface, and $R_{poly:FeS_2}$ is the Fresnel reflection from the polymer-iron pyrite interface.

Similarly, it can be shown that light that is reflected by the combined system is given by

$$P_{reflected} = P_{incident}(R_{Air:poly} + (1 - R_{Air:poly})^2 R_{poly:FeS_2} 10^{-2\alpha_{o_{poly}} t_{poly}}) \tag{5.7}$$

The fraction of laser light surviving the first two passes within the polymer film may be calculated using the second term in the above equation. For a 100 nm PGFDTBT film, about 3% should be available for a third pass through the PGFDTBT. Given the experimental uncertainties, this quantity is considered negligible.

The fraction of incident power absorbed by the PGFDTBT, and available for driving PL processes, is $P_{incident} - P_{FeS_2} - P_{reflected}$. The distribution of laser power as a function of PGFDTBT thickness is shown in Figure 5.4.

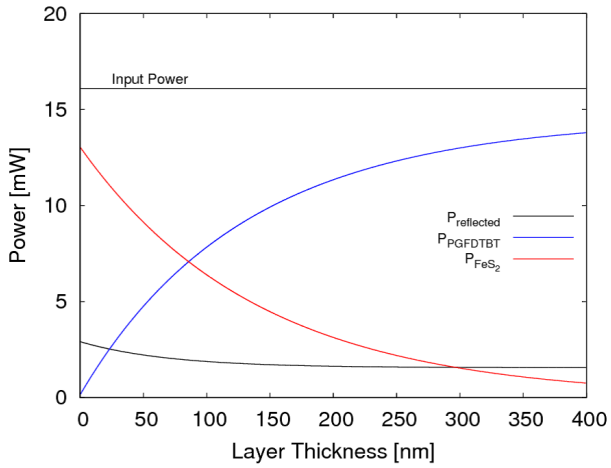

Figure 5.4: Distribution of incident laser light into the different components of the PGFDTBT:FeS_2 system as a function of PGFDTBT layer thickness. For thin films, most light is coupled to the iron pyrite layer. As the PGFDTBT layer thickness increases, more light is coupled into the polymer, and less survives to be absorbed by the iron pyrite.

5.3 Results

5.3.1 Sulfurized iron pyrite films

Morphology

Porous, columnar Fe films were deposited with GLAD on Si substrates and then sulfurized in a tube furnace under Ar flow with sulfur powder at 400 ℃ (Table 5.1). As mentioned previously in Chapter 4, during sulfurization the precursor Fe films undergo a volume expansion of approximately 3.5 times due to the density difference between iron (7.87 $g \cdot cm^{-3}$) and iron pyrite (4.89 $g \cdot cm^{-3}$) and the constrained volume/mass of the Fe precursor film. The sulfurization process is described by the following net reaction: $4Fe_{(s)} + S_{8(g)} \rightarrow 4FeS_{2(s)}$. The internal stress generated during phase transformation may be reduced by creating grain boundaries and/or voids in the precursor films.[150] The porosity of films deposited by GLAD increases with the deposition angle (α) as shown for the Fe films in Figure 5.5. After sulfurization, we observe that the sulfurized films' top surface morphology reflects

the increase in porosity of the precursor films as shown in Figure 5.6. The thickness of the Fe precursor film deposited at $\alpha = 85°$ was varied from 42 nm to 11 nm. The grain size and shape remain constant, but voids in the film disappear in the thinnest film, indicating a decrease in porosity (samples A–C in Figure 5.6). A decrease in the deposition angle of the Fe precursor (Figure 5.5) tends to lead to a decrease in void density and roughness on the surface of sulfurized films (samples D–G in Figure 5.6).

Table 5.1: Sample legend for the sulfurized iron pyrite films produced from sputtered GLAD precursors. Quenching was defined in Eq. 5.1. The sulfurized film thickness (t_{FeS_2}), Fe precursor deposition angle (α_{Fe}), Fe precursor thickness (t_{Fe}), thickness ratio, and XRD crystallite size D calculated from the (200) peak are shown.

Sample	Quenching [unitless]	t_{FeS_2} [nm]	α_{Fe} [°]	t_{Fe} [nm]	t_{FeS_2}/t_{Fe}	$D_{(200)}$ [nm]
A	0.66	125 ± 5	85	42 ± 2	2.9 ± 0.2	37 ± 1
B	0.67	80 ± 5	85	26 ± 3	3.1 ± 0.4	68 ± 1
C	1.2	33 ± 14	85	11 ± 2	3 ± 1	9 ± 1
D	0.66	109 ± 5	85	42 ± 2	2.6 ± 0.2	31 ± 3
E	0.96	161 ± 3	80	46 ± 4	3.5 ± 0.3	31 ± 3
F	0.81	179 ± 4	70	53 ± 3	3.4 ± 0.4	28 ± 1
G	0.87	274 ± 4	0	89 ± 2	3.1 ± 0.1	30 ± 1

The surface roughness of the samples D–G (Table 5.1) was measured directly by tapping-mode AFM. Reconstructions of the surface topology are shown in Figure 5.7. The surface roughness of the samples is plotted in Figure 5.7b and shows a gradual increase with the deposition angle, with a sudden jump at $\alpha = 85°$. This is not unexpected, as many other works have demonstrated a dramatic increase in porosity at $\alpha \geq 80°$.[4]

Cleaved cross-sections of the sulfurized films (example shown in Figure 5.8) demonstrate that the films are composed of globular equiaxed grains. Previous work[235, 150] on adjusting the grain size and surface morphology of Fe precursor films showed that sulfurized films were composed of a top columnar layer and a bottom layer of globular grains. In that work the authors proposed that the globular grains in the bottom layer resulted

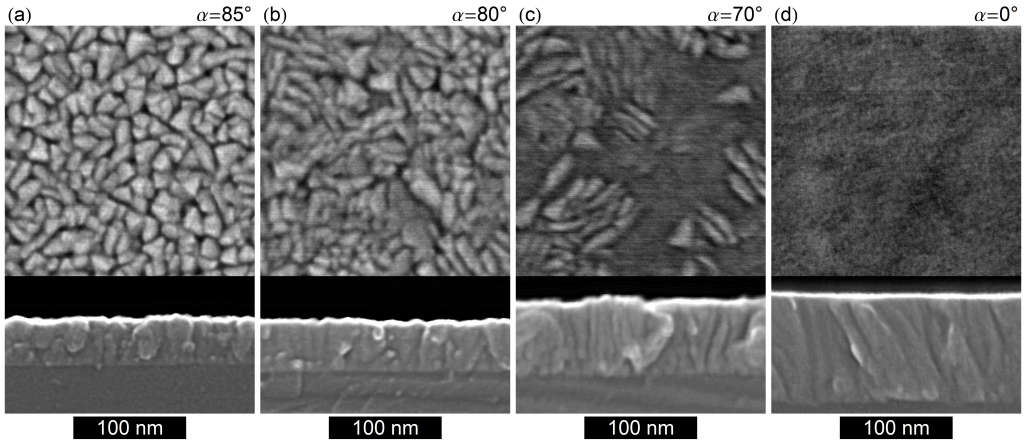

Figure 5.5: SEM images of precursor Fe films deposited at 85°, 80°, 70°and 0°in plan-view (top) and edge-on (bottom) perspectives. Precursors were used for sulfurized samples A, D, E, F and G from Table 5.1.

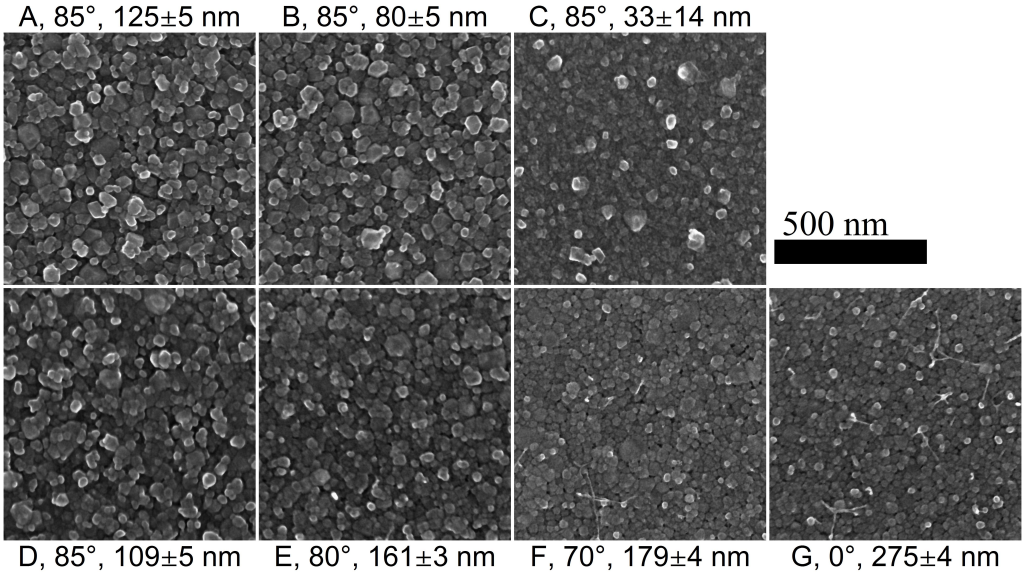

Figure 5.6: Top down SEM images of iron pyrite films labelled according to Table 5.1. The image labels indicate the sample, deposition angle (α), and the iron pyrite film thickness (t_{FeS_2}).

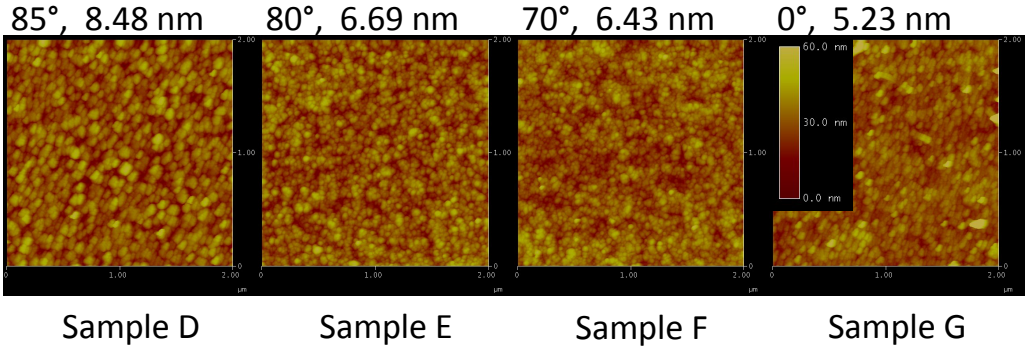

(a)

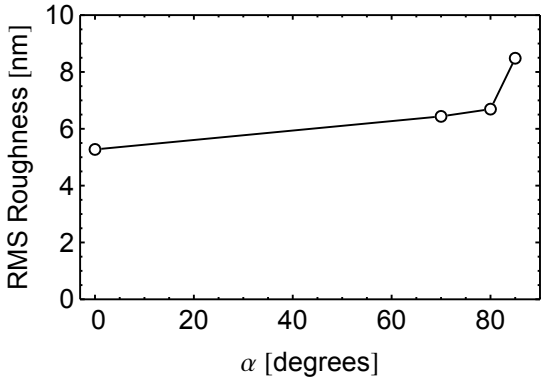

(b)

Figure 5.7: In (a) we show the surface reconstruction of Samples D-G measured by AFM. The labels are indicate the deposition angle and RMS surface roughness measured by AFM. In (b) the RMS roughness is plotted against the deposition angle

.

from the sulfur-rich environment created by diffusion through the top-layer. The equiaxed grains we observe are consistent with this interpretation as free surfaces are exposed to sulfur throughout the porous GLAD precursors. Therefore, globular growth would be expected to occur in the entire film in the GLAD case.

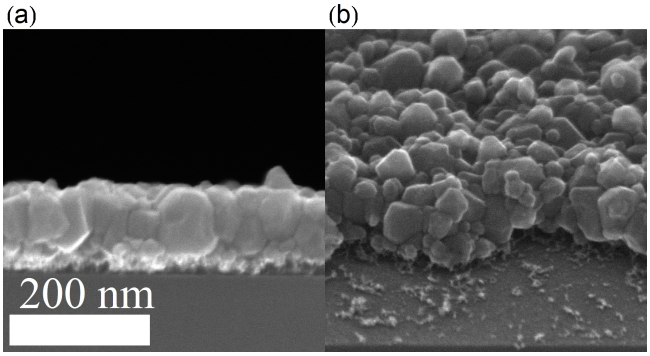

Figure 5.8: Cleaved cross section (a) and 30° oblique (b) SEM images of sulfurized sample A from Table 5.1.

Porous Fe films should permit the volume expansion that occurs during phase transformation to take place in both the lateral (in-plane) and substrate normal directions. The volume expansion was measured in one dimension by measuring the ratio of film thickness between the precursor and sulfurized film. For volume expansion occurring entirely in the normal direction (bulk film case), a thickness ratio of approximately 3.5 times is expected, whereas isotropic expansion reduces the expected thickness ratio to about $3.5^{1/3} \approxeq 1.5$ times. A plot of the measured thickness ratio with deposition angle in Figure 5.9 shows that the thickness ratio decreases at $\alpha = 85°$, which is consistent with the increased porosity of the precursor films (Figure 5.9) allowing for expansion in the lateral direction. Note that no correlation between the thickness ratio and Fe initial thickness is observed, revealing that the trend is due to changes in deposition angle.

We did not observe delamination of the sulfurized films discussed here. Delamination was only seen for films sulfurized from Fe films of low porosity ($\alpha = 70°$ and $\alpha = 0°$) produced by a different set of sulfurization conditions (140 sccm Ar flow, preheat 200 ℃ for 2 hr, anneal 400 ℃ for 10 hr). Films

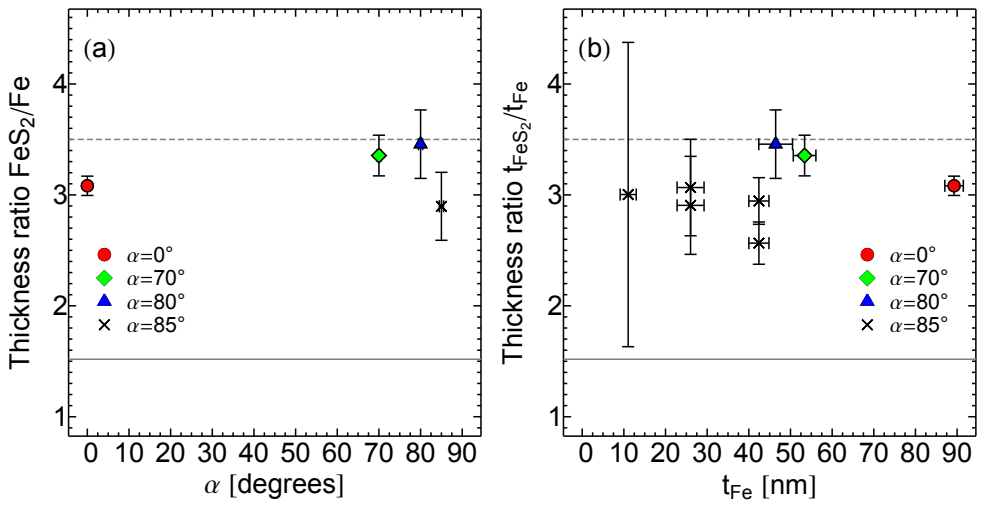

Figure 5.9: Measurement of the thickness ratio between the Fe precursor film thickness and sulfurized film thickness plot against (a) the deposition angle (α) and (b) the thickness of the porous precursors t_{Fe}. In (a), the films at $\alpha = 85°$ have been averaged for presentation. A full listing of the data is given in Table 5.1. At large deposition angles, the Fe films become porous and the thickness ratio decreases. Porous films are expected to undergo expansion in the lateral as well as normal directions during phase transformation, which reduces the thickness ratio. The maximum expected expansion ratio for bulk films (dashed line) and minimum expected expansion ratio occurring for isotropic expansion of a sufficiently porous film (solid line) are shown for comparison.

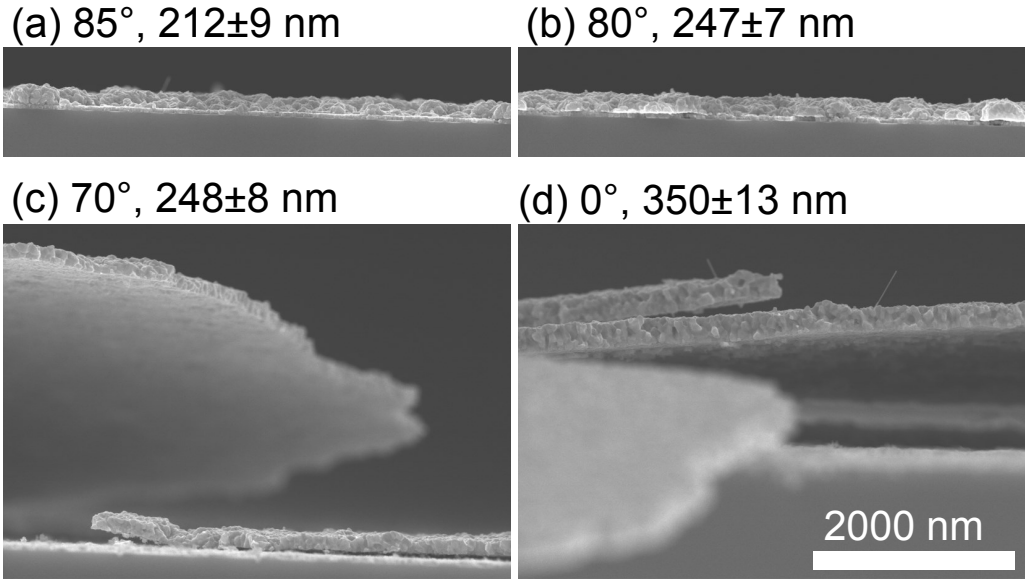

Figure 5.10: Survival of films after sulfurization under high-flow and a pre-heat treatment. Films that lack sufficient porosity (c,d) are seen to delaminate. The deposition angle and film thickness are shown above each image.

sulfurized with this alternate recipe deposited at $\alpha = 80°$ and $\alpha = 85°$ did not delaminate (Figure 5.10). This result suggests that delamination is dependent on both precursor porosity and the sulfurization process.[157, 159, 158, 236, 235]

Composition

X-ray diffraction patterns (Figure 5.11) taken for each of the sulfurized films shown in Figure 5.6 (samples A-G from Table 5.1) are consistent with films composed of cubic iron pyrite (ICDD 01-079-0617). In several of the samples there are peaks around $2\theta = 54°$ and $2\theta = 65°$ that cannot be attributed to iron pyrite and may be due to the (002) or (130) peaks ($2\theta = 54°$) and (310) peak ($2\theta = 65°$) of the marcasite (ICDD 01-075-6904) phase. The presence of a marcasite phase has been observed previously.[237, 238] The pyrite phase of FeS_2 occurs in a narrow composition range and is only slightly preferred thermodynamically over marcasite [187], and in some cases, the marcasite phase can be preferred kinetically.[136] Therefore, without rigorous control

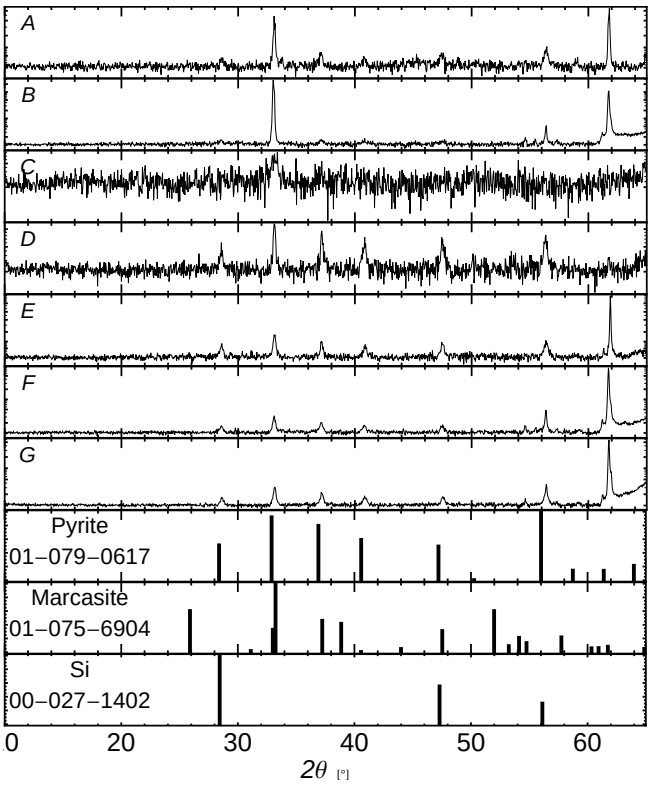

Figure 5.11: X-ray diffraction patterns for each of the samples (labeled top right, see Table 5.1). Powder diffraction patterns for the pyrite, marcasite phase and x-Si shown for comparison.

over the sulfurization environment, some marcasite can be expected. As can be seen from Figure 5.11, all the samples except the thinnest (C, 33 nm thick) appear to be crystalline. Iron pyrite has a large linear attenuation coefficient ($\mu_{\chi m} \approx 10^8\,\mathrm{m}^{-1}$). Therefore, samples even ≈ 10 nm thick interact strongly with the incoming x-ray beam, with less than 5% of the incoming beam transmitted through the film. Limited x-ray interaction can probably be ruled out as the cause of the small diffraction peaks observed in Sample C. More likely, the weak crystallinity of sample C can be attributed to phase impurity and/or a non-crystalline phase.

Crystallite sizes for each sample were computed by fitting the diffraction peaks between $2\theta = 28°$ and $2\theta = 62°$ with a Cauchy-Lorentz profile and applying the Scherrer equation (monodisperse, cubic crystallites)[170]. The crystallite sizes ranged between 24 and 32 nm, consistent with the features

observed in Figure 5.6, for all samples except sample B with a crystallite size of (68 ± 1) nm calculated from the predominant (200) peak at $2\theta = 33°$.

To verify complete sulfurization, bulk film composition of a subset of the films was investigated (samples A, D, and G) with ToF-SIMS and AES. These films were chosen since they lie at the extrema of precursor porosity investigated. Composition profiles from ToF-SIMS for porous sample (A) and the bulk film (G) are shown in Figure 5.12. The results are consistent with complete sulfurization throughout the film. Sputtering rates of FeS and S change rapidly at the film's surface and substrate interface, but stabilize in the film bulk. Note that the profiles for sample A and D (not shown) are similar as expected since they are both sulfurized from the same Fe precursors deposited at $\alpha = 85°$. An abrupt interface between the sulfurized film and Si substrate is observed for all samples. Variation in the FeS, S, and O components is seen at the free and substrate interface of the iron pyrite. The variation of both the FeS and S components is more pronounced at the free interface of samples A ($\alpha = 85°$) than in sample G ($\alpha = 0°$). This may be due to the differences in the sputtering rates caused by the voids in the surface morphology of the samples A (Figure 5.6). Oxygen from the substrate's native oxide is seen at the film-substrate interface.

Line composition profiles along a cleaved edge of sample A and sample G were also taken with AES (Figure 5.13) and corroborate the ToF-SIMS results, with Fe and S components detected throughout the film bulk. The Si component seen in the film bulk in Figure 5.13 is attributed to a combination of resolution limitations and potential Si contamination during sample preparation. Note that this spurious Si signal is not present in the ToF-SIMS data. Structure in the line profiles is attributed to edge effects on the cleaved surface.

5.3.2 PGFDTBT Photoluminescence

Hybrid inorganic-organic photovoltaics have been widely studied in recent years incorporating various inorganic semiconductors and semiconducting polymers[233, 239, 240, 241]. In general, charge generation for these next-generation photovoltaics involves: i) the absorption of light by the donor

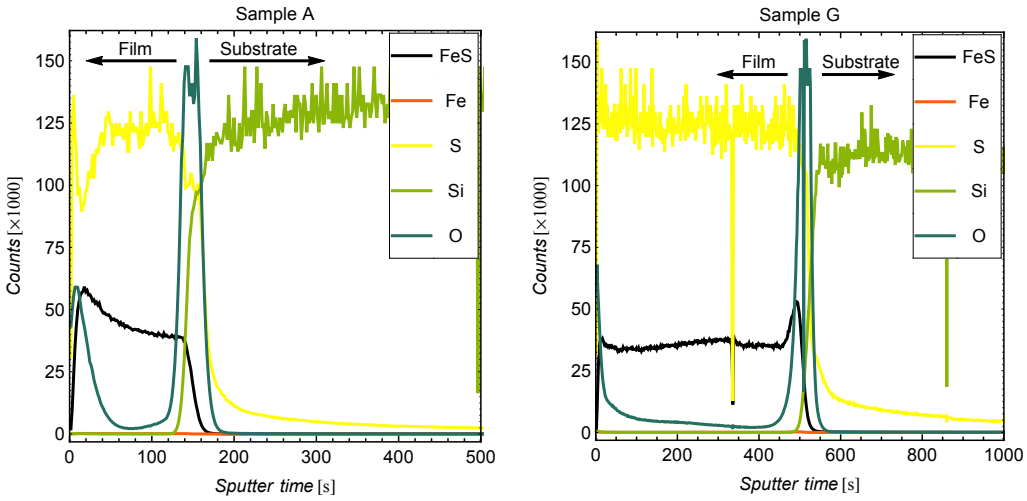

Figure 5.12: Composition depth profiles for sulfurized film samples A, (left) and G (right) taken with ToF-SIMS.

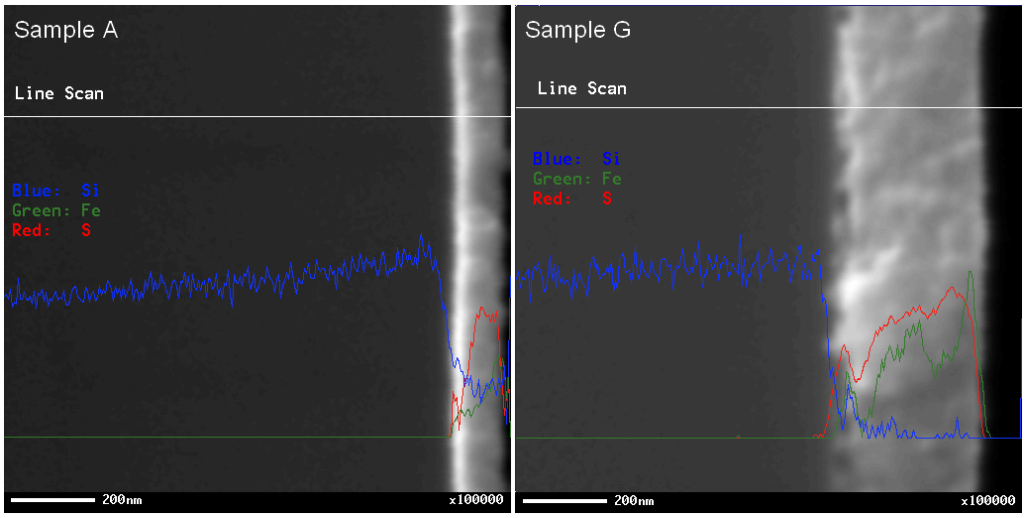

Figure 5.13: Auger electron spectroscopy line profiles of sulfurized samples A and G (Table 5.1). The white line indicates the scan line, and the blue, green and red profiles show the Si, Fe, and S components respectively. Variation in the profiles is attributed to edge effects along the cleaved surface.

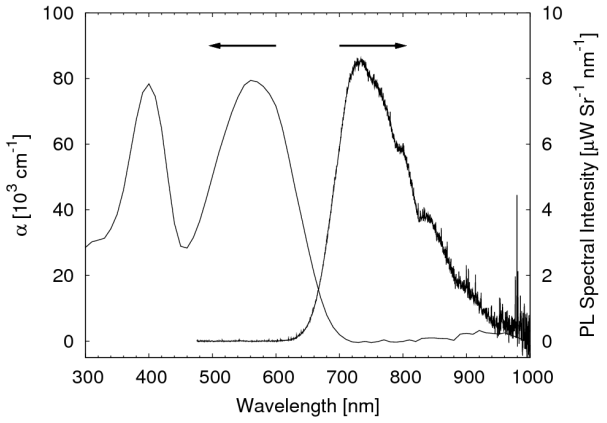

Figure 5.14: PGFDTBT absorption coefficient and photoluminescence spectra for a spun coat PGFDTBT layer on quartz.

material creating a bound exciton, ii) dissociation of the exciton at a donor-acceptor interface, and iii) transport of free carriers to the electrodes. PGFDTBT is a low-bandgap p-type polymer with a deep HOMO level with appropriate offsetting energy levels to form a type-II heterojunction with iron pyrite.[242] The absorption coefficient and absolute photoluminescence emission of a PGFDTBT layer on a Si wafer is shown in Figure 5.14. The absorption spectra is similar to that reported previously[13] but is reported in absolute units in this work. All the features from the original work by Allard et. al.[13] (the group that synthesized the PGFDTBT for us) are seen here. This includes both absorption bands at 400 nm and 580 nm and the absorption onset near 690 nm that corresponds to the optical bandgap of 1.79 eV. Note that the optical bandgap is slightly different than the electrochemical bandgap of 1.67 eV shown in Figure 5.1 [13].

The spectral photoluminescence was measured in the direction normal to the substrate. Assuming that the PGFDTBT layer is a Lambertian emitter, and correcting for the Fresnel reflection at the PGFDTBT:Si interface, the photoluminescence efficiency of PGFDTBT is approximately unity. Thus, approximately every photon absorbed by the PGFDTBT produces a photon in the PL spectra.

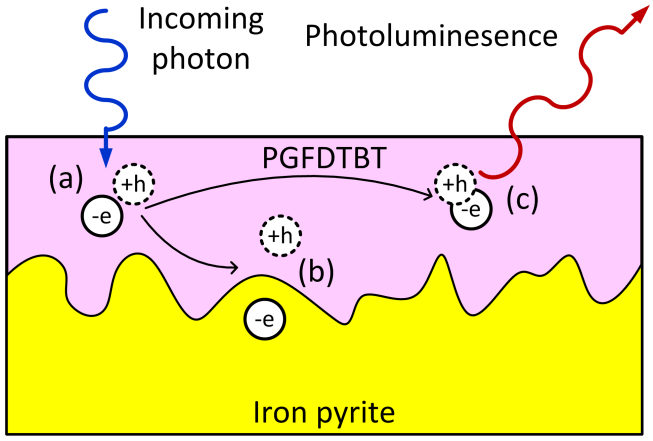

Figure 5.15: Schematic of photoluminescence quenching. In (a) a photon is absorbed in the PGFDTBT and an exciton is created. If the exciton dissociates at the PGFDTBT-pyrite interface (b) it cannot radiatively recombine and contribute to photoluminescence of the PGFDTBT (c).

5.3.3 PGFDTBT and iron pyrite photoluminescence

Photoluminescence quenching in excitonic systems occurs when an exciton is dissociated in a nonradiative process at an internal interface (schematic shown in Figure 5.15). Such quenching may indicate that the charges making up an exciton have been separated, and can therefore be used to produce electric power. Numerical results for the observed quenching are given in Table 5.1. The strongest quenching in Table 5.1 corresponds to the value of 0.66, which was observed for the highest porosity samples studied ($\alpha = 85°$). This is consistent with the surface roughness (Figure 5.7) of the films at $\alpha = 85°$ providing a larger interface area for exciton dissociation.

To properly account for changes in PGFDTBT layer thickness and reflectivity the absolute photoluminescence of the PGFDTBT-iron pyrite system was measured for all samples. An optical model of the combined system is required to evaluate quenching. It can be shown (see Section 5.2.5) that the power absorbed in the PGFDTBT layer is given by

$$P_{absorbed} = P_{in}\left\{1 - R_{o_{air:poly}} - T^2_{o_{air:poly}} R_{o_{poly:FeS_2}} 10^{-2\alpha_{o_{poly}} t_{poly}} - T_{air:poly} T_{poly:FeS_2} 10^{-\alpha_{o_{poly}} t_{poly}}\right\} \quad (5.8)$$

where P_{in} is incident laser power, R_o and T_o represent Fresnel reflections and transmissions at the interfaces, $\alpha_{o_{poly}}$ is the polymer's absorption coefficient at the laser wavelength, and t_{poly} is the PGFDTBT's thickness. Interfaces are denoted by *air:poly*(air:PGFDTBT) and *poly:*FeS_2 (PGFDTBT:iron pyrite). The reflectivity and transmission coefficients were estimated from single layer measurements on the VASE and the spectrophotometer, correcting for index matching with the quartz substrate.

Photoluminescence spectra of a reference sample (PGFDTBT on fused quartz) and sample A ($\alpha = 85°$) are given in Figure 5.16(a). The spectra are normalized to power absorbed in the PGFDTBT layer. The reflectivity (at the laser wavelength, 442 nm) and total photoluminescence power is shown in Figure 5.16(b) for the samples with an iron precursor deposited at 85°. The reflectivity data (closed squares) is fit to $P_{reflected}$, and the PL data (closed circles) is compared to curves showing different degrees of quenching. Samples A,B, and D with PGFDTBT layer thicknesses between 150 nm and 250 nm have iron pyrite layers between 80 nm and 125 nm thick. These samples show approximately a 1/3 reduction in photoluminescence efficiency. Sample C, with a PGFDTBT layer 75 nm thick has only a thin sulfurized film (33 nm) that had a weak diffraction pattern (Figure 5.11) implying that only a small crystalline iron pyrite phase is present. Thus, strong quenching was not expected from sample C. The assumptions of the optical model used for analysis may not apply well in the case of Sample C, which may explain the quenching value >1. Partial quenching was observed for all other samples. Although a decrease in PL efficiency can be caused by other non-radiative mechanisms or recombination at the interface[243, 244], these results may indicate that the required charge transfer for photovoltaic devices occurs for a wide variety of GLAD deposition conditions (Table 5.1).

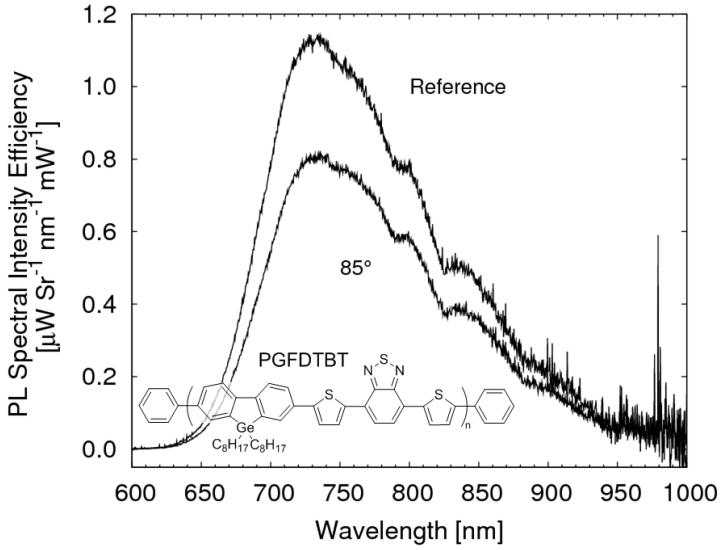

(a)

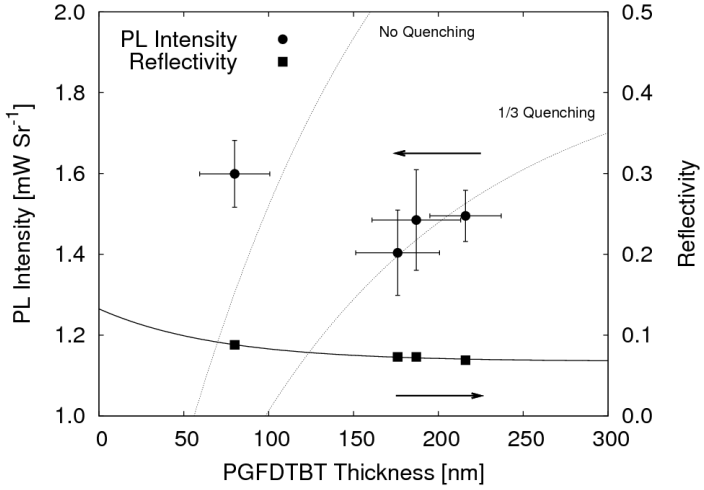

(b)

Figure 5.16: (a) Photoluminescence spectral intensity efficiency of a reference PGFDTBT layer and a PGFDTBT-pyrite bilayer system, showing quenching. The Fe GLAD precursor layer was deposited at $\alpha = 85°$. An inset shows the chemical structure of the PGFDTBT polymer. (b) Photoluminescence intensity and reflectivity (at 442 nm) of Fe precursors deposited at $\alpha = 85°$. The reflectivity curve is a fit to the optical model derived in Equation 5.7. The dashed lines show the model predictions for PL intensity with no quenching and 1/3 quenching. Sample C left of the no quenching line with a PGFDTBT layer approximately 75 nm thick exhibited weak x-ray diffraction (Figure 5.11) which indicates that a significant crystalline iron pyrite phase is not present and thus strong quenching may not be expected in sample C.

5.4 Conclusion

We have shown that the porosity of a nanostructured Fe precursor film influences the morphology of sulfurized iron pyrite. This technique was later refined in Chapter 4 to produce pyrite films with planar or columnar morphologies.

Use of columnar precursors appears to reduce the internal strain during sulfurization. Unstrained pyrite films are important for increasing mechanical robustness in device applications. As a first step towards the construction of a hybrid organic-inorganic photovoltaic device, we measured a PL quenching effect between a conjugated polymer donor (PGFDTBT) and the sulfurized iron pyrite via absolute photoluminescence quenching. This effect may suggest charge-transfer, but other non-radiative mechanisms could be responsible such as interface defects or Förster energy transfer.[244, 243] Temperature-dependent PL experiments[243], or time-resolved PL measurements could help elucidate the extent of charge-transfer between pyrite and an organic absorber. To summarize, columnar Fe precursors and sulfurization show some promise as an approach for the design and fabrication of iron pyrite thin films for photovoltaics.

This chapter concludes the work on iron pyrite sulfurization with GLAD Fe precursors. In the next chapter, we will switch to discuss some early work that was performed on tuning the morphology and microstructure of ZnO nanocolumns.

Chapter 6

Flux engineering for polycrystalline zinc oxide nanorods

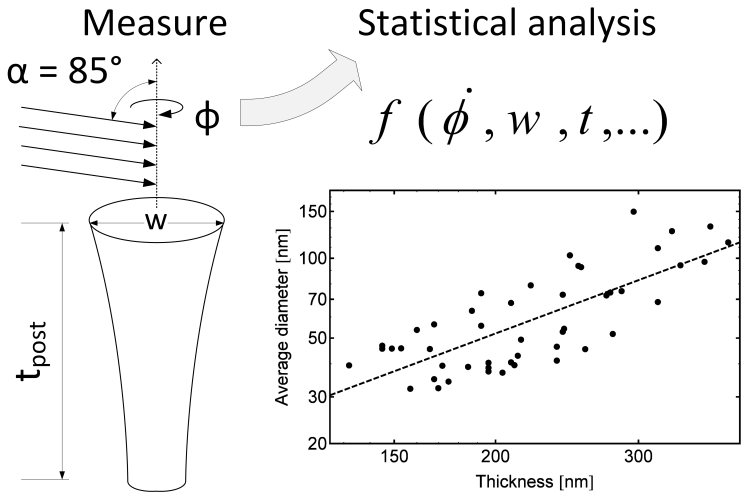

In this chapter[i], we apply several of the concepts for microstructural control and image analysis to the growth of ZnO nanorods. By systematically analyzing the growth of ZnO across a range of flux rates and deposition pitches we were able to identify different growth regimes that encourage

[i]Althought appearing last in the thesis, the work in this chapter preceded the studies in the other chapters chronologically.

or suppress the effect of changing pitch on the nanorod morphology and crystallinity. This work was published in *Thin Solid Films*[81].

6.1 Introduction

Zinc oxide possesses a combination of properties, including semiconductor electronic behavior, optical transparency, and piezoelectricity, that make it an interesting candidate for several applications including energy scavenging, photovoltaics, and chemical sensing [245, 246, 247]. Various nanostructures such as nanowires and nanoribbons [246, 248] have been formed with ZnO, with a variety of growth methods, by exploiting the difference in surface energy between the low-index crystal faces of the wurtzite ZnO crystal [249, 180] leading to preferential growth along the c-axis.

Often, GLAD growth operates under conditions of limited surface diffusion [250, 79, 251]. In general, the nanostructure's morphology is controlled by the motion of the deposition angle and the deposition pitch. However, a material's growth kinetics can impact GLAD film morphology and these effects are not well understood.

While GLAD typically produces amorphous films, there are many reports of single crystal films in the literature: Al [43, 79], Co [78], CrN [96], Cu [87, 252], Ge [88, 112], Mg [253, 254], Ti-doped Mg [89], Sn [91], Ru [83], β-phase W [182, 92], and ZnO[101]. Crystalline organic GLAD films have also been reported [255]. Despite these studies, the conditions under which GLAD produces crystalline films have not been thoroughly investigated nor explained. While a dependence on pitch has been observed for ytrria-stabilized zirconia [80], Cu [82] and Ru [83] GLAD films, detailed studies of these effects are ongoing.

Similarly, a limited number of models or mechanisms for crystalline growth in the GLAD process have been published. One model has been proposed by Karabacak et al. to explain the formation of β-W single crystal nanorods[92]. In this work, a mixture of α-W and β-W forms on the substrate during initial growth. Subsequently deposited adatoms are less mobile on the β-W phase, which favors their growth. Once this process has started, GLAD shadowing

effects ensure that the β-W islands receive more vapor flux, eventually growing into single crystal nanorods. In Chapter 3, we demonstrated the growth of crystalline Fe nanocolunms with GLAD. We proposed that evolutionary selection between the nanocolumns was responsible for the development of texture in the film. Additionally, the competitive environment, including the degree of nanocolumn crystallinity, is strongly dependent on deposition pitch in that system.

Systematic, detailed studies of the process parameters like that used in Chapter 3 are necessary to further understand crystalline growth modes in GLAD films and the role that growth kinetics have in determining film morphology. Here, we employ a parallel approach to probe the process parameter space of deposition rate, pitch and throw distance for ZnO nanorods, and observe the resulting film morphology and crystal properties. The influence of growth kinetics on nanostructure has been demonstrated for vapor-solid, vapor-liquid-solid and hydrothermal processes with ZnO, which makes it a good candidate material for this study [245, 246, 247]. We use first-order surface diffusion calculations to provide some insight into the growth kinetics of ZnO GLAD growth. A statistical analysis of the data has identified important trends, and optimal growth conditions for single-crystal ZnO nanorods have been found.

6.2 Experimental details

Zinc oxide thin films were sputtered onto Si substrates ($\langle 100 \rangle$, p-type, $\sim$ 1 cm^2) in a HV system with a base pressure of 0.1–1 mPa. Bonded ceramic ZnO targets on a copper back-plate (Kurt J. Lesker, 50.8 mm diameter, 6.35 mm thick ZnO, 6.35 mm thick Cu) were sputtered in voltage regulation mode (Advanced Energy Pinnacle+, 550 V, 5 kHz repetition rate, 0.4 μs reverse time). Each deposition ran until 720 kJ had been delivered to the target. To reduce the working pressure to 66 mPa, thereby increasing flux collimation to promote self-shadowing, argon working gas was flowed at 16.0 sccm through a tantalum hollow cathode[169] operated in current regulation mode at 1 A. Care was taken to position the tube tip directly above the erosion track, 5-10

mm from the target surface. Over several deposition runs (hours each) wear on the tube's surface caused changes in the thermionic emission current that decreased the achievable cathode power. However, the cathode power was stable for each deposition. A decrease in cathode power was necessary to achieve the low deposition rate experiments. Over the entire set of films the range of average deposition rates, calculated from measured film thickness and deposition time, varied between $0.001\,\mathrm{nm}\cdot\mathrm{s}^{-1}$ and $0.022\,\mathrm{nm}\cdot\mathrm{s}^{-1}$.

A total of nine depositions were performed at a deposition angle of 85° from the substrate normal with pitch values between 0.001 nm and 6.5 μm. For each deposition, a geared stage [43] with six Si substrates that were rotated at different rates (4.9×, 3/7×, 1×, 1/2×, 1/4×, 1/16×) was used. A computer-controlled stepper motor controlled the base rotation rate. Substrates on the stage were positioned at increasing throw distance from the target; substrate center-to-target distances were measured to be 118 mm, 139 mm, 157 mm, 173 mm, 189 mm, and 206 mm (all ±2 mm) listed in the same order as the gear ratios above.

After deposition, the films were imaged with SEM (JEOL 6301F Field Emission) and x-ray diffraction measurements (Bruker D8 Discover) were also performed. The goniometer was equipped with a Cu Kα x-ray tube with a 1 mm collimator and an area detector (Hi-Star Area Detector) positioned 15 cm from the sample.

Top-down images of the films were analyzed using ImageJ [172] to determine the average area per post, and the film's areal fraction. Images were processed by first applying a threshold using the Default or MinError(I) algorithms. Subsequently, noise and pixel cluster outliers were removed using the Remove Outliers algorithm for both black and white with a radius of 2 pixels. Any remaining gaps in the image were closed with ten iterations of the Close algorithm with four padding pixels. The image was segmented using the Watershed routine, and the image was analyzed with the built–in particle analyzer (Figure 6.1). Macros used for this analysis are presented in Appendix D.

Values for the average kinetic energy and the angular distribution of the sputter flux were simulated using SIMSPUD[256] for each of the substrates.

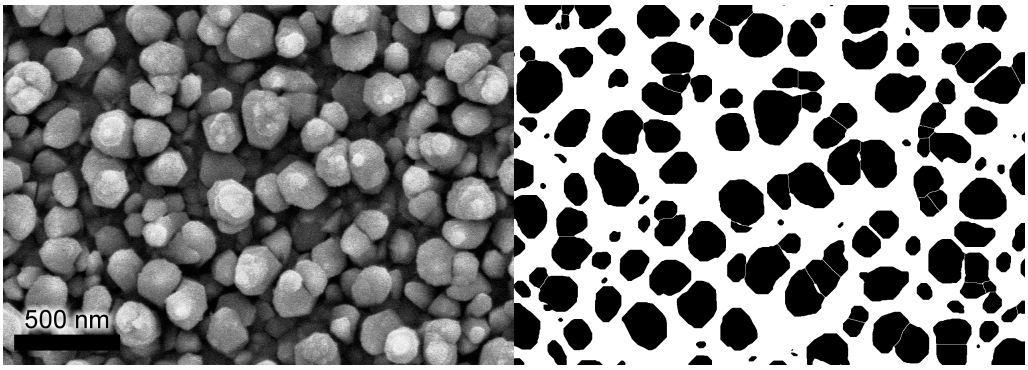

Figure 6.1: Example of a top down SEM image before (left) and after applying the thresholding routine used for image analysis (right).

Briefly, SIMSPUD (SIMulation of SPUtter Distributions) is a 3D Monte Carlo simulation that provides detailed information about the energy and angular distribution of a sputter flux arriving at a substrate. Increasing the throw distance from 118 mm to 206 mm decreased the average kinetic energy and angular flux distribution from 18 eV and 6.5° to 17 eV and 4.7° respectively. These parameters should be interpreted as approximate and indicative of relative trends due to difficulties in determining precise values for simulation input parameters.

6.2.1 Calculated Parameters

We estimated physical parameters of the growth process that are known to play a role in microstructural evolution. A complete list of parameters used during the study is presented in Table 6.1. First, we estimated the surface diffusion, Λ, following the methodology of Abelmann and Lodder[26] where Λ is approximated as the average number of hops before the adatom is buried under one atomic layer of incoming flux [26].

$$\Lambda = \tau_m/\tau_h \tag{6.1}$$

where τ_m is the monolayer growth time and τ_h is the average time between

hops. The monolayer growth time is approximated as

$$\tau_m = \frac{a}{\Gamma} \tag{6.2}$$

where a was chosen to be the length of the c-axis for wurtzite ZnO (520 pm [247]) since ZnO prefers to grow in this direction, and Γ is the deposition rate. The average time between hops is calculated as

$$\tau_h = \frac{1}{\omega} e^{E_h/(k_B T_f)} \tag{6.3}$$

where ω is the lattice vibration frequency, E_h is the energy needed for one hop (assumed to be one-fifth of the enthalpy of formation [26]), and T_f is the film temperature. Heat transfer calculations and thermocouple measurements of the rotation stage during deposition both indicate that the stage and substrate should be at thermal equilibrium with the process chamber (≈ 20 ℃) for all samples within the range of deposition conditions used in this study.

6.3 Results

Deposition onto several substrates in parallel, so that several data points are collected per deposition run, has made it possible to examine the relationships between process parameters and film characteristics (Table 6.1). We have examined a total of 14 parameters, classified as process variables (pitch, deposition rate and throw distance), morphological properties (film thickness, average post diameter, post area fraction, post aspect ratio, linear mass density, and areal post density), crystallinity properties (crystallite size, texture coefficient) and theoretical quantities (surface diffusion, average kinetic energy and angular distribution). Variance exists within the data due to the stochastic nature of film growth and uncontrolled or unknown parameters during deposition (e.g., exact position and material condition of Tantalum hollow cathode, steady state and transient temperature of growth surface, flux distribution characteristics, residual gases in the process chamber). Correlation analysis between all parameters was performed to identify

statistically significant relationships by evaluating the strength (r) and significance (p) of the relationship [257]. Briefly, the Pearson product-moment correlation coefficient, r, is a measure of the degree of linear dependence between the two random variables and ranges from -1 to 1. The significance, p, is the probability that a correlation coefficient, r, could be obtained from n samples assuming the null hypothesis (no linear dependence in this case) is true.

Table 6.1: Parameter definitions used to describe the thin film deposition process, film morphology, crystallinity and theory.

Process		Crystallinity	
P	= pitch (film thickness deposited per substrate revolution)	D	= crystallite size
Γ	= deposition rate (film thickness deposited per unit time)	χ	= texture coeffient
Morphology		**Theory**	
$t_{film} \approx t_{post}$	= post length (thickness)	Λ	= surface diffusion
w	= post diameter	$\langle E \rangle$	= average kinetic energy of flux
$\langle w \rangle$	= average post diameter	$\Delta\Theta$	= angular distribution of flux particles arriving at substrate
t_{post}/w	= post aspect ratio		
ρ_A	= post area fraction (fraction of substrate area occupied by posts)		
$\rho_{m_{lin}}$	= linear mass density (film mass/h)		
ρ_N	= areal post number density		

6.3.1 Morphology

Placement of SEM images for each film at the location in the pitch and throw distance parameter space produces a map of the film morphology (Figure

6.2). Morphological trends can be qualitatively understood using this map. Films deposited at pitch values between 0.1 nm and 10 nm and 118 mm throw distance appear to most closely approximate an ideal isolated array of ZnO nanorods (Figure 6.3).

Correlation analysis of the post aspect ratio (film thickness / average diameter) and logarithm of pitch data showed a weak relationship (Figure 6.4a). However, sorting the data by deposition rate produces a clearer relationship for low deposition rates below $0.0025\,\mathrm{nm}\cdot\mathrm{s}^{-1}$ (Figure 6.4b) and for high deposition rates above $0.01\,\mathrm{nm}\cdot\mathrm{s}^{-1}$ (Figure 6.4c). The relationship between aspect ratio and pitch is different for these two regions. At low deposition rates, it appears that aspect ratio is unrelated to pitch with a correlation coefficient of 0.25 for 11 samples ($p = 0.46$), whereas at high deposition rates a strong positive correlation ($p = 0.001$) between aspect-ratio and the logarithm of pitch is observed.

Further insight into the changing relationship can be obtained by plotting the slope and intercept of a linear fit to subsets taken from the complete dataset (Figure 6.4d). Seven consecutive points (in terms of deposition rate) were taken for each fit, and the mean deposition rate was used as the x-value. There are three regions observed in Figure 6.4, separated by deposition rates of $\approx 0.005\,\mathrm{nm}\cdot\mathrm{s}^{-1}$ and $\approx 0.01\,\mathrm{nm}\cdot\mathrm{s}^{-1}$. In the previous discussion, we stated that both heat transfer calculations and measurements with a thermocouple were consistent with the growth surface being near thermal equilibrium with the deposition chamber ($\sim$ 20 ℃). Thus even though the flux contains particles with a large kinetic energy ~ 10 eV, that energy is dissipated quickly (100 fs to 1 ps) upon condensation on the surface [26] and is not able to significantly alter the surface temperature because of the low deposition rate. At such low surface temperatures, the adatom hopping time is approximately 2000 s (Equation 6.3), and the burial time (determined by the deposition rate) is between 20 s and 350 s (Equation 6.2). Thus, adatoms on the surface have a low probability of thermally activated hopping before they are buried by incoming flux[26]. It therefore seems unlikely that thermally activated surface diffusion plays a significant role in film growth. However, two other mechanisms may contribute to the change in morphological evolution at high deposition rates.

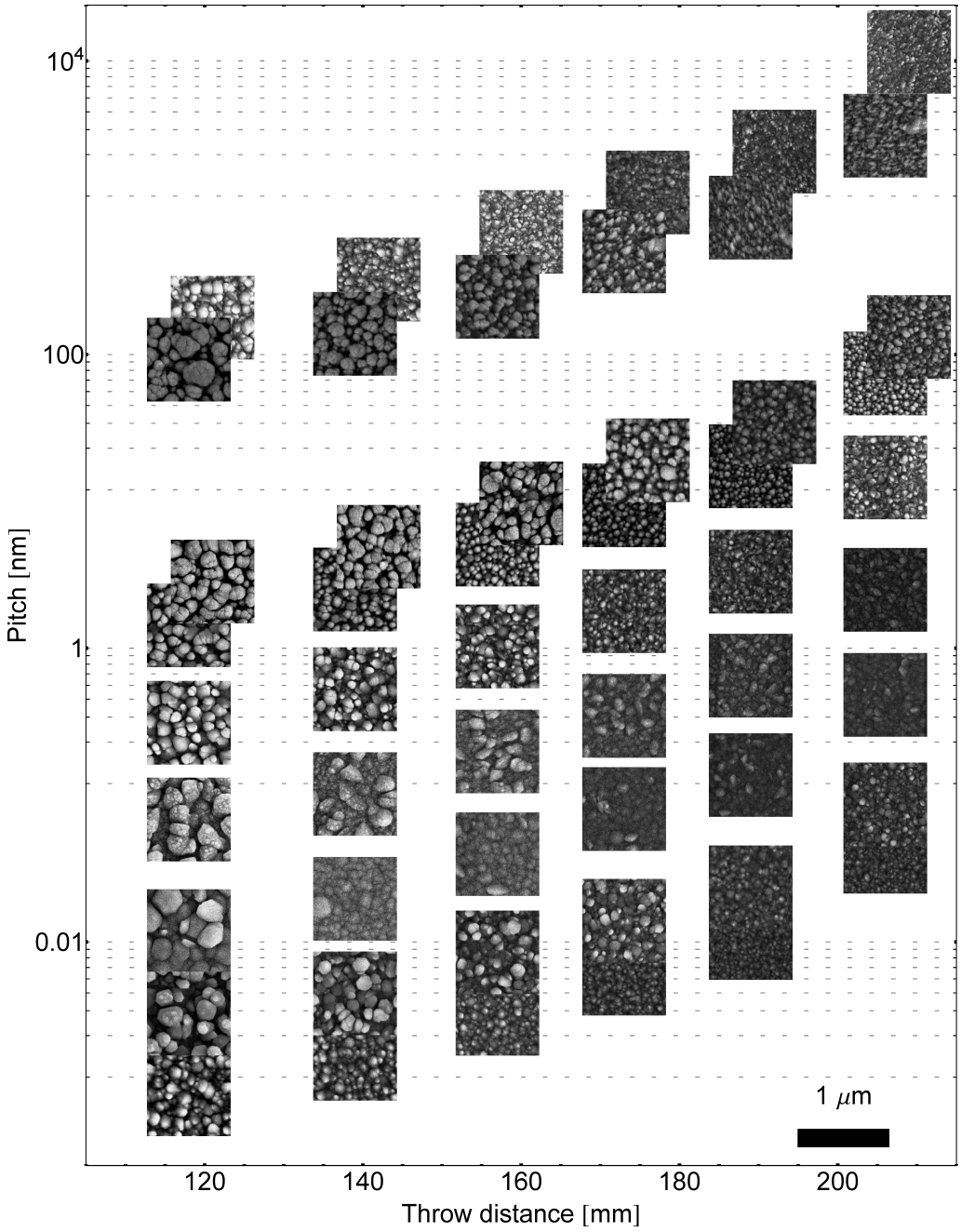

Figure 6.2: Morphology map showing SEM images located at the positions in the parameter space (throw, pitch) where that film was deposited. Note: Offset images were deposited at the same throw distances, but moved slightly along the y-axis to decrease image overlap.

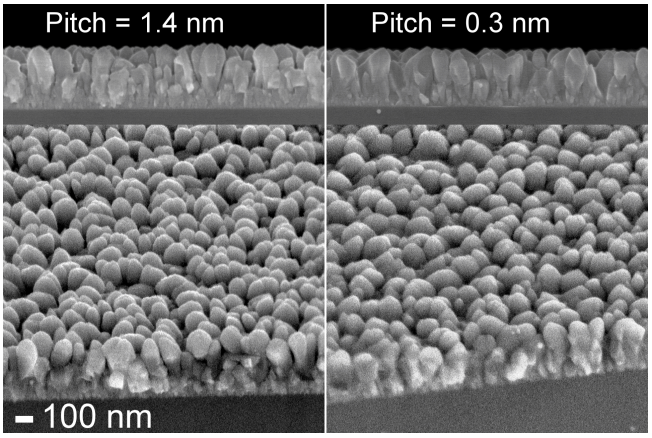

Figure 6.3: SEM images of a film deposited at a pitch of 1.4 nm, deposition rate of $0.02\,\mathrm{nm}\cdot\mathrm{s}^{-1}$, and 118 mm throw distance from an oblique angle (left-bottom) and normal to the cleaved edge (left-top). Another film deposited at a pitch of 0.3 nm, deposition rate of $0.005\,\mathrm{nm}\cdot\mathrm{s}^{-1}$, and 118 mm throw distance from an oblique angle (right-bottom) and normal to the cleaved edge (right-top).

As outlined by Adelmann and Lodder [26], surface contaminants from residual gas in the chamber can affect the diffusion of adatoms on the growth surface. Changes in the deposition rate will affect the rate of residual gas incorporation and thus the kinetics on the surface. However both the composition of the residual gas and the effect each species would have on the adatom surface diffusion is difficult to determine.

From the kinetic theory of crystal growth from a supersaturated vapor, it is known that the critical radius of adatom nuclei on atomically flat surfaces decreases as the gas pressure increases [28]. At high enough pressures the critical radius is small enough to allow frequent formation of adatom nuclei that provide strong binding sites for surface adatoms to fill and contribute to crystalline growth. In physical vapor deposition, the pressure is derived from the deposition rate. We cannot rule out that a similar deposition rate-dependent effect is responsible for the change in behavior at the high deposition rates observed here.

Detailed examination of the growth kinetics is beyond the scope of this paper. Our intention is to provide potential mechanisms by which the growth

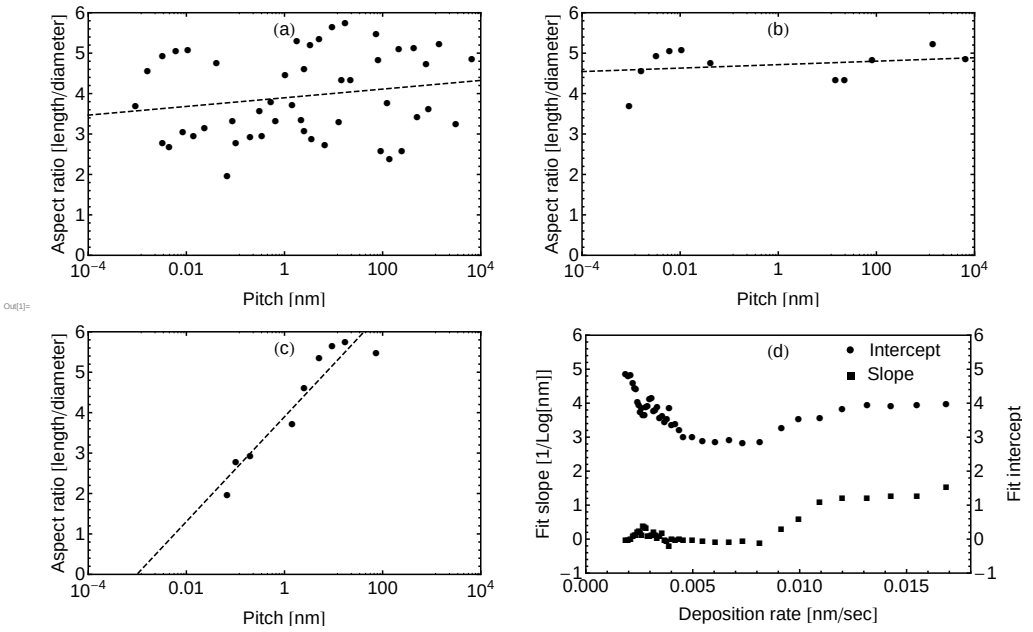

Figure 6.4: Scaling of the post aspect ratio with the logarithm of pitch for all data (a: $r = 0.19$, $p = 0.19$), at low-deposition rates of $< 0.0025\,\mathrm{nm}\cdot\mathrm{s}^{-1}$ (b: $r = 0.24$, $p = 0.46$) and high-deposition rates of $> 0.01\,\mathrm{nm}\cdot\mathrm{s}^{-1}$ (c, $r = 0.95$, $p = 0.0001$). Intercept and slope parameters of a linear fit (dashed line) to the data windowed (7 points used) across the range of deposition rates (d). The low-surface diffusion regime at low-deposition rates $< 0.005\,\mathrm{nm}\cdot\mathrm{s}^{-1}$ is seen followed by transition region until crystal growth kinetics at higher deposition rates $> 0.01\,\mathrm{nm}\cdot\mathrm{s}^{-1}$ begin to shape the evolution of the nanorods.

kinetics could be affected by changes in the deposition rate. In this context, Figure 6.4d can be interpreted as consisting of two regimes: a geometric shadowing regime at low deposition rates and a growth kinetics regime at high deposition rates. In the geometric shadowing regime, increasing deposition rates leads to a smaller average aspect ratio across all pitch values, as observed by a decrease in the intercept in Figure 6.4d. As the deposition rate continues to increase above $0.01\,\mathrm{nm}\cdot\mathrm{s}^{-1}$ growth kinetics begin to contribute to the morphological evolution of the films. Due to ZnO's preference to grow oriented along the c-axis, it is expected that a crystalline growth mode would lead to the higher aspect ratios seen in Figure 6.4.

We also observe a decrease in column diameter with increasing pitch. Similar effects have been reported by Dick et al. for SiO_2 and Bi vertical posts, who observed a decrease in column diameter before the onset of helical growth [43]. However, in the same report, Al vertical posts behaved differently, further emphasizing the importance of the choice of material system in GLAD growth.

Film thickness is primarily determined by deposition rate and time, not by pitch. Therefore it was expected from the above treatment of post aspect ratio, changes in the post diameter and post density should be observed. Indeed, similar treatment of the post density also reveals three regions separated by deposition rates of $\approx 0.005\,\mathrm{nm}\cdot\mathrm{s}^{-1}$ and $\approx 0.01\,\mathrm{nm}\cdot\mathrm{s}^{-1}$ (Figure 6.5). At low deposition rates the post density is unrelated to pitch, but as the deposition rate is increased past $0.01\,\mathrm{nm}\cdot\mathrm{s}^{-1}$ a strong correlation ($r = 0.94$, $p = 0.0001$) between post density and the logarithm of pitch emerges (Figure 6.5b). The sharp increase in the post density is primarily due to a decrease in the post diameter.

Post broadening with film growth for films deposited in the geometric shadowing regime (deposition rate $< 0.005\,\mathrm{nm}\cdot\mathrm{s}^{-1}$) is shown in Figure 6.6. Note that the scatter in the data is partly due to the variation in pitch. As expected from the literature, the relationship between these variables follow an exponential scaling relationship, predicted by Kardar-Parisi-Zhang (KPZ) fractal surface evolution theory [222, 258, 259]. KPZ theory is used to model surface evolution under conditions of limited surface diffusion and has been successfully applied to several GLAD films [222, 258]. While the data follow

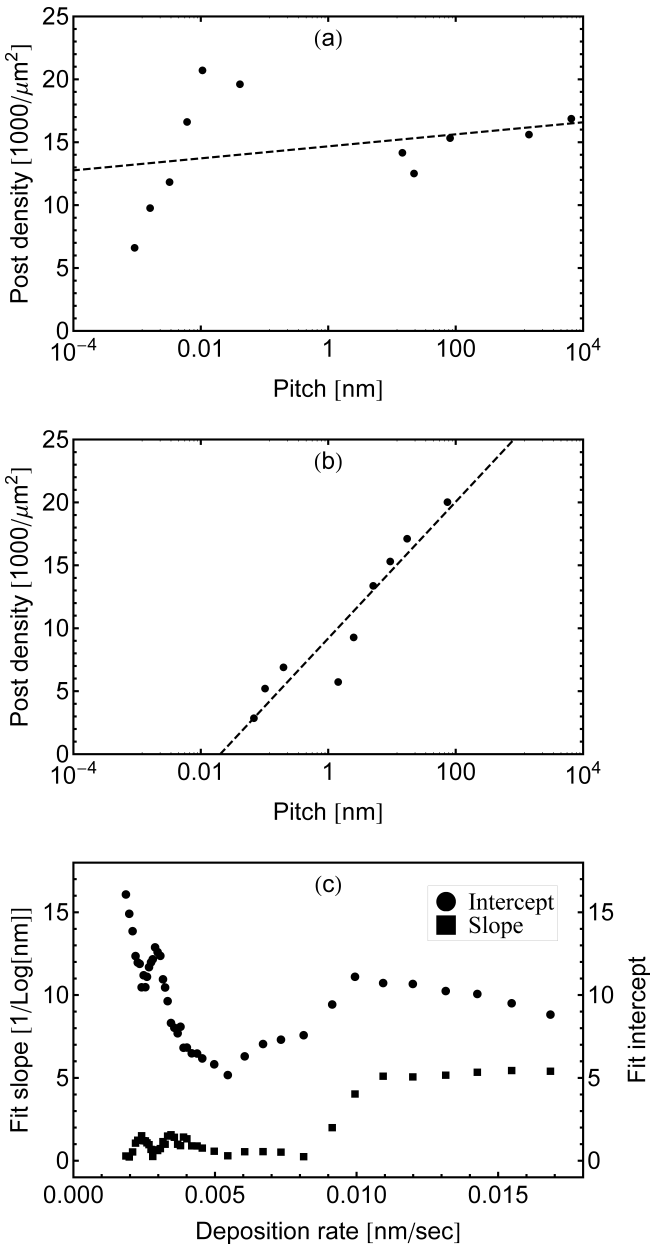

Figure 6.5: Scaling of the post density with the logarithm of pitch for low-deposition rates of $< 0.0025\,\mathrm{nm}\cdot\mathrm{s}^{-1}$ (a: $r = 0.29$, $p = 0.38$) and high-deposition rates of $> 0.01\,\mathrm{nm}\cdot\mathrm{s}^{-1}$ (b: $r = 0.94$, $p = 0.0001$). Intercept and slope parameters of a linear fit (dashed line) to the data windowed across the range of deposition rates (c). The low-surface diffusion regime at low-deposition rates $< 0.005\,\mathrm{nm}\cdot\mathrm{s}^{-1}$ is seen followed by transition region until crystal growth kinetics at higher deposition rates $> 0.01\,\mathrm{nm}\cdot\mathrm{s}^{-1}$ begin to shape the evolution of the nanorods.

the expected behaviour, the magnitude of exponential scaling parameter, $p' = 1.14$[ii], is much greater than expected from the limit of 2/3 from the KPZ theory [259]. Examination of Figure 6.3a reveals mushroom-like structures, suggesting that the value obtained from the fit properly describes our films. Similar structures have been reported for Al and Bi[43] and Cu [87, 252]. As we will see below, the films deposited here are highly textured, which may make the KPZ model inappropriate. The mushroom structures occur at higher pitch values and lead to post bifurcations; such effects may represent a limit in vertical post growth of crystalline materials. Further work will be required to evaluate these effects.

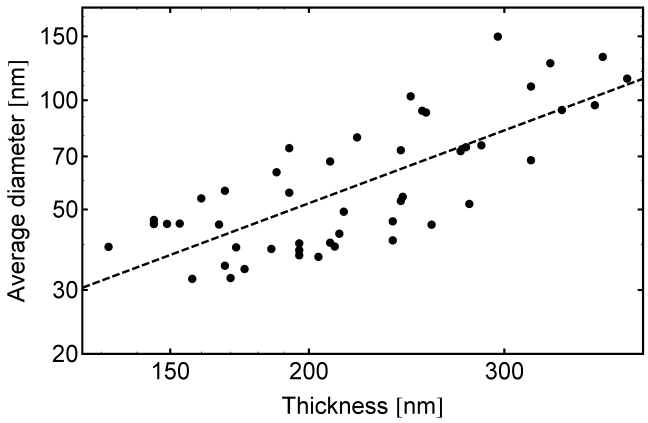

Figure 6.6: Scaling of post broadening with thickness for films with a deposition rate $< 0.005\,\mathrm{nm} \cdot \mathrm{s}^{-1}$ ($r = 0.76$, $p = 10^{-10}$). The fit is to the scaling relationship $w(h) = w_0 h^{p'}$ with $p' = 1.14$ (dashed line).

6.3.2 Crystallinity

Line profile analysis of the XRD patterns for all of the films show that the (002) peak at 34° is most prominent followed by the (004) peak at 73° (Figure 6.7). The large peak at 69° is due to diffraction from the (004) plane of the (100) silicon wafer. In nearly all of the patterns, all other diffraction peaks

[ii]The exponential scaling parameter is typically referred to as p in the literature, but should not be confused with the Pearson significance p used above.

are absent, indicating that the films are textured with c-axis growth parallel to the substrate normal.

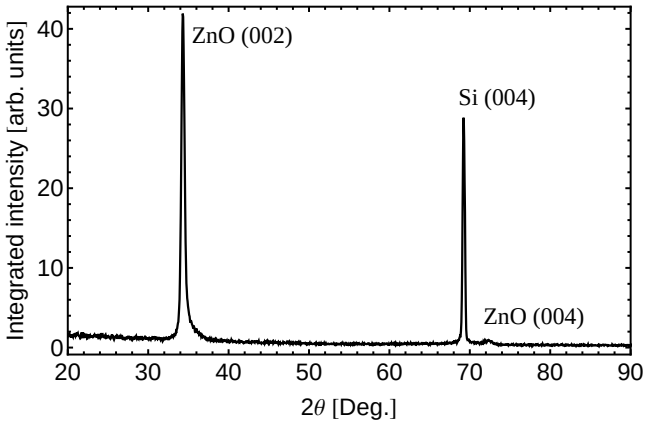

Figure 6.7: Typical XRD pattern of a ZnO thin film. Only the (002) and (004) peaks are present, indicating that the film is textured with the c-axis of wurtzite ZnO normal to the substrate.

Stereographic pole-figures of the (002), (101) and (102) planes of ZnO were taken at 2θ diffraction angles of 34.2°, 36.2°, and 47.5° respectively for one sample (Figure 6.8). The rotational symmetry of the patterns indicates isotropic orientation of the nanorods around the c-axis, which is parallel to the substrate normal. The measured angles between the (002)/(101) and (002)/(102) planes were found to be 61.5° and 42.7°, which are the expected values for a wurtzite ZnO crystal with lattice parameters of $a = b = 325$ pm and $c = 520$ pm[247].

Crystallite size was calculated with the Scherrer formula under the assumption of spherical monodisperse crystallites [170]. A measurement of the texture for each film was also produced by measuring the integral width of (002) diffraction arc in the χ direction. As expected, crystallite size increases with film thickness, but crystal orientation remains constant with the c-axis parallel to the substrate normal (Figure 6.9). The texture data demonstrates the preference of ZnO to grow with the c-axis normal to the substrate.

At high deposition rates, a strong positive correlation is seen between decreased crystal texture and pitch (Figure 6.10). One possible explanation for this is that the mushroom structures discussed above are similar to those ob-

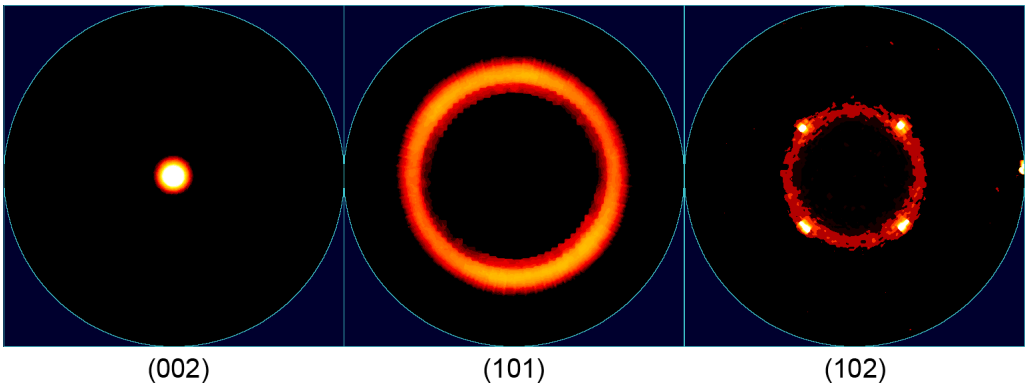

Figure 6.8: Stereographic pole figures for the (002), (101) and (102) planes of a ZnO thin film deposited at a film deposited at a pitch of 1.4 nm, deposition rate of 0.02 $\mathrm{nm} \cdot \mathrm{s}^{-1}$, and 118 mm throw distance. The four bright spots in the (102) pole figure are due to (220) plane of the (100) silicon substrate.

served in Cu [252]. In that work, the 'mushroom cap' is composed of smaller crystalline domains with different orientations (i.e., decreasing texture).

The data also suggest a trend between the crystal orientation and surface diffusion (Figure 6.11); increasing surface diffusion decreases the quality of the crystal texture in the film. This observation is consistent with early work on bulk sputtered ZnO thin films that identified a loss in crystal orientation above or below a temperature dependent deposition rate ($\sim 0.01\,\mathrm{nm} \cdot \mathrm{s}^{-1}$ for RF and DC sputtered films at temperatures less than 50 ℃) [260]. However, in other GLAD materials, an increase in surface diffusion was claimed to be responsible for increased texture [79] which further highlights the material dependence of film growth. The trend towards decreased crystal orientation for increased surface diffusion (decreased deposition rate) can be interpreted in the same way as the relationship between aspect ratio and the logarithm of pitch (i.e., as a deposition rate-dependent kinetic mechanism). Thus, as the surface diffusion increases, and the deposition rate decreases, growth kinetics are no longer able to play a significant role in the film's growth and crystal texture is degraded. Identifying the role of surface diffusion, deposition rate, and potential kinetic mechanisms in determining the crystal texture is a considerable task that is beyond the scope of this thesis. However, it is hoped that molecular dynamics simulations will be able to identify the

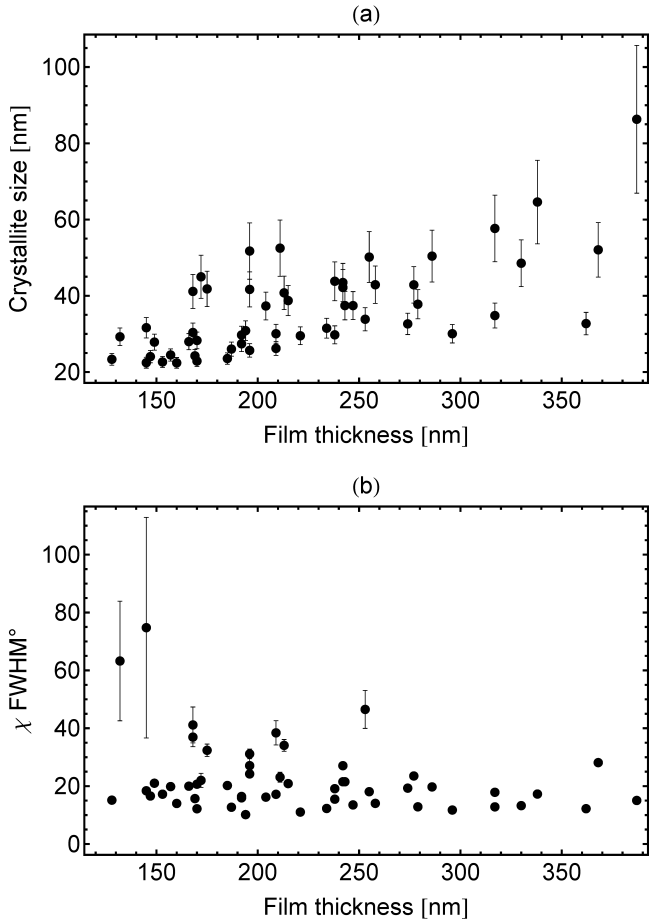

Figure 6.9: Data from the entire set of films demonstrating a trend towards increasing crystallite size with film thickness (a: $r = 0.68$, $p = 2 \cdot 10^{-8}$). Crystal texture (χ, smaller widths indicate larger texture) remains relatively constant regardless of film thickness (b). Error bars are produced from peak-fitting.

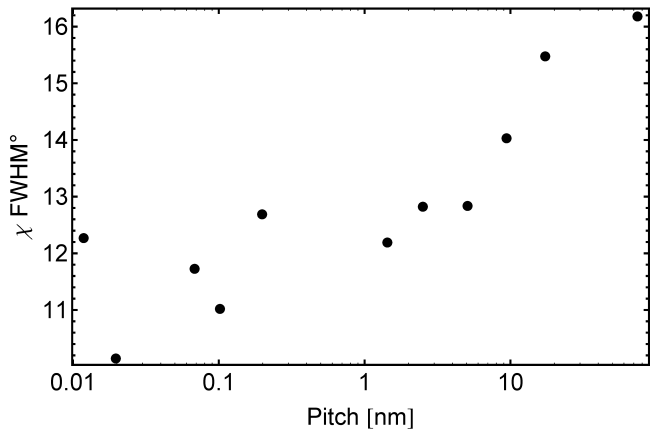

Figure 6.10: Measure of crystal texture and pitch for films deposited a high deposition rates $> 0.01\,\mathrm{nm} \cdot \mathrm{s}^{-1}$.

growth mechanisms.

The correlation between film texture and surface diffusion does suggest a means for controlling the texture independently of the film morphology. An increase in the deposition rate, or decrease in the substrate temperature, should both lead to an increased texture. However, caution should be employed when extrapolating beyond the range of process parameters explored here. In general, the influence of a material's preferred crystallinity will have to be evaluated on a case by case basis until a greater experimental data set and theoretical understanding can be developed.

6.4 Conclusion

A survey of the pitch and throw distance parameter space has allowed us to identify optimal growth conditions for single-crystalline, texture nanorod ZnO films. The relationship between post aspect ratio and pitch changes with deposition rate and can be interpreted as a transition between geometric shadowing, or GLAD growth, at low deposition rates of $< 0.005\,\mathrm{nm} \cdot \mathrm{s}^{-1}$ and growth kinetics activated at higher deposition rates $> 0.01\,\mathrm{nm} \cdot \mathrm{s}^{-1}$.

Nanorod growth is possible in both the geometric shadowing regime and the growth kinetics regime (Figure 6.3), but the nanorods grown at high

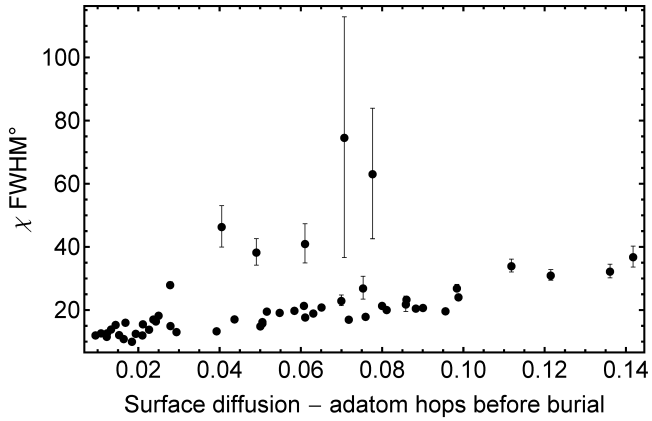

Figure 6.11: Measure of crystal texture with reference to the c-axis parallel to the substrate normal as a function of adatom surface diffusion. Crystal texture (χ) is based on the width of the (002) peak in the χ direction (smaller widths indicate larger texture); error bars are produced from peak fitting.

deposition rates ($> 0.01\,\mathrm{nm \cdot s^{-1}}$) are more isolated. The scaling of the aspect ratio with pitch is different for the two regimes (Figure 6.4). In both cases, pitch values between 1 nm and 100 nm produce isolated nanorod films, with a trend towards an increase in nanorod aspect ratio at larger values of pitch for films deposited at rates $> 0.01\,\mathrm{nm \cdot s^{-1}}$. Above and below this range, the nanorods broaden and are no longer completely isolated through the entire film thickness. Deposition pitch was also shown to strongly influence the texture and morphology of Fe nanocolumns in Chapter 3. Deposition rate and pitch (rotation rate) appear to play a crucial role in establishing and controlling crystal growth in GLAD films.

While all of the ZnO films exhibit crystal texture, films deposited under conditions that increase burial rate tend to have stronger texture. The data suggests that film texture and morphology can be independently controlled to some extent with substrate heating. This may provide a mechanism for further investigation of the relationship between growth kinetics and self-shadowing in material systems that exhibit crystallinity with GLAD.

Process studies, such as this work, are important in constraining the limits of what can be achieved with GLAD. This is necessary to define the achievable film characteristics, as GLAD moves towards applications and

manufacturing. For instance, this study helped define the range of morphologies readily achievable with sputtered-GLAD ZnO films. While we had originally hoped to fabricate nanorods with aspect-ratios of 100:1 for piezoelectric mechanical energy-scavenging electric generation devices, it became clear that such structures were not achievable. This knowledge motivated the pivot to the iron pyrite work discussed in Chapters 3, 4 and 5. While we left ZnO behind, the importance of pitch and flux engineering techniques for controlling morphology and microstructure in GLAD informed those later works.

Chapter 7

Conclusions

The goal of this of thesis was to develop new techniques for microstructural control of polycrystalline GLAD films while simultaneously insuring functional properties of the materials were maintained. To achieve this, we developed flux engineering techniques for controlling the microstructure, morphology and texture in Fe and ZnO material systems. These techniques were then applied to the development of iron pyrite films via sulfur annealing, and several tests were made to evaluate the functional performance of the iron pyrite for application to photovoltaics.

In Chapter 3, the low-pitch conditions required to encourage crystalline growth in Fe nanocolumns was shown. Crystalline nanocolumns have a tetrahedral apex, and thus a 3-fold symmetry in the substrate plane. We have used the symmetry of the nanocolumns to demonstrate a new motion algorithm to induce biaxial texture. By matching the azimuthal symmetry of the flux to that of the films, we are able to change the competitive dynamics during film growth to arrive at a biaxially textured, morphologically oriented nanocolumn array via an evolutionary selection process. This technique is generalizable to other crystalline materials system, and therefore provides a new method to induce biaxial texture in GLAD.

The polycrystalline Fe nanocolumns were then used as a template for the sulfurization of iron pyrite thin films in Chapter 4 and sputtered Fe nanocolumns were similarly used in Chapter 5. Annealing work in GLAD often is focused on improving the stoichiometry of a composite film, as in

the case of titanium dioxide or silicon dioxide films for optical applications, or recrystallizing a different crystal phase of the same material such as rutile or anatase titanium dioxide [4]. In the sulfurization work, the Fe precursors were used as templates and source material for the recrystallization of iron pyrite under sulfur annealing. Simultaneous composition, morphological, and crystal phase changes occur in this process. We are able to control the microstructure of the resulting iron pyrite films without changes in the annealing chemistry. This result is encouraging for other applications where GLAD templates could be used to develop other crystalline composite materials.

The voids introduced by the inter-column spacing in the Fe precursors reduce the stress buildup during conversion from Fe to FeS_2 and thereby induce the observed microstructure changes in the pyrite films. We have designed the Fe templates to relax the phase transformation stress during sulfurization. Although, we made attempts to measure the stress within the films by wafer bending and x-ray diffraction line profile analysis, we found it difficult to quantify these effects as film stresses were often relaxed due to cracking or delamination of the pyrite. It is likely that an in situ characterization technique such as x-ray diffraction will be required to properly characterize the stress build up and relaxation during sulfurization. The role of stresses during recrystallization is underdeveloped in general [221]. Thus, any future contributions in this area should find interest in the general materials science community.

The FeS_2 films were characterized to judge their suitability in photovoltaic applications. Beyond the typical analysis of the composition, crystal phases, optical properties and electrical properties of the pyrite films. We also measured carrier lifetime in Chapter 4 in collaboration with Dr. Frank Hegmann's group (Department of Physics) and attempted to determine an upper-bound for the strength of the charge-transfer process between a conjugated polymer and our iron pyrite films in Chapter 5 in collaboration with Dr. Jillian Buriak's group (Department of Chemistry) and Dr. Al Meldrum's group (Department of Physics). These experiments indicate that serious challenges around carrier lifetime and surface quality/preparation remain before our iron pyrite films would be able to provide efficiencies above a few percent

in a photovoltaic device. Although, significant strides were made in improving the original pyrite fabrication process between Chapter 5 and Chapter 4[i] we did not have an opportunity to explore improvements in charge-transfer in Chapter 4 as our main collaborator, Brian Worfolk, had graduated and moved on.

Finally[ii], we performed a systematic study of deposition conditions required to increase the aspect ratio of GLAD sputtered nanocolumns in Chapter 6. Our interest in the large aspect ratios was motivated by the interested in ZnO nanocolumns for piezoelectric energy generation and photovoltaics. We found that both pitch and deposition rate play a crucial role in determining the column structure. However, the nanowire-like aspect ratios of 1000:1 required for piezoelectric generation are well beyond what we were able to produce. Therefore, ZnO GLAD nanocolumns are better suited for other applications that require a roughened surface or low-aspect ratio columnar structures. While we left ZnO behind, the importance of pitch and flux engineering techniques for controlling morphology and microstructure in GLAD informed later work on Fe and FeS_2.

This thesis demonstrates the utility of crystalline microstructural control methods in GLAD. Much work remains to be done to further understand the relevant physics and the role of substrate motion in the development of crystallinity and texture evolution. Future studies will benefit from simulations that can accurately model the experimental work. Current models are too general to provide useful predictions of film growth. As mentioned above, understanding of recrystallization dynamics, such as those that appear present in sulfurization, are ripe for future study as this field is both experimentally and theoretically challenging. An opportunity for GLAD to assist experimentally as templates for stress-relaxation during recrystallization may be present.

Over the course of this thesis, additional developments in controlling biaxial texture have been made and nanowire vapor-liquid-solid growth has been merged with GLAD. Flux engineering developed here has already been demonstrated to assist in the alignment and texture development of branched

[i] Chronologically Chapter 5 preceded Chapter 4

[ii] Chronologically, this was the first work done for the thesis.

nanowires [102]. Continued or improved consideration of the benefits of engineering substrate rotations to compliment or enhance growth of nanoscale materials should continue to increase the possible nanoscale structures, and hopefully enable new applications.

Bibliography

[1] Multigate device, 2013.

[2] John A Thornton. High Rate Thick Film Growth. *Annual Review of Materials Science*, 7(1):239–260, August 1977.

[3] J. M. E. Harper. Microstructure control in semiconductor metallization. *Journal of Vacuum Science & Technology B: Microelectronics and Nanometer Structures*, 15(4):763, July 1997.

[4] Michael Thomas Taschuk, Matthew M. Hawkeye, and Michael Julian Brett. Glancing Angle Deposition. In *Handbook of Deposition Technologies for Films and Coatings*. Elsevier, 2010.

[5] John J. Steele and Michael Julian Brett. Nanostructure engineering in porous columnar thin films: recent advances. *Journal of Materials Science: Materials in Electronics*, 18(4):367–379, October 2006.

[6] Martin F. Schubert, J.-Q. Xi, Jong Kyu Kim, and E. Fred Schubert. Distributed Bragg reflector consisting of high- and low-refractive-index thin film layers made of the same material. *Applied Physics Letters*, 90(14):141115, 2007.

[7] Nobuyuki Otsu. A Threshold Selection Method from Gray-Level Histograms. *IEEE Transactions on Systems, Man, and Cybernetics*, 9(1):62–66, 1979.

[8] Ryan T. Tucker, Allan L. Beaudry, Joshua Michael LaForge, Michael Thomas Taschuk, and Michael Julian Brett. A little ribbing: Flux starvation engineering for rippled indium tin oxide nanotree branches. *Applied Physics Letters*, 101(19):193101, 2012.

[9] L Chen, Toh-Ming Lu, and G-C Wang. Biaxially textured Mo films with diverse morphologies by substrate-flipping rotation. *Nanotechnology*, 22(50):505701, December 2011.

[10] Pietro P. Altermatt, Tobias Kiesewetter, Klaus Ellmer, and Helmut Tributsch. Specifying targets of future research in photovoltaic devices containing pyrite (FeS2) by numerical modelling. *Solar Energy Materials and Solar Cells*, 71(2):181–195, February 2002.

[11] I.J. Ferrer, J.R. Ares, and C.R. Sánchez. A note on the Hall mobility and carrier concentration in pyrite thin films. *Solar Energy Materials and Solar Cells*, 76(2):183–188, March 2003.

[12] Yong Xu and Martin A.A. Schoonen. The absolute energy positions of conduction and valence bands of selected semiconducting minerals. *American Mineralogist*, 85:543–556, 2000.

[13] Nicolas Allard, Réda Badrou Aïch, David Gendron, Pierre-Luc T. Boudreault, Christian Tessier, Salima Alem, Shing-Chi Tse, Ye Tao, and Mario Leclerc. Germafluorenes: New Heterocycles for Plastic Electronics. *Macromolecules*, 43(5):2328–2333, March 2010.

[14] Tyler L Cocker. *Exploring conductivity in nanomaterials with terahertz pulses*. PhD thesis, University of Alberta, 2012.

[15] Vaidyanathan Subramanian. Multiple Gate Field-Effect Transistors for Future CMOS Technologies. *IETE Technical Review*, 27(6):446, 2010.

[16] Matthew M. Hawkeye and Michael Julian Brett. Optimized Colorimetric Photonic-Crystal Humidity Sensor Fabricated Using Glancing Angle Deposition. *Advanced Functional Materials*, 21:3652–3658, August 2011.

[17] C. B. Murray, C. R. Kagan, and M. G. Bawendi. Synthesis And Characterization Of Monodisperse Nanocrystals And Close-Packed Nanocrystal Assemblies. *Annual Review of Materials Science*, 30(1):545–610, August 2000.

[18] John H. Davies. *The Physics of Low-Dimensional Semiconductors: An Introduction*. Cambridge University Press, Cambridge, UK, 1997.

[19] Milton Ohring. *Materials Science of Thin Films*. Academic Press, San Diego, CA, 2 edition.

[20] Steven M George. Atomic layer deposition: an overview. *Chemical reviews*, 110(1):111–31, January 2010.

[21] Douglas B. Chrisey and Graham K. Hubler, editors. *Pulsed Laser Deposition of Thin Films*. Wiley-Interscience, 1994.

[22] Gabriela Popa, Fouzia Boulmedais, Peng Zhao, Joseph Hemmerlé, Loïc Vidal, Eric Mathieu, Olivier Félix, Pierre Schaaf, Gero Decher, and Jean-Claude Voegel. Nanoscale precipitation coating: the deposition of inorganic films through step-by-step spray-assembly. *ACS nano*, 4(8):4792–8, August 2010.

[23] Larry L. Hench and Jon K. West. The sol-gel process. *Chemical Reviews*, 90(1):33–72, January 1990.

[24] Mordechay Schlesinger and Milan Paunovic. *Modern Electroplating Volume 55 of The ECS Series of Texts and Monographs*. John Wiley & Sons, Inc, 2011.

[25] James Puthussery, Sean Seefeld, Nicholas Berry, Markelle Gibbs, and Matt Law. Colloidal iron pyrite (FeS2) nanocrystal inks for thin-film photovoltaics. *Journal of the American Chemical Society*, 133(4):716–9, February 2011.

[26] L Abelmann and C Lodder. Oblique evaporation and surface diffusion. *Thin Solid Films*, 305(1-2):1–21, August 1997.

[27] L.B. Freund and S. Suresh. *Thin Film Materials: Stress, Defect Formation and Surface Evolution*. Cambridge University Press, Cambridge, UK, 2003.

[28] Robert W. Balluffi, Samuel M. Allen, and W. Craig Carter. *Kinetics of Materials*. John Wiley and Sons, 2005.

[29] Matthew M. Hawkeye and Michael Julian Brett. Narrow bandpass optical filters fabricated with one-dimensionally periodic inhomogeneous thin films. *Journal of Applied Physics*, 100(4):044322, 2006.

[30] Matthew M. Hawkeye, Robert Joseph, Jeremy C. Sit, and Michael Julian Brett. Coupled defects in one-dimensional photonic crystal films fabricated with glancing angle deposition. *Optics express*, 18(12):13220–6, June 2010.

[31] David A Rider, Ryan T. Tucker, Brian J Worfolk, Kathleen M. Krause, Abeed Lalany, Michael Julian Brett, Jillian M. Buriak, and Kenneth D. Harris. Indium tin oxide nanopillar electrodes in polymer/fullerene solar cells. *Nanotechnology*, 22(8):085706, February 2011.

[32] John J. Steele, Glen a. Fitzpatrick, and Michael Julian Brett. Capacitive Humidity Sensors With High Sensitivity and Subsecond Response Times. *IEEE Sensors Journal*, 7(6):955–956, June 2007.

[33] Michael Thomas Taschuk, John J. Steele, Andy C. van Popta, and Michael Julian Brett. Photocatalytic regeneration of interdigitated capacitor relative humidity sensors fabricated by glancing angle deposition. *Sensors and Actuators B: Chemical*, 134(2):666–671, September 2008.

[34] John J. Steele, J.P. Gospodyn, Jeremy C. Sit, and Michael Julian Brett. Impact of morphology on high-speed humidity sensor performance. *IEEE Sensors Journal*, 6(1):24–27, February 2006.

[35] Michael Thomas Taschuk, Jason B. Sorge, John J. Steele, and Michael Julian Brett. Ion-Beam Assisted Glancing Angle Deposition for Relative Humidity Sensors. *IEEE Sensors Journal*, 8(9):1521–1522, September 2008.

[36] S. N. Piramanayagam. Perpendicular recording media for hard disk drives. *Journal of Applied Physics*, 102(1):011301, 2007.

[37] G Larrieu and X-L Han. Vertical nanowire array-based field effect transistors for ultimate scaling. *Nanoscale*, 5(6):2437–41, March 2013.

[38] L. Britnell, R. V. Gorbachev, A. K. Geim, L. A. Ponomarenko, A. Mishchenko, M. T. Greenaway, T. M. Fromhold, K. S. Novoselov, and L. Eaves. Resonant tunnelling and negative differential conductance in graphene transistors. *Nature Communications*, 4:1794, April 2013.

[39] Phillip M. Wu, Lars Samuelson, and Heiner Linke. Toward 3D Integration of 1D Conductors: Junctions of InAs Nanowires. *Journal of Nanomaterials*, 2011(111):1–5, 2011.

[40] DB Suyatin, Jie Sun, Andreas Fuhrer, and Daniel Wallin. Electrical properties of self-assembled branched InAs nanowire junctions. *Nano letters*, pages 0–4, 2008.

[41] Matthew M. Hawkeye and Michael Julian Brett. Glancing angle deposition: Fabrication, properties, and applications of micro- and nanostructured thin films. *Journal of Vacuum Science & Technology A: Vacuum, Surfaces, and Films*, 25(5):1317–1335, 2007.

[42] Jeremy C. Sit, D. Vick, Kevin Robbie, and Michael Julian Brett. Thin film microstructure control using glancing angle deposition by sputtering. *J. Mater. Res*, 14(4):1197–1199, 1999.

[43] B. Dick, Michael Julian Brett, and T. J. Smy. Investigation of substrate rotation at glancing incidence on thin-film morphology. *Journal of Vacuum Science & Technology B: Microelectronics and Nanometer Structures*, 21(6):2569, 2003.

[44] Ravi K Joshi and Jörg J Schneider. Assembly of one dimensional inorganic nanostructures into functional 2D and 3D architectures. Synthesis, arrangement and functionality. *Chemical Society reviews*, 41(15):5285–312, August 2012.

[45] Y. Xia, P. Yang, Y. Sun, Y. Wu, B. Mayers, B. Gates, Y. Yin, F. Kim, and H. Yan. One-Dimensional Nanostructures: Synthesis, Characterization, and Applications. *Advanced Materials*, 15(5):353–389, March 2003.

[46] H Masuda and K Fukuda. Ordered metal nanohole arrays made by a two-step replication of honeycomb structures of anodic alumina. *Science (New York, N.Y.)*, 268(5216):1466–8, June 1995.

[47] Zheng Miao, Dongsheng Xu, Jianhua Ouyang, Guolin Guo, Xinsheng Zhao, and Youqi Tang. Electrochemically Induced Sol−Gel Preparation of Single-Crystalline TiO 2 Nanowires. *Nano Letters*, 2(7):717–720, July 2002.

[48] Erik Garnett and Peidong Yang. Light trapping in silicon nanowire solar cells. *Nano letters*, 10(3):1082–7, March 2010.

[49] Brent a. Wacaser, Kimberly a. Dick, Jonas Johansson, Magnus T. Borgström, Knut Deppert, and Lars Samuelson. Preferential Interface Nucleation: An Expansion of the VLS Growth Mechanism for Nanowires. *Advanced Materials*, 21(2):153–165, January 2009.

[50] F. N. Borovik and S. P. Fisenko. Kinetics of nanowhisker growth via the vapor-liquid-solid mechanism. *Technical Physics Letters*, 33(2):151–153, February 2007.

[51] P. Cheyssac, M. Sacilotti, and G. Patriarche. Vapor-liquid-solid mechanisms: Challenges for nanosized quantum cluster/dot/wire materials. *Journal of Applied Physics*, 100(4):044315, 2006.

[52] Erik T Thostenson, Zhifeng Ren, and Tsu-Wei Chou. Advances in the science and technology of carbon nanotubes and their composites: a review. *Composites Science and Technology*, 61(13):1899–1912, October 2001.

[53] Song Jin, Matthew J. Bierman, and Stephen a. Morin. A New Twist on Nanowire Formation: Screw-Dislocation-Driven Growth of Nanowires and Nanotubes. *The Journal of Physical Chemistry Letters*, 1(9):1472–1480, May 2010.

[54] Jonathan E Allen, Eric R Hemesath, Daniel E Perea, Jessica L Lensch-Falk, Z Y Li, Feng Yin, Mhairi H Gass, Peng Wang, Andrew L Bleloch, Richard E Palmer, and Lincoln J Lauhon. High-resolution detection of

Au catalyst atoms in Si nanowires. *Nature nanotechnology*, 3(3):168–73, March 2008.

[55] Daniel E Perea, Eric R Hemesath, Edwin J Schwalbach, Jessica L Lensch-Falk, Peter W Voorhees, and Lincoln J Lauhon. Direct measurement of dopant distribution in an individual vapour-liquid-solid nanowire. *Nature nanotechnology*, 4(5):315–9, May 2009.

[56] Bozhi Tian, Ping Xie, Thomas J Kempa, David C Bell, and Charles M Lieber. Single-crystalline kinked semiconductor nanowire superstructures. *Nature nanotechnology*, 4(12):824–9, December 2009.

[57] CM Lieber. Nanoscale science and technology: building a big future from small things. *Mrs Bulletin*, (July):486–491, 2003.

[58] Michael Julian Brett, Kevin Robbie, and Akhlesh Lakhtakia. Chiral sculptured thin films. *Nature*, 384(6610):616–616, December 1996.

[59] Kevin Robbie and Michael Julian Brett. Sculptured thin films and glancing angle deposition: Growth mechanics and applications. *Journal of Vacuum Science & Technology A: Vacuum, Surfaces, and Films*, 15(3):1460–1465, 1997.

[60] Kevin Robbie, Gisia Beydaghyan, Tim Brown, Cory Dean, Jonathan Adams, and Cristina Buzea. Ultrahigh vacuum glancing angle deposition system for thin films with controlled three-dimensional nanoscale structure. *Review of Scientific Instruments*, 75(4):1089, 2004.

[61] Kenneth D. Harris, Andy C. van Popta, Jeremy C. Sit, Dirk J. Broer, and Michael Julian Brett. A Birefringent and Transparent Electrical Conductor. *Advanced Functional Materials*, 18(15):2147–2153, August 2008.

[62] Nicholas G. Wakefield, Jason B. Sorge, Michael Thomas Taschuk, Louis W Bezuidenhout, Michael Julian Brett, and Jeremy C. Sit. Control of the principal refractive indices in biaxial metal oxide films. *Journal of the Optical Society of America A*, 28(9):1830–1840, 2011.

[63] Mark Alan Summers and Michael Julian Brett. Optimization of periodic column growth in glancing angle deposition for photonic crystal fabrication. *Nanotechnology*, 19(41):415203, October 2008.

[64] J D Driskell, A G Seto, L P Jones, S Jokela, R A Dluhy, Y-P Zhao, and R A Tripp. Rapid microRNA (miRNA) detection and classification via surface-enhanced Raman spectroscopy (SERS). *Biosensors & bioelectronics*, 24(4):923–8, December 2008.

[65] Daniel P Smetaniuk, Michael Thomas Taschuk, and Michael Julian Brett. Photocatalytic Titanium Dioxide Nanostructures for Self-Regenerating Relative Humidity Sensors. *Sensors (Peterborough, NH)*, 11(8):1713–1719, 2011.

[66] Martin R. Kupsta, Michael Thomas Taschuk, Michael Julian Brett, and Jeremy C. Sit. Reactive Ion Etching of Columnar Nanostructured TiO2 Thin Films for Modified Relative Humidity Sensor Response Time. *IEEE Sensors Journal*, 9(12):1979–1986, December 2009.

[67] S. V. Kesapragada, P Victor, O Nalamasu, and Daniel Gall. Nanospring pressure sensors grown by glancing angle deposition. *Nano letters*, 6(4):854–7, April 2006.

[68] E Schubert, J Fahlteich, T Hoche, G Wagner, and B Rauschenbach. Chiral silicon nanostructures. *Nuclear Instruments and Methods in Physics Research Section B: Beam Interactions with Materials and Atoms*, 244(1):40–44, March 2006.

[69] Joachim Krug. Origins of scale invariance in growth processes. *Advances in Physics*, 46(2):139–282, April 1997.

[70] Paul Meakin. *Fractals, scaling and growth far from equilibrium*, volume 5 of *Cambridge nonlinear science series*. Cambridge University Press, 1998.

[71] Tansel Karabacak, G.-C. Wang, and Toh-Ming Lu. Physical self-assembly and the nucleation of three-dimensional nanostructures by

oblique angle deposition. *Journal of Vacuum Science & Technology A: Vacuum, Surfaces, and Films*, 22(4):1778, 2004.

[72] Julianne D Halley and David A Winkler. Consistent concepts of self-organization and self-assembly. *Complexity*, 14(2):10–17, November 2008.

[73] Tansel Karabacak, J. Singh, Y.-P. Zhao, G.-C. Wang, and Toh-Ming Lu. Scaling during shadowing growth of isolated nanocolumns. *Physical Review B*, 68(12):125408, September 2003.

[74] Mark Alan Summers, K. Tabunshchyk, Andriy Kovalenko, and Michael Julian Brett. Fabrication of 2D–3D photonic crystal heterostructures by glancing angle deposition. *Photonics and Nanostructures - Fundamentals and Applications*, 7(2):76–84, May 2009.

[75] Mark Alan Summers. *Glancing angle depositied periodic thin films*. PhD thesis, 2009.

[76] Pasquale Calabrese and Pierre Le Doussal. Exact Solution for the Kardar-Parisi-Zhang Equation with Flat Initial Conditions. *Physical Review Letters*, 106(25):250603, June 2011.

[77] M.O. Jensen and Michael Julian Brett. Porosity engineering in glancing angle deposition thin films. *Applied Physics A*, 80(4):763–768, June 2005.

[78] B. Dick, Michael Julian Brett, T. J. Smy, M. R. Freeman, M. Malac, and Ray F. Egerton. Periodic magnetic microstructures by glancing angle deposition. *Journal of Vacuum Science & Technology A: Vacuum, Surfaces, and Films*, 18(4):1838, 2000.

[79] Marek Malac and Ray F. Egerton. Observations of the microscopic growth mechanism of pillars and helices formed by glancing-angle thin-film deposition. *Journal of Vacuum Science & Technology A: Vacuum, Surfaces, and Films*, 19(1):158, 2001.

[80] Norio Yamaguchi, Kunihiko Wada, Kazushige Kimura, and Hideaki Matsubara. Microstructure modification of yttria-stabilized zirconia

layers prepared by EB-PVD. *Journal of the Ceramic Society of Japan*, 111(12):883–889, 2003.

[81] Joshua Michael LaForge, Michael Thomas Taschuk, and Michael Julian Brett. Glancing angle deposition of crystalline zinc oxide nanorods. *Thin Solid Films*, 519(11):3530–3537, March 2011.

[82] H. Alouach and G. J. Mankey. Texture orientation of glancing angle deposited copper nanowire arrays. *Journal of Vacuum Science & Technology A: Vacuum, Surfaces, and Films*, 22(4):1379, 2004.

[83] P. Morrow, F. Tang, Tansel Karabacak, P.-I. Wang, D.-X Ye, G.-C. Wang, and Toh-Ming Lu. Texture of Ru columns grown by oblique angle sputter deposition. *Journal of Vacuum Science & Technology A: Vacuum, Surfaces, and Films*, 24(2):235, 2006.

[84] Joshua Morgan Arthur Siewert, Joshua Michael LaForge, Michael Thomas Taschuk, and Michael Julian Brett. Disassembling glancing angle deposited films for high-throughput, single-post growth scaling measurements. *Microscopy and microanalysis : the official journal of Microscopy Society of America, Microbeam Analysis Society, Microscopical Society of Canada*, 18(5):1135–42, October 2012.

[85] H-F Li, A K Kar, T. Parker, G-C Wang, and Toh-Ming Lu. The morphology and texture of Cu nanorod films grown by controlling the directional flux in physical vapor deposition. *Nanotechnology*, 19(33):335708, August 2008.

[86] F. Tang, C. Gaire, D.-X. Ye, Tansel Karabacak, Toh-Ming Lu, and G.-C. Wang. AFM, SEM and in situ RHEED study of Cu texture evolution on amorphous carbon by oblique angle vapor deposition. *Physical Review B*, 72(3):1–8, July 2005.

[87] Jian Wang, Hanchen Huang, S. V. Kesapragada, and Daniel Gall. Growth of Y-shaped nanorods through physical vapor deposition. *Nano letters*, 5(12):2505–8, December 2005.

[88] W K Choi, L Li, H G Chew, and F Zheng. Synthesis and structural characterization of germanium nanowires from glancing angle deposition. *Nanotechnology*, 18(38):385302, September 2007.

[89] Yuping He, Yiping Zhao, and Jinsong Wu. The effect of Ti doping on the growth of Mg nanostructures by oblique angle codeposition. *Applied Physics Letters*, 92(6):063107, 2008.

[90] F. Tang, Tansel Karabacak, P. Morrow, C. Gaire, G.-C. Wang, and Toh-Ming Lu. Texture evolution during shadowing growth of isolated Ru columns. *Physical Review B*, 72(16):1–6, October 2005.

[91] Wang Huan-Hua, Shi Yi-Jian, William Chu, and Yigal Blum. Strong Surface Diffusion Mediated Glancing-Angle Deposition: Growth, Recrystallization and Reorientation of Tin Nanorods. *Chinese Physics Letters*, 25(1):234–237, January 2008.

[92] Tansel Karabacak, Anupama Mallikarjunan, Jitendra P. Singh, Dexian Ye, Gwo-Ching Wang, and Toh-Ming Lu. Beta-Phase Tungsten Nanorod Formation By Oblique-Angle Sputter Deposition. *Applied Physics Letters*, 83(15):3096, 2003.

[93] R Krishnan, T. Parker, S. Lee, and Toh-Ming Lu. The formation of vertically aligned biaxial tungsten nanorods using a novel shadowing growth technique. *Nanotechnology*, 20(46):465609, November 2009.

[94] R Krishnan, Y Liu, C. Gaire, L Chen, G-C Wang, and Toh-Ming Lu. Texture evolution of vertically aligned biaxial tungsten nanorods using RHEED surface pole figure technique. *Nanotechnology*, 21(32):325704, August 2010.

[95] H.-F. Li, T. Parker, F. Tang, G.-C. Wang, Toh-Ming Lu, and S. Lee. Biaxially oriented CaF2 films on amorphous substrates. *Journal of Crystal Growth*, 310(15):3610–3614, July 2008.

[96] J. R. Frederick and Daniel Gall. Surface morphological evolution of epitaxial CrN(001) layers. *Journal of Applied Physics*, 98(5):054906, 2005.

[97] Yuping He, Zhongyue Zhang, Chris Hoffmann, and Yiping Zhao. Embedding Ag Nanoparticles into MgF2 Nanorod Arrays. *Advanced Functional Materials*, 18(11):1676–1684, June 2008.

[98] Y Xu, C H Lei, B Ma, H Evans, H Efstathiadis, R Manisha, M Massey, U. Balachandran, and R Bhattacharya. Growth of textured MgO through e-beam evaporation and inclined substrate deposition. *Superconductor Science and Technology*, 19(8):835–843, August 2006.

[99] R.E. Koritala, B.L. Fisher, A.R. Markowitz, R.A. Erck, S.E. Dorris, D.J. Miller, and U. Balachandran. Biaxially aligned template films fabricated by inclined-substrate deposition for YBCO-coated conductor applications. *IEEE Transactions on Appiled Superconductivity*, 13(2):2695–2698, June 2003.

[100] Stijn Mahieu, Pieter Ghekiere, Diederik Depla, Roger De Gryse, Oleg I. Lebedev, and Gustaf Van Tendeloo. Mechanism of in-plane alignment in magnetron sputtered biaxially aligned yttria-stabilized zirconia. *Journal of Crystal Growth*, 290(1):272–279, April 2006.

[101] R Teki, T. Parker, H Li, N Koratkar, Toh-Ming Lu, and S. Lee. Low temperature synthesis of single crystalline ZnO nanorods by oblique angle deposition. *Thin Solid Films*, 516(15):4993–4996, June 2008.

[102] Allan L. Beaudry, Ryan T. Tucker, Joshua Michael LaForge, Michael Thomas Taschuk, and Michael Julian Brett. Indium tin oxide nanowhisker morphology control by vapour–liquid–solid glancing angle deposition. *Nanotechnology*, 23(10):105608, March 2012.

[103] Motofumi Suzuki, Kenji Hamachi, Hideki Hara, Kaoru Nakajima, Kenji Kimura, Chia-Wei Hsu, and Li-Jen Chou. Vapor-liquid-solid growth of Ge nanowhiskers enhanced by high-temperature glancing angle deposition. *Applied Physics Letters*, 99(22):223107, 2011.

[104] Arif S. Alagoz and Tansel Karabacak. Fabrication of Crystalline Semiconductor Nanowires by Vapor-Liquid-Solid Glancing Angle Deposition (VLS-GLAD) Technique. *MRS Proceedings*, 1350(Cvd), June 2011.

[105] RS Wagner and WC Ellis. Vapor-Liquid-Solid Mechanism of Single Crystal Growth. *Applied Physics Letters*, 4:89, 1964.

[106] Allan L. Beaudry, Joshua Michael LaForge, Ryan T. Tucker, Peng Li, Michael Thomas Taschuk, and Michael Julian Brett. Flux Engineering for Indium Tin Oxide Nanotree Crystal Alignment and Height-Dependent Branch Orientation. *Crystal Growth & Design*, 13(1):212–219, January 2013.

[107] D. M. Evans and H. Wilman. Crystal growth and orientation in deposits condensed from the vapour. *Acta Crystallographica*, 5(6):731–738, November 1952.

[108] D.J. Srolovitz, C.C. Battaile, X Li, and J.E. Butler. Simulation of faceted film growth in two-dimensions: microstructure, morphology and texture. *Acta Materialia*, 47(7):2269–2281, May 1999.

[109] A. van der Drift. Evolutionary selection, a principle governing growth orientation in vapour-deposited layers. *Philips Research Reports*, 22:267, 1967.

[110] M.P. Chudzik, R.E. Koritala, L.P. Luo, D.J. Miller, U. Balachandran, and C.R. Kannewurf. Mechanism and processing dependence of biaxial texture development in magnesium oxide thin films grown by inclined-substrate deposition. *IEEE Transactions on Appiled Superconductivity*, 11(1):3469–3472, March 2001.

[111] O. P. Karpenko, J. C. Bilello, and S. M. Yalisove. Growth anisotropy and self-shadowing: A model for the development of in-plane texture during polycrystalline thin-film growth. *Journal of Applied Physics*, 82(3):1397, 1997.

[112] Liang Li, Xiaosheng Fang, Han Guan Chew, Fei Zheng, Tze Haw Liew, Xijin Xu, Yunxia Zhang, Shusheng Pan, Guanghai Li, and Lide Zhang. Crystallinity-Controlled Germanium Nanowire Arrays: Potential Field Emitters. *Advanced Functional Materials*, 18(7):1080–1088, 2008.

[113] Christopher G. Johansen, Hanchen Huang, and Toh-Ming Lu. Effects of three-dimensional Ehrlich-Schwoebel barrier on texture selection during Cu nanorod growth. *Applied Physics Letters*, 91(12):121914, 2007.

[114] James Gospodyn, Michael Thomas Taschuk, Peter C. P. Hrudey, Y. Y. Tsui, R. Fedosejevs, Michael Julian Brett, and Jeremy C. Sit. Photoluminescence emission profiles Of Y2O3 : Eu films composed of high-low density stacks produced by glancing angle deposition. *APPLIED OPTICS*, 47(15):2798–2805, 2008.

[115] Jooho Kim, Z. Dohnálek, and Bruce D. Kay. Structural characterization of nanoporous Pd films grown via ballistic deposition. *Surface Science*, 586(1-3):137–145, July 2005.

[116] Sean M. Pursel, Mark W. Horn, and Akhlesh Lakhtakia. Blue-shifting of circular Bragg phenomenon by annealing of chiral sculptured thin films. *Optics Express*, 14(17):8001, 2006.

[117] D.W. Flaherty, Z. Dohnalek, A. Dohnalkova, B.W. Arey, D.E. McCready, N. Ponnusamy, C.B. Mullins, and B.D. Kay. Reactive Ballistic Deposition of Porous TiO2 Films: Growth and Characterization. *Journal of Physical Chemistry C*, 111(12):4765–4773, March 2007.

[118] W. Smith and Y.-P. Zhao. Superior photocatalytic performance by vertically aligned core–shell TiO2/WO3 nanorod arrays. *Catalysis Communications*, 10(7):1117–1121, March 2009.

[119] Arman Bonakdarpour, Ryan T. Tucker, Michael D. Fleischauer, Nicole A. Beckers, Michael Julian Brett, and David P. Wilkinson. Nanopillar Niobium Oxides as Support Structures for Oxygen Reduction Electrocatalysts. *Electrochimica Acta*, 85:492–500, August 2012.

[120] Bing He, Niall Tait, and Fred Regnier. Fabrication of Nanocolumns for Liquid Chromatography. *Analytical Chemistry*, 70(18):3790–3797, September 1998.

[121] A J Oko, S R Jim, Michael Thomas Taschuk, and Michael Julian Brett. Analyte migration in anisotropic nanostructured ultrathin-layer chromatography media. *Journal of chromatography. A*, 1218:2661–2667, December 2010.

[122] N.A. Beckers, Michael Thomas Taschuk, and Michael Julian Brett. Selective room temperature nanostructured thin film alcohol sensor as a virtual sensor array. *Sensors and Actuators B: Chemical*, 176:1096–1102, January 2013.

[123] K. Okamoto, T. Hashimoto, K. Hara, and E. Tatsumoto. Origin of Magnetic Anisotropy of Iron Films Evaporated at Oblique Incidence. *Journal of the Physical Society of Japan*, 31(5), 1971.

[124] K. Okamoto, T. Hashimoto, K. Hara, M. Kamiya, and Hiroshi Fujiwara. Columnar structure and texture of iron films prepared at various evaporation rates. *Thin Solid Films*, 147(3):299–311, March 1987.

[125] K Okamoto, T. Hashimoto, K. Hara, M. Kamiya, and Hiroshi Fujiwara. Columnar structure and texture of iron films prepared at various pressures. *Thin Solid Films*, 129(3-4):299–307, July 1985.

[126] Kunito Okamoto and Kikuo Itoh. Incidence Angle Dependences of Columnar Grain Structure and Texture in Obliquely Deposited Iron Films. *Japanese Journal of Applied Physics*, 44(No. 3):1382–1388, March 2005.

[127] K. Ozawa, T. Yanada, H. Masuya, M. Sato, S. Ishio, and M. Takahashi. Oblique incidence effects in evaporated iron thin films. *Journal of Magnetism and Magnetic Materials*, 35(1-3):289–292, March 1983.

[128] K Itoh, M. Kamiya, K. Hara, T. Hashimoto, K Okamoto, and Hiroshi Fujiwara. Argon gas pressure dependence of the columnar grain structure in iron films deposited obliquely by sputtering. *Thin Solid Films*, 195(1-2):245–256, January 1991.

[129] Kazuhiro Hara, Hiroshi Fujiwara, Takashi Hashimoto, and Kunito Okamoto. Crystallographic Investigations of Columnar Grains in Iron

Film Evaporated at Oblique Incidence. *Journal of the Physical Society of Japan*, 39(5):1252–1256, May 1975.

[130] F Liu, M T Umlor, L Shen, J Weston, W Eads, J A Barnard, and G J Mankey. The growth of nanoscale structured iron films by glancing angle deposition. *Journal of Applied Physics*, 85(8):5486, 1999.

[131] Bernd Thomas, K. Diesner, T. Cibik, and K. Ellmer. Phase Transitions during the Deposition of Polycrystalline Iron Pyrite (FeS2) - Layers by Low-Pressure Metalorganic Chemical Vapor Deposition. *Solid State Phenomena*, 51-52:301–308, May 1996.

[132] S Kar and S Chaudhuri. Synthesis of highly oriented iron sulfide nanowires through solvothermal process. *Materials Letters*, 59(2-3):289–292, 2005.

[133] Prasad Narhar Gadgil. *Preparation of Iron Pyrite Films for Solar Cells by Metalorganic Chemical Vapor Deposition*. PhD thesis, Simon Fraser University, 1990.

[134] J Oertel, K. Ellmer, W. Bohne, J. Rohrich, and Helmut Tributsch. Growth of n-type polycrystalline pyrite (FeS2) films by metalorganic chemical vapour deposition and their electrical characterization. *Journal of Crystal Growth*, 198-199:1205–1210, March 1999.

[135] Nicholas Berry, Ming Cheng, Craig L. Perkins, Moritz Limpinsel, John C. Hemminger, and Matt Law. Atmospheric-Pressure Chemical Vapor Deposition of Iron Pyrite Thin Films. *Advanced Energy Materials*, 2(9):1124–1135, September 2012.

[136] D.M. Schleich and H.S.W. Chang. Iron pyrite and iron marcasite thin films prepared by low pressure chemical vapor deposition. *Journal of Crystal Growth*, 112(4):737–744, July 1991.

[137] R Misho and W Murad. Band gap measurements in thin films of hematite Fe2O3, pyrite FeS2 and troilite FeS prepared by chemical spray pyrolysis. *Solar Energy Materials and Solar Cells*, 27(4):335–345, September 1992.

[138] A.K. Raturi, L. Ndjeli, and K. Rabah. FeS2 thin films prepared by spray pyrolysis. *Renewable Energy*, 11(2):191–195, June 1997.

[139] G Smestad, A. Da Silva, Helmut Tributsch, S. Fiechter, M. Kunst, N. Meziani, and Mario Birkholz. Formation of semiconducting iron pyrite by spray pyrolysis. *Solar Energy Materials*, 18(5):299–313, May 1989.

[140] A Yamamoto, M. Nakamura, A. Seki, E.L. Li, A. Hashimoto, and S. Nakamura. Pyrite (FeS2) thin films prepared by spray method using FeSO4 and (NH4)2Sx. *Solar Energy Materials and Solar Cells*, 75(3-4):451–456, February 2003.

[141] H Alex Macpherson and Conrad R Stoldt. Iron pyrite nanocubes: size and shape considerations for photovoltaic application. *ACS nano*, 6(10):8940–9, October 2012.

[142] Hongfei F. Liu and Dongzhi Z. Chi. Magnetron-sputter deposition of Fe3S4 thin films and their conversion into pyrite (FeS2) by thermal sulfurization for photovoltaic applications. *Journal of Vacuum Science & Technology A: Vacuum, Surfaces, and Films*, 30(4):04D102, April 2012.

[143] Liping Yu, Stephan Lany, Robert Kykyneshi, Vorranutch Jieratum, Ram Ravichandran, Brian Pelatt, Emmeline Altschul, Heather a. S. Platt, John F. Wager, Douglas a. Keszler, and Alex Zunger. Iron Chalcogenide Photovoltaic Absorbers. *Advanced Energy Materials*, 1(5):748–753, August 2011.

[144] Liuyi Huang, Feng Wang, Zhaoju Luan, and Liang Meng. Pyrite (FeS2) thin films deposited by sol–gel method. *Materials Letters*, 64(23):2612–2615, December 2010.

[145] R.J. Bouchard. The preparation of single crystals of FeS2, CoS2, and NiS2 pyrites by chlorine transport. *Journal of Crystal Growth*, 2(1):40–44, February 1968.

[146] Ahmed Ennaoui. Photoactive Synthetic Polycrystalline Pyrite (FeS[sub 2]). *Journal of The Electrochemical Society*, 132(7):1579, 1985.

[147] G. Willeke, O. Blenk, Ch. Kloc, and E. Bucher. Preparation and electrical transport properties of pyrite (FeS2) single crystals. *Journal of Alloys and Compounds*, 178(1-2):181–191, February 1992.

[148] S Bausch, B. Sailer, H Keppner, G. Willeke, E. Bucher, and G. Frommeyer. Preparation of pyrite films by plasma-assisted sulfurization of thin iron films. *Applied Physics Letters*, 57(1):25, 1990.

[149] H Dahman, M. Khalifa, M. Brunel, and B. Rezig. Iron pyrite films prepared by sulfur vapor transport. *Thin Solid Films*, 280(1-2):56–60, July 1996.

[150] L Huang, Y Liu, and Liang Meng. Pyrite Films Grown by Sulfurizing Precursive Iron of Different Crystallizing Status. *Journal of Materials Science and Technology*, 25(2):237–241, 2009.

[151] L.Y. Huang and Liang Meng. Crystallographic behavior of FeS2 films formed on different substrates. *Materials Chemistry and Physics*, 124(1):413–416, July 2010.

[152] Zhang Hui, Liu Ying-Shu, Wang Bao-Yi, Wei Long, Kui Re-Xi, and Qian Hai-Jie. X-ray absorption near the edge structure and X-ray photoelectron spectroscopy studies on pyrite prepared by thermally sulfurizing iron films. *Chinese Physics B*, 18(7):2734–2738, July 2009.

[153] Liang Meng, J.P. Tu, and M.S. Liu. Formation of pyrite thin films by sulfidation annealing of iron films. *Materials Letters*, 38(2):103–107, January 1999.

[154] G Smestad, Ahmed Ennaoui, S. Fiechter, Helmut Tributsch, W Hofmann, Mario Birkholz, and W Kautek. Photoactive thin film semiconducting iron pyrite prepared by sulfurization of iron oxides. *Solar Energy Materials*, 20(3):149–165, March 1990.

[155] Dongyun Wan, Yutian Wang, Baoyi Wang, Chuangxin Ma, Hong Sun, and Long Wei. Effects of the crystal structure on electrical and optical

properties of pyrite FeS2 films prepared by thermally sulfurizing iron films. *Journal of Crystal Growth*, 253(1-4):230–238, June 2003.

[156] D. Wan, B. Wang, Y. Wang, H. Sun, R. Zhang, and L. Wei. Effects of the sulfur pressure on pyrite FeS2 films prepared by sulfurizing thermally iron films. *Journal of Crystal Growth*, 257(3-4):286–292, October 2003.

[157] G Pimenta and W Kautek. Thermodynamic aspects of pyrite film formation by sulphur conversion of iron. *Thin Solid Films*, 219(1-2):37–45, October 1992.

[158] J.R. Ares, M León, N M Arozamena, J Sánchez-Páramo, P Celis, I.J. Ferrer, and C.R. Sánchez. Evolution of the Seebeck coefficient during the formation and crystallization of pyrite thin films. *Journal of Physics: Condensed Matter*, 10(19):4281–4289, May 1998.

[159] J.R. Ares, A. Pascual, I.J. Ferrer, C.R. Sánchez, and C Sanchez. Grain and crystallite size in polycrystalline pyrite thin films. *Thin Solid Films*, 480-481:477–481, June 2005.

[160] T. G. Myers, J. P. F. Charpin, and C. P. Thompson. Slowly accreting ice due to supercooled water impacting on a cold surface. *Physics of Fluids*, 14(1):240, 2002.

[161] L. Makkonen. Models for the growth of rime, glaze, icicles and wet snow on structures. *Philosophical Transactions of the Royal Society A: Mathematical, Physical and Engineering Sciences*, 358(1776):2913–2939, November 2000.

[162] Graham Poots. *Ice an Snow Accretion on Structures*. Research Studies Press Ltd, University of Michigan, illustrate edition, 1996.

[163] P. J. Martin. Ion-based methods for optical thin film deposition. *Journal of Materials Science*, 21(1):1–25, January 1986.

[164] Jason B. Sorge, Michael Thomas Taschuk, Nicholas G. Wakefield, Jeremy C. Sit, and Michael Julian Brett. Metal oxide morphology in

argon-assisted glancing angle deposition. *Journal of Vacuum Science & Technology A: Vacuum, Surfaces, and Films*, 30(2):021507, 2012.

[165] Jonathan K Kwan and Jeremy C. Sit. The use of ion-milling to control clustering of nanostructured, columnar thin films. *Nanotechnology*, 21(29):295301, July 2010.

[166] Martin R. Kupsta, Michael Thomas Taschuk, Michael Julian Brett, and Jeremy C. Sit. Overcoming cap layer cracking for glancing-angle deposited films. *Thin Solid Films*, 519(6):1923–1929, November 2011.

[167] Kikuo Itoh, Fusao Ichikawa, Yoshinori Takahashi, Kei Tsutsumi, Yoshie Noguchi, Kunito Okamoto, Tetsuji Uchiyama, and Ienari Iguchi. Columnar Grain Structure in Cobalt Films Evaporated Obliquely at Low Substrate Temperatures. *Japanese Journal of Applied Physics*, 45(4A):2534–2538, April 2006.

[168] D.W. Flaherty, Z. Dohnalek, A. Dohnalkova, B.W. Arey, D.E. McCready, N. Ponnusamy, C.B. Mullins, and B.D. Kay. Reactive Ballistic Deposition of Porous TiO2 Films: Growth and Characterization. *Journal of Physical Chemistry C*, 111(12):4765–4773, March 2007.

[169] C. J. Backhouse, S.K. Dew, and Michael Julian Brett. Hollow-cathode assisted sputtering. *Journal of Vacuum Science & Technology A: Vacuum, Surfaces, and Films*, 14(4):2674, July 1996.

[170] Mario Birkholz. *Thin Film Analysis by X-Ray Scattering*. Wiley-VCH, 1 edition, 2006.

[171] B. B. He. *Two-dimensional X-Ray Diffraction*. Wiley, Hoboken, NJ, USA, 2009.

[172] W.S. Rasband. ImageJ.

[173] P.P. Ferguson, Michael D. Fleischauer, Joshua Michael LaForge, A.D.W. Todd, P. Li, and J.R. Dahn. Studies of CoSn grains in the carbon matrix structure of nanostructured tin–cobalt–carbon. *Journal of Alloys and Compounds*, 541:168–172, November 2012.

[174] John C. Russ. *The Image Processing Handbook, Fifth Edition*. CRC Press, 5th edition, 2009.

[175] Edward R. Dougherty and Roberto A. Lotufo. *Hands-on Morphological Image Processing*. SPIE, 1000 20th Street, Bellingham, WA 98227-0010 USA, July 2003.

[176] J. Kittler and J. Illingworth. Minimum error thresholding. *Pattern recognition*, 19(1):41–47, 1986.

[177] J.N. Kapur, P.K. Sahoo, and A.K.C. Wong. A new method for gray-level picture thresholding using the entropy of the histogram. *Computer Vision, Graphics, and Image Processing*, 29(3):273–285, March 1985.

[178] L. Vincent and P. Soille. Watersheds in digital spaces: an efficient algorithm based on immersion simulations. *IEEE Transactions on Pattern Analysis and Machine Intelligence*, 13(6):583–598, June 1991.

[179] Joshua Michael LaForge, Grayson L. Ingram, Michael Thomas Taschuk, and Michael Julian Brett. Flux Engineering To Control In-Plane Crystal and Morphological Orientation. *Crystal Growth & Design*, 12(7):3661–3667, July 2012.

[180] D-X Ye, Tansel Karabacak, R C Picu, G-C Wang, and Toh-Ming Lu. Uniform Si nanostructures grown by oblique angle deposition with substrate swing rotation. *Nanotechnology*, 16(9):1717–1723, September 2005.

[181] Kevin Robbie, Jeremy C. Sit, and Michael Julian Brett. Advanced techniques for glancing angle deposition. *Journal of Vacuum Science & Technology B: Microelectronics and Nanometer Structures*, 16(3):1115, May 1998.

[182] Jitendra P. Singh, F. Tang, Tansel Karabacak, Toh-Ming Lu, and G.-C. Wang. Enhanced cold field emission from $\langle 100 \rangle$ oriented β–W nanoemitters. *Journal of Vacuum Science & Technology B: Microelectronics and Nanometer Structures*, 22(3):1048, 2004.

[183] Huafang Li, Patrick Snow, Ming He, Pei-I Wang, Gwo-ching Wang, and Toh-ming Lu. Biaxially textured Al film growth on CaF2 nanostructures toward a method of preparing single-crystalline Si film on glass substrates. *ACS nano*, 4(10):5627–32, October 2010.

[184] Charles W. Teplin, David S. Ginley, and Howard M. Branz. A new approach to thin film crystal silicon on glass: Biaxially-textured silicon on foreign template layers. *Journal of Non-Crystalline Solids*, 352(9-20):984–988, June 2006.

[185] L Vitos, A V Ruban, H L Skriver, and J Kolla. The surface energy of metals. *Surface Science*, 411:186–202, 1998.

[186] Joshua Michael LaForge, Balazs Gyenes, Sijia Xu, Landon K. Haynes, Lyubov V. Titova, Frank A. Hegmann, and Michael Julian Brett. Tuning iron pyrite thin film microstructure by sulfurization of columnar iron precursors. *Solar Energy Materials and Solar Cells*, 117:306–314, October 2013.

[187] Ahmed Ennaoui, S. Fiechter, Ch. Pettenkofer, N. Alonso-Vante, K. Büker, M Bronold, Ch. Höpfner, and Helmut Tributsch. Iron disulfide for solar energy conversion. *Solar Energy Materials and Solar Cells*, 29(4):289–370, May 1993.

[188] Cyrus Wadia, Yue Wu, Sheraz Gul, Steven K. Volkman, Jinghua Guo, and A Paul Alivisatos. Surfactant-Assisted Hydrothermal Synthesis of Single phase Pyrite FeS 2 Nanocrystals. *Chemistry of Materials*, 21(13):2568–2570, July 2009.

[189] K. Büker, N. Alonso-Vante, and Helmut Tributsch. Photovoltaic output limitation of n-FeS2 (pyrite) Schottky barriers: A temperature-dependent characterization. *Journal of Applied Physics*, 72(12):5721, 1992.

[190] V. Antonucci, A Arico, N Giordano, P.L. Antonucci, U Russo, D.L. Cocke, and F Crea. Photoactive screen-printed pyrite anodes for electrochemical photovoltaic cells. *Solar Cells*, 31(2):119–141, March 1991.

[191] Yan Hu, Zhi Zheng, Huimin Jia, Yiwen Tang, and Lizhi Zhang. Selective Synthesis of FeS and FeS2 Nanosheet Films on Iron Substrates as Novel Photocathodes for Tandem Dye-Sensitized Solar Cells. *Journal of Physical Chemistry C*, 112(33):13037–13042, August 2008.

[192] W. Jaegermann and Helmut Tributsch. Photoelectrochemical reactions of FeS2 (pyrite) with H2O and reducing agents. *Journal of Applied Electrochemistry*, 13(6):743–750, November 1983.

[193] D.M. Nevskaia, I.J. Ferrer, and C. Sanchez. Open circuit photopotentials in n-FeS2 natural single-crystal/aqueous electrolyte junctions. *Solar Energy Materials*, 22(2-3):127–135, July 1991.

[194] A.K Raturi, S Waita, B Aduda, and T Nyangonda. Photoactive iron pyrite films for photoelectrochemical (PEC) cells. *Renewable Energy*, 20(1):37–43, May 2000.

[195] Yun-Yue Lin, Di-Yan Wang, Hung-Chi Yen, Hsuen-Li Chen, Chia-Chun Chen, Chun-Ming Chen, Chih-Yuan Tang, and Chun-Wei Chen. Extended red light harvesting in a poly(3-hexylthiophene)/iron disulfide nanocrystal hybrid solar cell. *Nanotechnology*, 20(40):405207, October 2009.

[196] Ahmed Ennaoui, S. Fiechter, W. Jaegermann, and Helmut Tributsch. Photoelectrochemistry of Highly Quantum Efficient Single-Crystalline n-FeS[sub 2] (Pyrite). *Journal of The Electrochemical Society*, 133(1):97, 1986.

[197] N. Alonso-Vante, G. Chatzitheodorou, S. Fiechter, N. Mgoduka, I. Poulios, and Helmut Tributsch. Interfacial behavior of hydrogen-treated sulphur deficient pyrite (). *Solar Energy Materials*, 18(1-2):9–21, December 1988.

[198] Mario Birkholz, S. Fiechter, A. Hartmann, and Helmut Tributsch. Sulfur deficiency in iron pyrite (FeS2-x) and its consequences for band-structure models. *Physical Review B*, 43(14):11926–11936, May 1991.

[199] M Bronold, Y Tomm, and W. Jaegermann. Surface states on cubic d-band semiconductor pyrite (FeS2). *Surface Science*, 314(3):L931–L936, August 1994.

[200] M Bronold, C Pettenkofer, W. Jaegermann, Bereich Physikalische Chemie, and D Berlin. Surface photovoltage measurements on pyrite (100) cleavage planes: Evidence for electronic bulk defects. *Journal of Applied Physics*, 76(10):5800, 1994.

[201] Jun Hu, Yanning Zhang, Matt Law, and Ruqian Wu. First-principles studies of the electronic properties of native and substitutional anionic defects in bulk iron pyrite. *Physical Review B*, 85(8):085203, February 2012.

[202] Ruoshi Sun, M. K. Y. Chan, and G. Ceder. First-principles electronic structure and relative stability of pyrite and marcasite: Implications for photovoltaic performance. *Physical Review B*, 83(23):235311, June 2011.

[203] Y. N. Zhang, J. Hu, Matt Law, and R. Q. Wu. Effect of surface stoichiometry on the band gap of the pyrite FeS_{2}(100) surface. *Physical Review B*, 85(8):085314, February 2012.

[204] M Bronold, K. Büker, S Kubala, C Pettenkofer, and Helmut Tributsch. Surface Preparation of FeS2 via Electrochemical Etching and Interface Formation with Metals. *Physica Status Solidi (a)*, 135(1):231–243, January 1993.

[205] Jun Cai and Michael R Philpott. Electronic structure of bulk and (001) surface layers of pyrite FeS2. *Computational Materials Science*, 30(3-4):358–363, August 2004.

[206] R Murphy and Daniel R. Strongin. Surface reactivity of pyrite and related sulfides. *Surface Science Reports*, 64(1):1–45, January 2009.

[207] C. de las Heras, I.J. Ferrer, and C.R. Sánchez. Pyrite thin films: Improvements in their optical and electrical properties by annealing at dif-

ferent temperatures in a sulfur atmosphere. *Journal of Applied Physics*, 74(7):4551, 1993.

[208] C. de las Heras, J. L. Martín de Vidales, I.J. Ferrer, and C.R. Sánchez. Structural and microstructural features of pyrite FeS2− x thin films obtained by thermal sulfuration of iron. *Journal of Materials Research*, 11(01):211–220, January 1996.

[209] C. de las Heras and G. Lifante. Optical parameters of pyrite thin films. *Journal of Applied Physics*, 82(10):5132, 1997.

[210] Liang Meng, Y Liu, and W Huang. Synthesis of pyrite thin films obtained by thermal-sulfurating iron films at different sulfur atmosphere pressure. *Materials Science and Engineering B*, 90(1-2):84–89, March 2002.

[211] A Pascual, J.R. Ares, I.J. Ferrer, and C.R. Sánchez. Electrical resistance evolution of Fe thin films during their sulphuration process. *Applied Surface Science*, 234(1-4):355–361, July 2004.

[212] L Huang and Liang Meng. Effects of film thickness on microstructure and electrical properties of the pyrite films. *Materials Science and Engineering: B*, 137(1-3):310–314, February 2007.

[213] Liang Meng and MS Liu. Thin pyrite (FeS2) films prepared by thermal-sulfurating iron films at various temperatures. *Materials Science and Engineering B*, 60(3):168 – 172, June 1999.

[214] Th. de Keijser, E. J. Mittemeijer, and H. C. F. Rozendaal. The determination of crystallite-size and lattice-strain parameters in conjunction with the profile-refinement method for the determination of crystal structures. *Journal of Applied Crystallography*, 16(3):309–316, June 1983.

[215] P.U. Jepsen, D.G. Cooke, and M. Koch. Terahertz spectroscopy and imaging - Modern techniques and applications. *Laser & Photonics Reviews*, 5(1):124–166, January 2011.

[216] T. L. Cocker, L. V. Titova, S. Fourmaux, G. Holloway, H.-C. Bandulet, D. Brassard, J.-C. Kieffer, M. A. El Khakani, and Frank A. Hegmann. Phase diagram of the ultrafast photoinduced insulator-metal transition in vanadium dioxide. *Physical Review B*, 85(15):155120, April 2012.

[217] Lyubov V. Titova, Tyler L Cocker, David G. Cooke, Xiongyao Wang, Al Meldrum, and Frank A. Hegmann. Ultrafast percolative transport dynamics in silicon nanocrystal films. *Physical Review B*, 83(8):085403, February 2011.

[218] Liang Meng, Y.H. Liu, and L. Tian. Evolutions of structure, composition and optical absorption behavior of pyrite films formed by sulfurating iron. *Materials Research Bulletin*, 38(6):941–948, May 2003.

[219] J.R. Ares, A. Pascual, I.J. Ferrer, and CR C.R. Sánchez. Lattice intrinsic defects and electrical resistivity in pyrite thin films. *Thin Solid Films*, 451-452:233–236, March 2004.

[220] W.M. Haynes, editor. *Handbook of Chemistry and Physics*. CRC Press, 92 edition, 2012.

[221] F.J. Humphreys and M. Hatherly. *Recrystallization and Related Annealing Phenomena*. Elsevier, 2 edition, 2004.

[222] Michael Thomas Taschuk, Kathleen M. Krause, John J. Steele, Mark Alan Summers, and Michael Julian Brett. Growth scaling of metal oxide columnar thin films deposited by glancing angle depositions. *Journal of Vacuum Science & Technology B: Microelectronics and Nanometer Structures*, 27(5):2106, 2009.

[223] A.P. Chandra and A.R. Gerson. The mechanisms of pyrite oxidation and leaching: A fundamental perspective. *Surface Science Reports*, 65(9):293–315, September 2010.

[224] Jacques I. Pankove. *Optical processes in semiconductors*. Prentice-Hall, 1971.

[225] I.J. Ferrer, D.M. Nevskaia, C. de las Heras, and C. Sánchez. About the band gap nature of FeS2 as determined from optical and photoelectrochemical measurements. *Solid State Communications*, 74(9):913–916, June 1990.

[226] R Dasbach. *Basic investigations on Pyrite thin-film solar cells*. Phd, University of Konstanz, 1994.

[227] Ruoshi Sun, M. K. Y. Chan, ShinYoung Kang, and G. Ceder. Intrinsic stoichiometry and oxygen-induced p-type conductivity of pyrite FeS_{2}. *Physical Review B*, 84(3):035212, July 2011.

[228] C. Höpfner, K. Ellmer, Ahmed Ennaoui, C Pettenkofer, S. Fiechter, and Helmut Tributsch. Stoichiometry-, phase- and orientation-controlled growth of polycrystalline pyrite (FeS2) thin films by MOCVD. *Journal of Crystal Growth*, 151(3-4):325–334, June 1995.

[229] Sean Seefeld, Moritz Limpinsel, Yu Liu, Nima Farhi, Amanda Weber, Yanning Zhang, Nicholas Berry, Yon Joo Kwon, Craig L Perkins, John C. Hemminger, Ruqian Wu, and Matt Law. Iron pyrite thin films synthesized from an Fe(acac)3 ink. *Journal of the American Chemical Society*, 135(11):4412–24, March 2013.

[230] Joshua Michael LaForge, Brian J. Worfolk, Jillian M. Buriak, and Michael Julian Brett. No Title. In *Sulfurized Iron Pyrite Nanostructured Films for Photovoltaics*, San Francisco, CA, 2012. MRS Spring.

[231] Joshua Michael LaForge, Brian J. Worfolk, Jillian M. Buriak, and Michael Julian Brett. No Title. In *Morphological control of sulfurized iron pyrite with nanostructured iron precursors*, Montreal, QC, 2012. Next Generation Solar (Photovoltaics Canada).

[232] Gary Hodes and David Cahen. All-solid-state, semiconductor-sensitized nanoporous solar cells. *Accounts of chemical research*, 45(5):705–13, May 2012.

[233] Wendy U Huynh, Janke J Dittmer, and A Paul Alivisatos. Hybrid nanorod-polymer solar cells. *Science*, 295(5564):2425, March 2002.

[234] John M. Khosrofian and Bruce A. Garetz. Measurement of a Gaussian laser beam diameter through the direct inversion of knife-edge data. *Applied Optics*, 22(21):3406, November 1983.

[235] X Li, Y Wang, and Liang Meng. Microstructure and optical absorption of FeS2 films formed by sulfurizing precursive iron of various crystallite scales. *Materials Research Bulletin*, 44(2):462–467, 2009.

[236] Y Liu, Liang Meng, and L Zhang. Optical and electrical properties of FeS thin films with different thickness prepared by sulfurizing evaporated iron. *Thin Solid Films*, 479(1-2):83–88, May 2005.

[237] D Lichtenberger, K. Ellmer, R. Schieck, S. Fiechter, and Helmut Tributsch. Structural, optical and electrical properties of polycrystalline iron pyrite layers deposited by reactive d.c. magnetron sputtering. *Thin Solid Films*, 246(1-2):6–12, June 1994.

[238] Y. Sasaki, A. Sugii, and K. Ishii. Iron pyrite thin film prepared by double source vacuum vapor deposition. *Journal of Materials Science Letters*, 18(15):1193–1195, 1999.

[239] Wendy Huynh, Janke J Dittmer, Nerayo Teclemariam, Delia Milliron, A Paul Alivisatos, and Keith Barnham. Charge transport in hybrid nanorod-polymer composite photovoltaic cells. *Physical Review B*, 67:115326, March 2003.

[240] A. A. Damitha T. Adikaari, D. M. Nanditha M. Dissanayake, and S. Ravi P. Silva. Organic–Inorganic Solar Cells: Recent Developments and Outlook. *IEEE Journal of Selected Topics in Quantum Electronics*, 16(6):1595–1606, November 2010.

[241] Sean A McClure, Brian J Worfolk, David A Rider, Ryan T. Tucker, Jordan A M Fordyce, Michael D. Fleischauer, Ken D Harris, Michael Julian Brett, and Jillian M. Buriak. Electrostatic Layer-by-Layer Assembly of CdSe Nanorod/Polymer Nanocomposite Thin Films. *ACS Appl. Mater. Interfaces*, 2(1):219, 2010.

[242] Ilan Gur, Neil A Fromer, Michael L Geier, and A Paul Alivisatos. Air-stable all-inorganic nanocrystal solar cells processed from solution. *Science (New York, N.Y.)*, 310(5747):462–5, October 2005.

[243] Thilo Stöferle, Ullrich Scherf, and Rainer F Mahrt. Energy transfer in hybrid organic/inorganic nanocomposites. *Nano letters*, 9(1):453–6, January 2009.

[244] Andrey a Lutich, Guoxin Jiang, Andrei S Susha, Andrey L Rogach, Fernando D Stefani, and Jochen Feldmann. Energy transfer versus charge separation in type-II hybrid organic-inorganic nanocomposites. *Nano letters*, 9(7):2636–40, July 2009.

[245] Chennupati Jagadish and Stephen Pearton, editors. *Zinc oxide bulk, thin films and nanostructures: processing, properties and applications*. Elsevier, 1st edition, 2006.

[246] Zhong-Lin Wang. Zinc oxide nanostructures: growth, properties and applications. *Journal of Physics: Condensed Matter*, 16(25):R829–R858, 2004.

[247] U. Ozgur, Ya. I. Alivov, C. Liu, A. Teke, M. A. Reshchikov, S. Dogan, V. Avrutin, S.-J. Cho, and H. Morkoc. A comprehensive review of ZnO materials and devices. *Journal of Applied Physics*, 98(4):041301, 2005.

[248] Sheng Xu, Yong Ding, Yaguang Wei, Hao Fang, Yue Shen, Ashok K Sood, Dennis L Polla, and Zhong-Lin Wang. Patterned growth of horizontal ZnO nanowire arrays. *Journal of the American Chemical Society*, 131(19):6670–1, May 2009.

[249] U Diebold. Atomic-scale properties of low-index ZnO surfaces. *Applied Surface Science*, 237(1-4):336–342, 2004.

[250] R Tait, T. J. Smy, and Michael Julian Brett. Modelling and characterization of columnar growth in evaporated films. *Thin Solid Films*, 226(2):196–201, 1993.

[251] D. Vick, LJ Friedrich, S.K. Dew, Michael Julian Brett, Kevin Robbie, M. Seto, and T. J. Smy. Self-shadowing and surface diffusion effects in obliquely deposited thin films. *Thin Solid Films*, 339(1-2):88–94, 1999.

[252] S. V. Kesapragada and Daniel Gall. Anisotropic broadening of Cu nanorods during glancing angle deposition. *Applied Physics Letters*, 89(20):203121, 2006.

[253] Yuping He and Yiping Zhao. Mg Nanostructures Tailored by Glancing Angle Deposition. *Crystal Growth & Design*, 10(1):440–448, 2010.

[254] F. Tang, T. Parker, H.-F. Li, G.-C. Wang, and Toh-Ming Lu. Unusual Magnesium Crystalline Nanoblades Grown by Oblique Angle Vapor Deposition. *Journal of Nanoscience and Nanotechnology*, 7(9):3239–3244, September 2007.

[255] Jian Zhang, Ingo Salzmann, Siegfried Rogaschewski, Jürgen P. Rabe, Norbert Koch, Fujun Zhang, and Zheng Xu. Arrays of crystalline C[sub 60] and pentacene nanocolumns. *Applied Physics Letters*, 90(19):193117, 2007.

[256] S.K. Dew. *Processes and simulation for advanced integrated circuit metallization*. Phd thesis, University of Alberta, 1992.

[257] John R. Taylor. *An Introduction to Error Analysis: The Study of Uncertainties in Physical Measurements*. University Science Books; 2nd edition, 1996.

[258] S. Mukherjee and Daniel Gall. Anomalous scaling during glancing angle deposition. *Applied Physics Letters*, 95(17):173106, 2009.

[259] A.L. Barabási and H.E. Stanley. *Fractal concepts in surface growth*. Cambridge University Press, Cambridge, 1995.

[260] Kiyotaka; Wasa, Makoto; Kitabatake, and Hideaki Adachi. *Thin Film Materials Technology - Sputtering of Compound Materials*. William Andrew Publishing/Noyes, 2004.

Appendix A

Motion control for flux engineering

The angle of inclination (deposition angle α) and azimuthal angle ($\phi > 0$) of the substrate chuck are controlled by programming target positions of α and ϕ at a particular film thickness. The controller monitors deposition rate and moves the substrate chuck through the series of target positions as the film grows. For the FASP = 3 films, the target pitch was limited by the rotation speed of the chuck to 2.01 nm. The three-fold motion consisted of three stationary points, where a target of 0.6 nm was deposited, followed by rapid motion between these positions. Approximately 0.07 nm of material is deposited while rotating between each stationary point. A segment of a deposition file that describes one complete rotation is shown in Table A.1. The nominal flux rate was kept nearly constant at $0.10\,\mathrm{nm}\cdot\mathrm{s}^{-1}$ with minor adjustments to the electron beam current to reduce drift between the target positions and actual positions during film growth. However, the rate can drift between $0.09\,\mathrm{nm}\cdot\mathrm{s}^{-1}$ to $0.11\,\mathrm{nm}\cdot\mathrm{s}^{-1}$ for a few seconds before correction. This effect contributes to reducing the precision of the deposited pitch from the 2.01 nm target to the 2 nm reported in the manuscript text.

Table A.1: Example segment of a motion file used to program a FASP = 3 substrate motion of the chuck during deposition . The target thickness, target α, and target ϕ, tell the motion controller which position in (α, ϕ) the substrate should be in at the target thickness.

Step	Target Thickness [nm]	Target α[°]	Target ϕ[°]
1	0	88	45
2	0.6	88	45
3	0.67	88	165
4	1.27	88	165
5	1.34	88	285
6	1.94	88	285
7	2.01	88	405

Appendix B

Kinetic Fe Image Analysis Mathematica Code

```
ImportNINTSEM[filepath_?FileExistsQ] := Module[{image},
  image = ImportQ[filepath, "TIFF"];

  Switch[
   Last@ImageDimensions[image],
   1920, ImageTake[image, {0, 1790}],
   960, ImageTake[image, {0, 895}]
   ]
  ]

ExportLZW[filepath_String, image_Image] :=
 Export[filepath, image, "TIFF", "ImageEncoding" -> "LZW"]

ProcessImage[imgfp_, sdfN_Integer, mfN_Integer, binmethod_String,
  boundaryQ : (True | False), n_Integer: 1] :=
 Module[
  {img, sdf, enh, mf, dbc, b, comp, compimg, segall, outcompfp,
   outsegallfp, uep, edm, ws, boundary, split},

  img = ImportNINTSEM[imgfp];
```

```
  sdf = StandardDeviationFilter[img, sdfN] // ImageAdjust;
  enh = ImageAdd[img, sdf] // ImageAdjust;
  mf = Nest[MedianFilter[#, mfN] &, enh, n] // ImageAdjust;

  b = Binarize[mf, Method -> binmethod] // FillingTransform;
 b = Image[DeleteBorderComponents@MorphologicalComponents[b], "Bit"];

  If[TrueQ[boundaryQ], Block[{},
   uep = DistanceTransform[b, Padding -> 0] // MaxDetect[#, 0.95] &;
    edm = DistanceTransform[b];
    ws = WatershedComponents[ColorNegate@edm, uep];
    boundary = Image[ws, "Bit"];
    split = ImageMultiply[b, boundary];
    b = split;]
   ];

  comp = DeleteBorderComponents@MorphologicalComponents[b];
  compimg = Image[comp, "Bit16"];
  segall = Image[comp, "Bit"];

  outcompfp =
   FileNameJoin[{compdir, FileBaseName[imgfp] <> "-comp.tif"}];
  outsegallfp =
  FileNameJoin[{maskdir, FileBaseName[imgfp] <> "-segall.tif"}];
  ExportLZW[outcompfp, compimg];
  ExportLZW[outsegallfp, segall];

  (*ImageAssemble[{{sdf},{mf},{b}}*)
  ]

ProcessImageWithMarkers[filename_?FileExistsQ] := Module[{},
  samplename =
   StringReplace[FileBaseName[filename], "-comp" ~~ ___ -> ""];
 markerfp = FileNames[samplename ~~ ___ ~~ ".tif", {graysondir}];
```

```
mrk = Opening[ColorNegate@Apply[Import, markerfp], BoxMatrix[1]];

img = Import[filename];
{r, g, b} = ColorSeparate[img];
all = g;

(*Find Grayson segments*)
seg = GeodesicDilation[mrk, all];

(*Morph filt segments*)
mf = ImageSubtract[all, r];

(*Compute agreed and complements for both sets*)
agreed = ImageMultiply[seg, mf];
mfcomp = ImageSubtract[mf, agreed];
segcomp = ImageSubtract[seg, agreed];

(*Prep final image*)
outimage =
ColorCombine[{ImageSubtract[ImageSubtract[all, mfcomp], segcomp],
   ImageSubtract[ImageSubtract[all, agreed], segcomp],
   ImageSubtract[ImageSubtract[all, agreed], mfcomp]}];

outfilename =
 FileNameJoin[{outdir, FileBaseName[filename] <> ".tif"}];

ExportLZW[outfilename, outimage]
]
```

Appendix C

Optical setup for optical-pump/THz-probe measurements

The setup of the optical-pump/THz-probe measurements performed in Dr. Hegmann's lab. The figure and description are taken from Dr. Tyler Cocker's PhD thesis[14], as he built the instrument.

> **Schematic of the time-resolved terahertz spectroscopy setup in the Ultrafast Spectroscopy Laboratory at the University of Alberta.** The medium power beam (MPB) is used to generate THz pulses in a ([110]) ZnTe crystal by optical rectification. The low power beam (LPB) is used as a sampling beam for electro-optic detection, and passes through a small hole in the back of the final off-axis parabolic mirror. The high power beam (HPB) is used to optically pump the sample, and can be set to a wavelength of 800 nm, 400 nm, or 267 nm using an optical tripler. The high power pulses pass through a hole in the back of an off-axis parabolic mirror and overlap with the THz pulses in time and space at the sample. The spot size of the pump beam at the sample is larger than the THz beam to prevent spatial filtering. The vacuum chamber and cold finger cryostat allow for

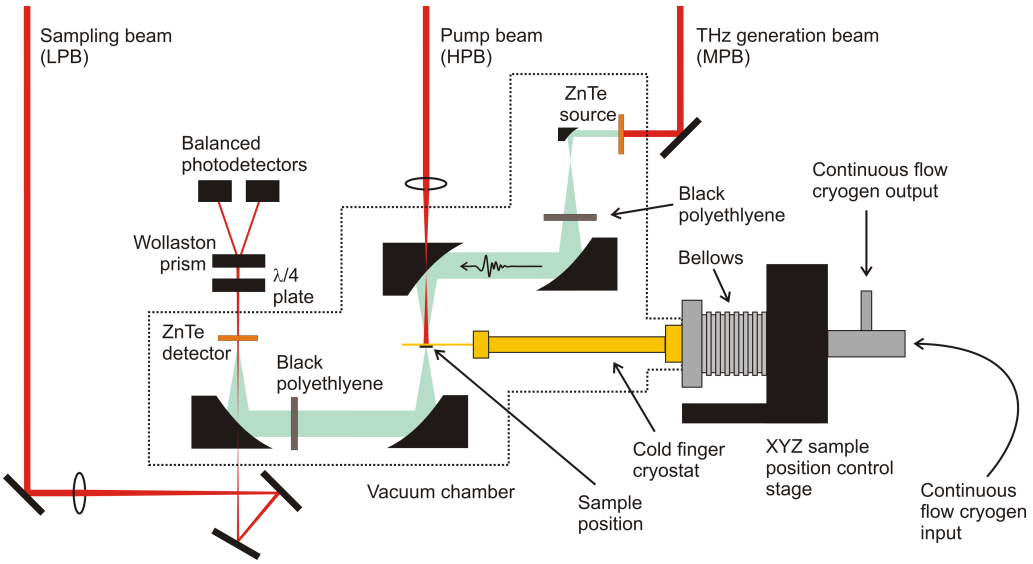

Figure C.1: Schematic of the setup for the optical-pump/THz-probe measurements. Reproduced from [14] with permission from the author.

low-temperature spectroscopy measurements to be made without the THz pulses being absorbed by water vapour or attenuated by windows.

Appendix D

ImageJ Macros for ZnO Image Analsysis

ImageJ Macro code used to process the plan-view SEM images in Chapter 6.

```
run("Auto Threshold", "method=Default white");
run("Remove Outliers...", "radius=2 threshold=50 which=Bright");
run("Remove Outliers...", "radius=2 threshold=50 which=Dark");
run("Options...", "iterations=10 count=4 pad edm=Overwrite do=Close");
run("Invert");
run("Watershed");
```

Appendix E

Sputter system configuration

A conceptual diagram of the sputter vacuum chamber used to deposit the ZnO thin films discussed in Chapter 6 is shown in Figure E.1. The surfaces of the substrates on the rotation stage were positioned over the center of the ZnO target. Argon working gas was fed into the system through an electrically isolate feed through. Stainless steel tubing was bent to position the 5–10 cm length of straight tantalum tubing at approximately 5–10 mm and above the erosion track on the target's surface

The tantalum hollow cathode was made of two concentric tantalum tube purchased from American Elements (Figure E.2).

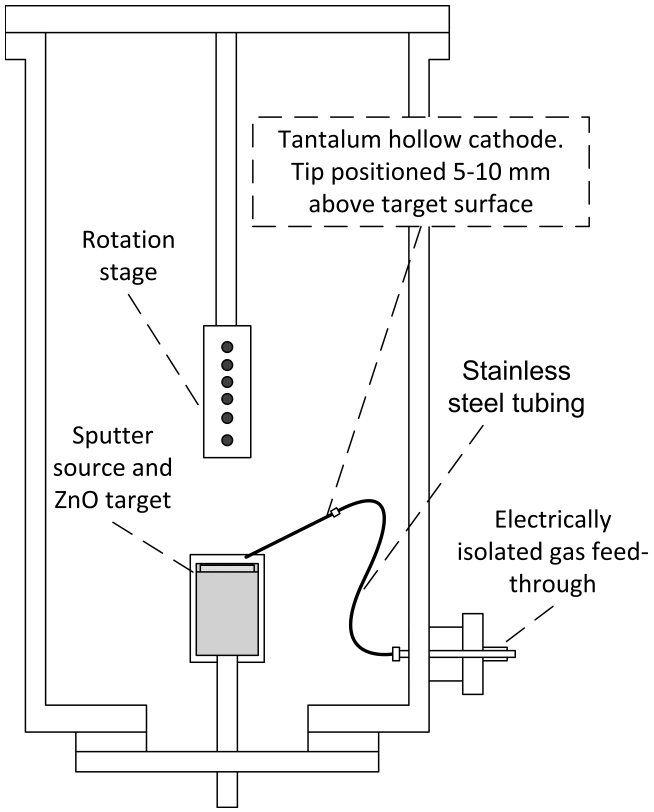

Figure E.1: Conceptual diagram of the sputter vacuum system used to deposit ZnO thin films. The hollow cathode gas feed-through is electrically isolated from the system and injects charged particles (ionized gas, and electrons) directly above the sputter target.

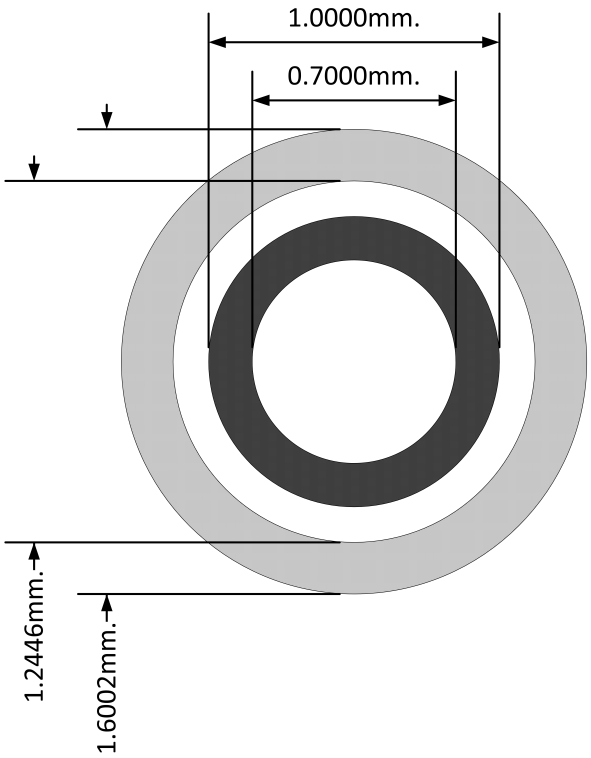

Figure E.2: Cross section of the Tantalum hollow cathode tubing. Both materials are made of Ta. Spacing in the schematic is idealized; there are no additional supports within the tube to maintain the spacing between inner and outer tubes.